

The appearance of vacancies during Cu and Zn diffusion in III-V compound semiconductors

Dissertation

zur Erlangung des akademischen Grades

Dr. rerum naturalium (Dr. rer. nat.)

vorgelegt der

Mathematisch-Naturwissenschaftlich-Technischen Fakultät

(mathematisch-naturwissenschaftlicher Bereich)

der

Martin-Luther-Universität Halle-Wittenberg

von Herrn

Mohamed Elsayed

geb. am 23.11.1976 in Minia, Ägypten

Gutachter:

- (1) Prof. Dr. R. Krause-Rehberg (Martin-Luther-Universität Halle-Wittenberg)
- (2) Prof. Dr. Nicolaas A. Stolwijk (Institut für Materialphysik Universität Münster)
- (3) PD Dr. habil. H.S. Leipner (Martin-Luther-Universität Halle-Wittenberg)

Halle (Saale) 10.12. 2010

Verteidigt am 23.03.2011

Table of contents

1. Introduction	1
2. Diffusion	3
2.1 Introduction	3
2.2 Solution of diffusion equation	5
2.2.1 Thin-film solution	5
2.2.2 Error function solution	6
2.3 Diffusion mechanisms	7
2.3.1 Diffusion without involvement of native point defects	7
2.3.2 Simple vacancy exchange and interstitialcy mechanism	8
2.3.3 Divacancy mechanism	9
2.3.4 Interstitial-Substitutional exchange mechanisms	9
2.3.5 Recombination-enhanced Diffusion	11
2.4 Techniques for studying the diffusion profiles	11
2.4.1 Radiotracer method	11
2.4.2 Other Profiling and Detection Techniques	12
2.4.2.1 Secondary Ion Mass Spectrometry (SIMS)	12
2.4.2.2 Auger Electron Spectroscopy (AES)	12
2.4.2.3 Rutherford Backscattering Spectrometry (RBS)	13
2.4.2.4 Nuclear Reaction Analysis (NRA)	13
2.5 Thermodynamics of point defects in GaAs	13
2.5.1 GaAs system	13
2.5.2 Chemistry of point defects in GaAs	15
2.6 Diffusion in GaAs	18
2.6.1 Gallium self-diffusion	18
2.6.2 Arsenic self-diffusion	21
2.6.3 Impurity diffusion in GaAs	21
2.6.3.1 Silicon diffusion	21
2.6.3.2 Copper diffusion	22
2.6.3.3 Sulfur diffusion	23
3. Experimental methods	25
3.1 Physical background of positron annihilation spectroscopy	25
3.2 Positron annihilation lifetime spectroscopy	27
3.2.1 Lifetime spectra analysis	27
3.2.2 Trapping of positrons in defects	28
3.2.2.1 Positron trapping into one-defect type	30
3.2.3 Shallow positron traps	31
3.2.4 Dependence of positron trapping on the temperature in semiconductors	33
3.2.4.1 Theoretical considerations	33
3.2.4.2 Positron trapping model for experimental data fitting	37
3.2.4.2.1 Trapping of positron by negatively charged vacancy	37
3.2.4.2.2 Trapping of positron into two defects: negative vacancies and shallow traps	38
3.3 Doppler broadening spectroscopy	39
3.3.1 Principle	39
3.3.2 Measurement of annihilation radiation Doppler broadening	40
3.3.3 Line shape parameters	41
3.3.4 Coincidence Doppler-broadening spectroscopy	42

3.4 Procedure of positron annihilation experiments	43
3.5 Other techniques	44
3.5.1 Hall-effect measurement.....	44
3.5.2 Secondary ion mass spectroscopy	44
4. Variable energy positron annihilation spectroscopy.....	47
4.1 Introduction to slow positron beam technique	47
4.2 Positron source and moderation process	47
4.3 Guidance systems of slow positron beam	48
4.4 Basics of the measurement.....	50
4.5 Defect depth profile	51
4.6 Determination the lateral resolution of POSSY	52
5. Vacancy generation during Cu diffusion in semi-insulating and Zn-doped GaAs.....	55
5.1 Introduction.....	55
5.2 Experimental work.....	56
5.3 Results and discussion	57
5.3.1 Reference measurement.....	57
5.3.2 Semi-insulating GaAs.....	58
5.3.3 Zinc-doped GaAs.....	66
5.3.4 Estimation of the positron binding energy to shallow traps.....	68
5.4 Summary	69
6. Identification of defect properties in Te-doped GaAs after Cu in-diffusion by positron annihilation	71
6.1 Introduction.....	71
6.2 Experimental work.....	73
6.3 Positron lifetime results	73
6.3.1 Sample annealed under 10 bar of P_{As}	73
6.3.2 Sample annealed under 0.2 bar	79
6.3.3 Stoichiometry effect.....	81
6.4 Results of coincidence Doppler broadening measurements.....	82
6.5 Determination of concentration of shallow traps and positron binding energy	83
6.6 Conclusion	85
7. Cu diffusion-induced vacancy-like defects in freestanding GaN	87
7.1 Introduction.....	87
7.2 Experimental details.....	88
7.3 Results and discussion	89
7.4 Conclusion	95
8. Observation of As Vacancies during Zn diffusion in GaAs.....	97
8.1 Experimental	99
8.2 Results and discussion	99
8.3 Conclusion	105
9. Summary	107
References	109
Erklärung.....	117
Curriculum vitae	118
Acknowledgements.....	119

Figure captions

Fig. 2.1: Thin-layer solution of the diffusion equation for various diffusion times, plotted as C/a versus x . The numbers on the curves stands for different values of the quantity Dt	5
Fig. 2.2: Complementary error function curve plotted against $2(Dt)^{1/2}$ as the unit of length.	6
Fig. 2.3: Diffusion without involvement of native point defect (Direct interstitial mechanism).	8
Fig. 2.4: The diffusivity of foreign atoms in silicon and silicon self-diffusion. The lines labeled with $Au_s^{(1)}$ and $Au_s^{(2)}$ correspond to different effective diffusivities of substitutional gold in Si. Taken from Ref. [9].	8
Fig. 2.5: Simple vacancy exchange mechanism, left part. Interstitialcy diffusion mechanism (right part).	8
Fig. 2.6: Divacancy mechanism of diffusion.	9
Fig. 2.7: Schematic representation of interstitial-substitutional exchange mechanisms of impurity atom diffusion. Frank-Turnbull mechanism (a) and kick-out mechanism (b). ...	10
Fig. 2.8: Schematic illustration of the tracer method. The main steps, tracer deposition, diffusion annealing, serial sectioning and estimation of the depth profile are shown.	12
Fig. 2.9: Phase diagram of the GaAs System with thermodynamically allowed composition range greatly exaggerated. The figures are taken from Refs.[29,30](left) and [31] (right).	14
Fig. 2.10: Partial pressures of As , As_2 , As_4 in equilibrium with the most Ga rich ((a,a^*) curves) and the most As rich GaAs ((b,b^*) curves). (From Ref. [32]).	14
Fig. 2.11: Thermal equilibrium concentrations of V_{Ga}^{3-} in n-type GaAs, doped to different concentrations, calculated as a function of temperature [37,39].	17
Fig. 2.12: Ga self-diffusion in GaAs and Ga-Al interdiffusion in GaAs/AlGaAs superlattice under intrinsic condition. (Ref. [9])	19
Fig. 2.13: The $(n/n_i)^3$ dependence of Al-Ga interdiffusion data of Mei et al. [58]. $D_{Ga}^V(n_i)$ is described by Eq. 2.43.	20
Fig. 2.14: Fitting of some p-dopant enhanced Al-Ga interdiffusion data. $D_{Ga}^I(n_i)$ is determined by Eq. 2.45. The data fitting shows an approximate quadratic dependence of (p/n_i) . The figure is taken from Ref.[9].	21
Fig. 3.1: Position probability density of the positrons in defect-free GaAs (on the left) and in a Ga vacancy (V_{Ga}) in GaAs (on the right). The atoms position are given (As - full, Ga - shaded). The calculations were carried out using the superimposed-atom model for (110) plane [76,80]. The darker shading corresponds to higher values of the wave function.	25
Fig. 3.2: Schematic representation of the different positron techniques. e^+ from a radioactive source, e.g. ^{22}Na , introduced to the sample, thermalizes within a few ps, diffuses, and finally annihilate. The thermalization distance amounts to $100 \mu m$ which is much larger than the positron diffusion length L_+ . It is estimated to be about $100 nm$	26
Fig. 3.3: A schematic diagram of fast-fast coincidence spectrometer. The lifetime is measured as the time difference between the appearance of the start and stop γ -rays. (PM: photomultiplier; SCA: single channel analyzer; TAC: time-to-amplitude converter; MCA: multi channel analyzer). (From Ref. [79])	27

Fig. 3.4: Positron lifetime spectra measured in GaAs:Zn and GaAs:Si. The presence of native open-volume point defects in GaAs:Si increases the average lifetime compared to that of GaAs:Zn.	28
Fig. 3.5: Schematic representation of the transition-limited trapping (left part) and diffusion-limited trapping (right part).	29
Fig. 3.6: Schematic presentation of the trapping model with only a single defect type. A thermalized positron either annihilates from the delocalized state with annihilation rate λ_b or is trapped into the defect with the trapping rate κ_d and then annihilate with the annihilation rate λ_d	30
Fig. 3.7: Temperature dependence of the average positron lifetime for neutral and negative vacancies (V^0 and V^-) and shallow traps [79]. The effect of shallow positron traps, st , as competing trapping centers to both types of vacancies is shown.	33
Fig. 3.8: A schematic representation of the positron potential V_+ for negative, neutral, and positive vacancies in Si according to Puska et al. [94]. a_0 is the Bohr radius. The Coulomb tail is cut off at a distance $r = 13.6a_0$ as a result of the charge delocalization. The value $4.8a_0$ is assumed as a radius of the neutral vacancy.	34
Fig. 3.9: Temperature dependence of the positron trapping coefficient of positively and negatively charged and neutral monovacancies in Si, according to Puska et al. [76].	35
Fig. 3.10: Schematic representation of the mechanisms of positron energy-loss mechanisms: (i) interband electron-hole excitations; (ii) exciting of the electron from a defect level to conduction band; (iii) trapping into Rydberg states; (iv) transition between Rydberg states, and (v) between Rydberg and ground states [94].	35
Fig. 3.11: A scheme of two-stage positron into negatively charged vacancy. The Rydberg states (thin lines) are replaced by a single level [79].	36
Fig. 3.12: Model of positron trapping into a negative vacancy. It involves positron capture into Rydberg states of the attractive Coulomb potential at a rate K_R and positron detrapping from these states at rate δ_R . (From Ref. [39])	38
Fig. 3.13: Schematic presentation of the trapping model for two types of defects (neutral vacancies and shallow traps). A thermalized positron may be trapped to the vacancy with trapping rate κ_d or to the shallow trap with trapping rate κ_{st} . Positrons trapped to the shallow traps either annihilate with annihilation rate $\lambda_{st} \approx \lambda_b$ or escape back to the delocalized state with detrapping rate δ_{st}	38
Fig. 3.14: The vector diagram of the momentum conservation during the 2γ -annihilation process. p stands for the momentum of e^-e^+ pair. p_L and p_T denote the longitudinal and transverse components, respectively.	39
Fig. 3.15: Schematic diagram of the Doppler broadening experiment. A LN_2 cooled Ge-detector is used to measure the energy distribution of the annihilation line. The signal of the Ge-detector is processed by the preamplifier included in the detector. The output signal of the amplifier is provided to a spectroscopy amplifier. Its output signal is stored in the MCA after analog-to-digital conversion. Taken from Ref. [79].	41
Fig. 3.16: Doppler broadening spectra of two samples: for the defect-free GaAs:Zn, reference and plastically deformed GaAs [79]. S and W parameters are evaluated by the illustrated areas divided by the area under the whole curve. Both spectra are normalized to the same area.	41

Fig. 3.17: Two Doppler broadening spectra of GaAs:Zn normalized to the same area. One of them is measured (●) with a single Ge detector and the other was measured (○) by CDBS. The background reduction is clearly demonstrated.....	43
Fig. 3.18: Schematic diagram of a SIMS spectrometer.	45
Fig. 4.1: Positron emission spectrum of a ^{22}Na source is schematically represented [79]. $N(E)$ is the number of positrons per energy channel E . The narrow curve positioned at 3 eV shows the energy distribution after moderation in tungsten.	47
Fig. 4.2: Schematic representation of positron moderation process in transmission geometry by a (110) tungsten foil. A small fraction stops in the foil and annihilates there. They may spontaneously released upon reaching the surface due to the negative work function of W . The majority of positrons leave the moderator foil with a high energy. (From Ref. [79]).....	48
Fig. 4.3: Schematic diagram of the slow-positron-beam system POSSY at Martin Luther University Halle–Wittenberg. Moderated positrons are fed through the collimator by the solenoids and are accelerated to the sample. The whole longitudinal magnetic field is generated by the guidance coils (m).	48
Fig. 4.4: Schematic representation of the steerers which guide the positron beam to hit the target.	49
Fig. 4.5: Scan of the aperture at 10 keV.	49
Fig. 4.6: Contour plot obtained by calibration the coils pairs of the sample at 3 keV. One can see obviously the sample position at the middle of the plot.	50
Fig. 4.7: Implantation profile in GaAs calculated for different incident positron energies according to Eq. 4.2 using the values of parameters which are mentioned above.	51
Fig. 4.8: Low momentum parameter as a function of the distance through scanning the sample holder in the vertical direction. The positron energy is 10 keV. The lateral resolution at the sample position is ~ 4 mm.	52
Fig. 5.1: Solubility of Cu in undoped GaAs as a function of temperature (Ref.[17]).	55
Fig. 5.2: Temperature profile of the two-zone furnace used for the annealing of GaAs samples under different As pressures.	56
Fig. 5.3: Vapor pressure of metallic As as a function of the temperature, taken from Ref. [129]. ..	57
Fig. 5.4: Average positron lifetime as a function of the sample temperature in semi-insulating and Zn-doped GaAs without treatment.	58
Fig. 5.5: Average positron lifetime as a function of sample temperature in undoped SI GaAs. Prior to the experiment, about $6 \times 10^{18} \text{ cm}^3$ Cu atoms were introduced by evaporating a layer of 30 nm Cu onto the sample surface and by subsequent annealing at 1100 °C under 0.2 bar of As pressure (3h, then quenched into water). The temperature-dependent lifetime experiment was carried out after each annealing step as illustrated in the figure.	58
Fig. 5.6: Positron lifetime results of the annealing experiment of undoped semi-insulating GaAs after in-diffusion of $6 \times 10^{18} \text{ cm}^3$ Cu atoms at 1100 °C under 0.2 bar of As pressure. The average lifetime is shown in the lower panel. The defect-related lifetime versus the annealing temperature is plotted in the upper panel. The spectra were measured at a sample temperature of 466 K to diminish the influence of the shallow traps.	59

- Fig. 5.7: Defect concentration and the number of vacancies as a function of the annealing temperature in undoped SI GaAs after in-diffusion of $6 \times 10^{18} \text{ cm}^{-3}$ Cu atoms at 1100 °C under 0.2 bar of As pressure. The number of vacancies in the observed clusters is shown in the upper panel. The defect concentration versus the annealing temperature is plotted in the lower panel. These Data were calculated using the positron lifetime results presented in Fig. 5.5..... 59
- Fig. 5.8: Average positron lifetime as a function of sample temperature in undoped SI GaAs. The samples were annealed at 1100 °C under 0.2 bar of As pressure. The samples were not treated with copper as a reference experiment to the results shown in Fig. 5.5. The temperature-dependent lifetime experiment was carried out after each annealing step as illustrated in the figure..... 60
- Fig. 5.9: Average and defect-related positron lifetime versus measurement temperature for undoped semi-insulating GaAs annealed at 1100 °C for 3 hours under different arsenic pressures compared to a not annealed reference sample. Lines are to guide the eye only. 61
- Fig. 5.10: Vacancy defect concentrations in semi-insulating and Si-doped GaAs versus As vapor pressure during annealing at 1100 °C (Ref. [134]). Solid lines are the power law fits to the data points. Closed circles present the concentration of Cu impurities obtained with the help of titration measurements for the samples annealed at 0.2 and 9.68 bar. 62
- Fig. 5.11: Normalized annihilation momentum distribution measured at room temperature in pure Cu (upper panel) and SI GaAs after Cu in-diffusion and SI GaAs annealed at 1100 °C under $P_{\text{As}} = 0.2$ bar (lower panel). 63
- Fig. 5.12: Average positron lifetime as a function of sample temperature in undoped SI GaAs. Prior to the experiment, about 6×10^{18} Cu atoms were introduced by evaporating a layer of 30 nm Cu onto the sample surface and by subsequent annealing at 1100 °C under 5.57 bar of As pressure (3h, then quenched into water). The temperature-dependent lifetime experiment was carried out after each annealing step as illustrated in the figure. 64
- Fig. 5.13: Positron lifetime results of the annealing experiment of undoped semi-insulating GaAs after in-diffusion of $6 \times 10^{18} \text{ cm}^{-3}$ Cu atoms at 1100 °C under 5.57 bar of As pressure. The average lifetime is shown in the upper panel. The defect-related lifetime and its intensity versus the annealing temperature are plotted in the lower two panels. The spectra were measured at a sample temperature of 466 K to diminish the influence of the shallow traps. 64
- Fig. 5.14: Defect concentration and the number of vacancies as a function of the annealing temperature in undoped SI GaAs after in-diffusion of $6 \times 10^{18} \text{ cm}^{-3}$ Cu atoms at 1100 °C under 5.57 bar of As pressure. The number of vacancies in the observed clusters is shown in the upper panel. The defect concentration versus the annealing temperature is plotted in the lower panel. These Data were calculated using the positron lifetime results presented in Fig. 5.13..... 65
- Fig. 5.15: Average positron lifetime as a function of sample temperature in undoped SI GaAs. The samples were annealed at 1100 °C under 5.57 bar of As pressure. The samples were not treated with copper as a reference experiment to the results shown in figure 5.12. The temperature-dependent lifetime experiment was carried out after each annealing step as illustrated in the figure..... 65

- Fig. 5.16: Average positron lifetime as a function of sample temperature in GaAs:Zn. Prior to the experiment, a layer of 30 nm Cu was deposited onto the sample surface and introduced by subsequent annealing at 1100 °C under 0.2 bar of As pressure. The temperature-dependent lifetime experiment was carried out after each annealing step as displayed in the figure. 66
- Fig. 5.17: Lifetime results of the annealing experiment of Zn doped GaAs after Cu in-diffusion at 1100 °C under 0.2 bar of As pressure. The average lifetime is shown in the lower panel. The defect-related lifetime versus the annealing temperature is plotted in the upper panel. The spectra were measured at a sample temperature of 466 K to diminish the influence of the shallow traps. 66
- Fig. 5.18: Defect concentration versus the annealing temperature in GaAs:Zn ($3.8 \times 10^{16} \text{ cm}^{-3}$) after in-diffusion of $6 \times 10^{18} \text{ cm}^3$ Cu atoms at 1100 °C under 0.2 bar of As pressure. The data were calculated according the positron lifetime results in Fig. 5.16. 67
- Fig. 5.19: Normalized annihilation momentum distribution measured at room temperature in pure Cu (upper panel) and Cu-diffused GaAs:Zn (lower panel) . Cu in-diffusion was performed by annealing the sample at 1100 °C under $P_{As} = 0.2$ bar. The sample was subject to an annealing up to 750 K, which shows a maximum effect on the lifetime. 67
- Fig. 5.20: Average positron lifetime versus sample temperature in Zn doped GaAs. The samples were annealed at 1100 °C under 0.2 bar of As pressure without Cu treatment. The temperature-dependent lifetime experiment was performed after different annealing steps. 68
- Fig. 5.21: The ratio of the detrapping and trapping rates in Cu diffused GaAs:Zn annealed under 2 bar of P_{As} calculated from the decomposition of the lifetime spectra after annealing the sample at 750 K using Eq. (5.5). The solid line is the fit of Eq. (5.6) to the experimental data with $E_b = 70 \text{ meV}$ 69
- Fig. 6.1: Average positron lifetime as a function of measurement temperature in GaAs:Te. Prior to the experiment, about $6 \times 10^{18} \text{ cm}^3$ Cu atoms were introduced by evaporating a layer of 35 nm Cu onto the sample surface and by subsequent annealing for 3h at 1100 °C under 10 bar of As vapor pressure (then quenched into RT water). The sample is isochronally annealed. The temperature-dependent lifetime experiment was performed after each annealing step as illustrated in the figure. 74
- Fig. 6.2: Positron lifetime results of the isochronal annealing experiment of GaAs:Te after in-diffusion of $6 \times 10^{18} \text{ cm}^3$ Cu atoms at 1100 °C under 10 bar of As pressure. The average lifetime is shown in the lower panel. The lifetimes and their relative intensities versus the annealing temperature are plotted in the two upper panels. The spectra were measured at a sample temperature of 500 K to avoid the influence of the shallow traps. 75
- Fig. 6.3: Defect concentration and the number of vacancies (N) included in one cluster versus the annealing temperature in Cu diffused GaAs:Te. The defect concentration versus the annealing temperature is plotted in the lower panel. The number of vacancies in the observed clusters is shown in the upper panel. These data were calculated using the positron lifetime results presented in Fig. 6.1. 76
- Fig. 6.4: Positron lifetime decomposition as a function of sample temperature in Cu diffused GaAs:Te at 1100 °C under 10 bar of As vapor pressure. The sample is isochronally annealed up to 750 K. Then, the temperature-dependent lifetime experiment was performed. The average lifetime is represented in Fig. 6.1. 77
- Fig. 6.5: Positron annihilation fraction versus the measurement temperature calculated using the lifetime decomposition presented in Fig. 6.4. 77

- Fig. 6.6: *The measured S parameter as a function of the sample temperature for Cu diffused GaAs:Te under 10 bar of P_{As} . The sample is annealed up to 750 K. Afterward, the temperature-dependent Doppler broadening experiment was carried out.* 78
- Fig. 6.7: *Positron lifetime decomposition as a function of sample temperature in Cu-diffused GaAs:Te. Cu in-diffusion is performed at 1100 °C under 10 bar of As vapor pressure. The sample was isochronally annealed up to 825 K. Subsequently, the temperature-dependent lifetime experiment was performed.*..... 78
- Fig. 6.8: *Average positron lifetime as a function of sample temperature in GaAs:Te. The sample was annealed at 1100 °C under 10 bar of As pressure and quenched. The sample was not treated with copper and is thus a reference experiment to the results shown in Fig. 6.1. The samples were annealed up to 900 K. The temperature dependent lifetime experiment was performed for the sample in the as-quenched state and after annealing at 700 K and 900 K.* 79
- Fig. 6.9: *Average positron lifetime as a function of sample temperature in GaAs:Te. Before the experiment, about $6 \times 10^{18} \text{ cm}^{-3}$ Cu atoms were deposited onto the sample surface. Cu in-diffusion is performed for 3 h at 1100 °C under 0.2 bar of As vapor pressure. Therefore, the sample is quenched into water at RT. It is isochronally annealed. The temperature-dependent lifetime experiment was carried out after each annealing step.* . 79
- Fig. 6.10: *Positron lifetime results of the isochronal annealing experiment of GaAs:Te. In-diffusion of $6 \times 10^{18} \text{ cm}^{-3}$ Cu atoms is performed at 1100 °C under 0.2 bar of P_{As} . The average lifetime is shown in the lower panel. The lifetimes and their relative intensities versus the annealing temperature are plotted in the two upper panels. The spectra were measured at a sample temperature of 500 K to diminish the influence of the shallow traps.* 80
- Fig. 6.11: *Defect concentration versus the annealing temperature in Cu diffused GaAs:Te under 0.2 bar of As vapor pressure. These data were estimated using the positron lifetime results presented in Fig. 6.10.*..... 81
- Fig. 6.12: *High momentum part of the positron annihilation momentum distribution, normalized to SI undoped GaAs reference (left part). In the upper part (a) the spectrum for pure copper is shown, lower part (b) represents spectra of two GaAs:Te samples: In one of them, the Cu in-diffusion is performed under 0.2 bar of P_{As} and annealed subsequently up to 700 K. For the other, the Cu in-diffusion is carried out under 10 bar of P_{As} and the sample is subject to isochronal annealing up to 750K. The right part shows the ratio of high momentum distribution to the bulk GaAs for pure Cu (c) and different vacancies in GaAs (d) from theoretical calculations. The calculation was done using GGA. The curve of $V_{Ga-Cu_{Ga}}$ complex is highlighted to emphasize the agreement to the respective experimental data in GaAs:Te annealed samples.* 82
- Fig. 6.13: *The concentration of shallow positron traps determined at 29 K as a function of the annealing temperature in Cu diffused GaAs:Te annealed under 10 bar of P_{As} . The calculation was performed using the decomposition of positron lifetime results shown in Fig. 6.1.* 84
- Fig. 6.14: *The ratio of the detrapping and trapping rates in Cu diffused GaAs:Te annealed under 10 bar of P_{As} calculated from the decomposition of the lifetime spectra after annealing the sample at 650 K using Eq. (5.5). The solid line is the fit of Eq. (5.6) to the experimental data with $E_b = 79.4 \text{ meV}$.* 85
- Fig. 7.1: *SIMS depth profiles of GaN sample after Cu diffusion induced by annealing for 96 h at 873 K. Note that surface peaks are artifact of SIMS measurements.* 90

Fig. 7.2: Positron lifetime spectrum recorded for Cu-diffused fs-GaN after annealing at 550 K. For the sake of comparison, data of virgin fs-GaN are also displayed. The spectra were measured at 300 K.	90
Fig. 7.3: Average positron lifetime measured for fs-GaN samples at different temperatures. The samples are isochronally annealed. The temperature-dependent lifetime experiment was carried out after each annealing step as indicated in the figure.	91
Fig. 7.4: Average positron lifetime of Cu-diffused fs-GaN samples after the isochronal annealing. The spectra were measured at a sample temperature of 333K.	91
Fig. 7.5: Average positron lifetime of virgin fs-GaN sample as a function of the measurement temperature. The sample was annealed for 96 h at 873 K without deposition of Cu-cap layer. The sample is isochronally annealed at different temperatures. A reference sample before the annealing is also shown for comparison.	92
Fig. 7.6: Doppler broadening parameters as a function of the incident positron energy measured for the virgin and Cu-diffused GaN annealed up to 550 K samples. The low momentum parameter S is shown in the lower panel and W in the upper panel. The positron mean penetration depth is shown in the top axis. The inset in the lower panel displays the difference of S parameter between the Cu-diffused and virgin samples.	93
Fig. 7.7: W versus S plot for the slow-positron beam measurement of the virgin and Cu-diffused GaN samples. The data are obtained from figure 7.6.	94
Fig. 7.8: SIMS depth profiles of Cu-diffused GaN sample after annealing at 850 K. Note that the surface peaks are artifact of the SIMS measurements.	95
Fig. 8.1: Ion image for the as-quenched Zn-diffused SI GaAs measured by TOF-SIMS. Zn diffusion was performed from both surfaces of the sample for 2h at 950 °C. The diffusion is terminated by quenching the sample in RT water. The SIMS measurement was performed on the cleaved sample with a measuring area of $500 \times 500 \mu\text{m}^2$	99
Fig. 8.2: Low momentum (S) parameter as a function of the incident positron energy in SI GaAs reference sample.	100
Fig. 8.3: Investigation of defects generated by Zn diffusion in SI GaAs. The S parameter is presented as a function of the incident positron energy for the as-quenched sample and after stepwise etching for the same sample. The thickness of the layer removed by etching is shown on the right side of the figure.	101
Fig. 8.4: S parameter plotted as a function of the depth from the sample surface. The curve was compiled from the individual $S(E)$ curves measured for the as-quenched sample and after each etching step for the same sample (Fig. 8.3). The etch depths were considered as appropriate rightward shifts. The S parameter approaches the reference level at a depth of $41 \mu\text{m}$. Therefore, this value represents the defect layer. The solid line is plotted as a smoothed curve to guide the eye.	102
Fig. 8.5: Defect profile as obtained by positron annihilation in Zn-diffused SI GaAs. The positron trapping rate is plotted as a quantity proportional to the defect concentration as a function of the depth.	102
Fig. 8.6: Temperature dependence of the average positron lifetime in Zn-diffused GaAs. The measurement is repeated after each etching step for the same sample as shown in the figure.	103
Fig. 8.7: Average and defect-related positron lifetimes and its relative intensity in Zn diffused GaAs as a function of the depth below the surface. The profile was assembled from the individual measurements for the as-quenched sample and after each etching step for the same sample measured at 300 K. The etch depths were taken into account as appropriate rightward shifts. τ_{av} approaches the reference level at a depth of $45 \mu\text{m}$	103

Fig. 8.8: Results of Doppler broadening spectroscopy of Zn-diffused SI GaAs (as-quenched) and pure Zn samples. All ratio plots are normalized to SI GaAs reference sample (left part). Ratio of the momentum density to bulk GaAs for different vacancies and vacancy complex in GaAs are theoretically calculated (right part). The curve for $V_{As}-2Zn_{Ga}$ is in an agreement to the measured in Zn-diffused GaAs. The theoretical curves are not accurate for $P_L < 20 \times 10^{-3} m_0c$ Ref. [105] and hence are omitted. 104

Fig. 8.9: Average positron lifetime as a function of sample temperature in SI GaAs. The sample was annealed without Zn addition for 2h at 950 °C. Only 10 mg As was added. The annealing is terminated with quenching the sample in water. The sample is thus a reference experiment to the results shown in Fig. 8.6. 105

Abbreviations and Symbols

ACAR	angular correlation of annihilation radiation
ADC	analog-digital converter
AES	auger electron spectroscopy
AFM	atomic force microscopy
A_i	interstitially dissolved atom of species A
A_s	substitutionally dissolved atom of species A
AS_{Ga}	antisite defect of an arsenic atom occupying Ga sublattice site
c	speed of light
C	concentration
C_d	defect concentration
CDBS	coincidence Doppler broadening spectroscopy
C_x^{eq}	thermal equilibrium concentration of species x
Cu_{Ga}	Cu on gallium sublattice
D	positron decay spectrum
D	diffusivity or diffusion coefficient
D_+	positron diffusion constant
DBS	Doppler broadening spectroscopy
D^{eff}	effective diffusivity
e	elementary charge
E	energy
E_b	positron binding energy to shallow traps
E_f	Fermi energy
	energy of final state
E_g	energy gap
E_i	energy of initial state
E_R	positron binding energy to Rydberg states
f_s	fraction of positrons diffusing back to the surface
FWHM	full width at half maximum
Ga_{As}	antisite defect of an gallium atom occupying As sublattice site
GGA	gradient generalized approximation
h	Planck constant
h^+	hole
h^f	formation enthalpy
i	interstitially dissolved atom
I	self-interstitials
I	intensity of positron lifetime components
i-s	interstitial-substitutional impurity
k	number of different defect types
K	mass action constant
k_B	Boltzmann constant
L_+	positron diffusion length
LEC	liquid encapsulated Czochralski
LT	lifetime
MCA	multi-channel analyzer
MELT	maximum entropy of lifetime
m_0	electron rest mass
m^*	positron effective mass
N	lifetime spectrum
n	donor doped or electron concentration of semiconductor
n	quantum number
n_+	positron density

n	electron density
n_b	number of positrons in the bulk
n_d	number of positrons in the defect
n_i	intrinsic carrier concentration
NRA	nuclear reaction analysis
P	pressure
P	probability
	positron wave-vector
	positron implantation profile
	stopped fraction of positron
p	momentum
p	acceptor doped or hole concentration of semiconductor
PALS	positron annihilation lifetime spectroscopy
PAS	positron annihilation spectroscopy
p_L	longitudinal momentum component
p_T	transverse momentum component
Q	activation energy
	charge state of vacancies
R	gas constant
RBS	Rutherford backscattering spectroscopy
r_d	defect radius
r_o	classical electron radius
s	substitutionally dissolved atom
	$s=1-2x$ stoichiometry deviation
S	S parameter
SCA	single channel analyzer
S^f	formation entropy
SIMS	secondary ion mass spectrometry
st	shallow traps
STM	scanning tunneling microscopy
t	time
T	temperature
TAC	time-to-amplitude converter
TEM	transmission electron microscopy
V	vacancies
V_+	positron potential
V_{As}	arsenic vacancy
VEPFIT	variable energy positron fit
VEPAS	variable energy positron annihilation spectroscopy
V_{Ga}	gallium vacancy
V_N	nitrogen vacancy
V_P	phosphorus vacancy
W	W parameter
x	distance
δ	positron detrapping rate
ϵ	dielectric constant
η	annihilation fraction positrons
κ_d	positron trapping rate
λ	positrons annihilation rate
λ_{eff}	positrons annihilation rate
μ	positron trapping coefficient
ρ	density
τ	positron lifetime
τ_{av}	average positron lifetime

τ_b

bulk positron lifetime

τ_d

defect-related positron lifetime

1. Introduction

Gallium arsenide (GaAs) and gallium nitride (GaN) are today most important III-V compound semiconductors. Both are used to produce a variety of discrete and integrated optoelectronic devices due to their electronic properties and direct band gap. They also represent the basic materials of semiconductor laser, which offers many industrial applications. Moreover, current advances in the production of thin layers have made a whole new range of multi-quantum-wells-based devices achievable. Besides GaAs, GaN has attracted much attention in the production of high-electron-mobility transistors. The manufacture of semiconductor devices is almost performed during heat treatment processes, which implies that some diffusion have to take place during their fabrication. Understanding of dopant diffusion process is deemed of interest to keep control over the technology.

With an increasing appreciation of how the behavior of impurities such as copper (Cu) and zinc (Zn) in GaAs and GaN lattices, investigation on their influential role in shaping the electrical and structural properties can now follow. In addition to this intentional doping, existence of Cu is often encountered during semiconductor device growth and processing. Zinc diffusion in GaAs is technologically pivotal for the fabrication of laser diodes and the other III-V devices.

Copper (Cu) is among the impurities in GaN that has recently received increase attention owing to the associated room-temperature ferromagnetism, which could create new opportunities in GaN-based spintronics. Point defects play an important role in determining the properties of semiconductor materials by reducing the density of free carriers or mediating, e.g., dopant diffusion. From a fundamental point of view, exploring and elucidation the formation of defects and their behavior are of vital importance to the understanding of the properties of these materials. It is necessary to thoroughly characterize these materials: an area that well merits such a characterization concerns point defects responsible for occurrence of diffusion.

Characterization of point defects during diffusion of Cu and Zn in Zn-, Te-doped and semi-insulating (SI) GaAs and free-standing (fs) GaN crystals were studied in this work. Positron annihilation spectroscopy (PAS) was utilized as the main method of study.

PAS is well recognized as a powerful probe of material microstructure investigations. It is a sensitive tool for the detection of vacancy-type defects. Nevertheless, the interpretation of PAS results would not be feasible without combination of additional experimental techniques for the detailed microscopic identification of defects.

Diffusion of copper from thin Cu cap layer into the bulk samples was carried out during annealing at high temperature followed by quenching into room temperature water to freeze the equilibrium concentration of defects as well as possible. The samples were subject to further isochronal annealing for the out-diffusion process. Investigations with PAS and associated methods were performed after each annealing step.

Zinc diffusion in GaAs was performed by using metallic Zn as a source for diffusion. The samples were stepwise etched and subject to PAS measurements after each etching step.

The work is arranged as follows: Physical background of diffusion phenomenon, diffusion mechanisms and diffusion in GaAs are described in chapter 2. Chapter 3 gives a brief review of the different positron techniques and other experimental methods, which may help in characterization of defects in materials. Slow positron beam description and determination of its lateral resolution are dealt in Chapter 4. Chapter 5 is devoted to the study of vacancy generation during Cu diffusion in semi-insulating (SI) and Zn-doped GaAs. Identification of defects introduced during Cu diffusion in Te-doped GaAs and GaN crystals are discussed in Chapters 6 and 7, respectively.

Chapter 8 focuses on the observation of arsenic vacancies during Zn diffusion in SI GaAs. A summary is given in Chapter 9.

2. Diffusion

2.1 Introduction

Diffusion is a well-known natural phenomenon. It can be defined as thermally stimulated random motion of atoms or molecules in gases, liquids and solids. This kind of motion was first seen by Robert Brown in 1827 [1]. The mathematical formulation of Brownian motion was done by Albert Einstein in 1905 and 1906 [2,3]. Understanding diffusion phenomena in compound semiconductors is of fundamental importance, since the electrical properties of semiconductor devices can strongly depend on the thermal stability of a *p-n* junction or an Ohmic contact. Diffusion can also be used as a tool to introduce dopants into a semiconductor. Conventionally, the semiconductor industry has been established on silicon and the knowledge of the material and electrical properties of silicon is therefore widespread. Nevertheless, silicon has its own drawbacks in contrast to compound semiconductor materials, such as GaAs and GaN. For example, silicon has an indirect band gap and thus it cannot be used in optoelectronic devices. The use of compound semiconductors in electronic devices has received a huge step forward in the recent decades. Much of daily electronics, such as CD-players and laser pointers, are dependent on the compound semiconductor structures. Nevertheless, with the quickly diminishing size of the active components, more knowledge of the electronic and material properties of the semiconductors used in the manufacture of devices is necessitated. Commonly, thin charge transmitting metal wires are used to connect the integrated circuits to a power source and to other electronic devices. These Ohmic contacts must be thermally stable to keep as superior electronic properties as possible. Namely, there have to be no combination of contact and device material through diffusion and no loss of adhesion. The Ohmic contacts are normally heterostructures of several materials, for example Au, Pt, Ti and Ni. Silicon is incorporated in GaAs frequently as donor leading to *n*-type conductivity. The dopant is often incorporated into semiconductor materials by ion implantation or by diffusion from an external source. Since Si is a group IV element it can show amphoteric behavior [4] in compound semiconductors, i. e., it can work both as an acceptor and as a donor depending on, on which sublattice it substitutes in the host lattice. Earlier studies have explained Si diffusion in GaAs by taking into account that Si as an amphoteric dopant, diffusing by pairing with Ga and As vacancies [4]. However, it has been observed experimentally that a significant amount of Si occupies interstitial sites [5]. These Si interstitial should be considered in order to fully elucidate the Si diffusion in GaAs. The charge state of the interstitial Si atom is also of interest, because it has a clear effect on the position of the Fermi level; or what is so called Fermi level effect. Point defects, e.g. vacancies, may influence the electrical properties of semiconductors by establishing energy levels in the band gap, which behave as charge carrier traps and compensators [6]. The mathematical basis of the diffusion was laid by Fick, whose first law states that the rate of the transfer of diffusers through unit area is proportional to the magnitude of the gradient normal to the area. The flux of atoms in *x*-direction, assuming that *x*-axis is chosen as the direction of the concentration gradient, is given by:

$$J_x = -D \frac{\partial C(x,t)}{\partial x}. \quad (2.1)$$

The concentration $C(x,t)$ depends on both, the distance and the time. The proportionality constant, D , is called the diffusion coefficient or diffusivity. Since C is expressed in terms of number of atoms per cubic meter (m^{-3}), then the unit of J_x is $\text{m}^{-2}\text{s}^{-1}$ and that of D is m^2s^{-1} . The negative sign indicates that the concentration decreases with the distance. It is worth mentioning that Eq. 2.1 is

similar to Fourier's equation of heat conduction, which predicts proportionality between the heat flow and temperature gradient and to Ohmic's law too which indicates that the current flux is proportional to the potential gradient. More often the equation is written as:

$$J = -D\nabla C. \quad (2.2)$$

assuming that the medium is isotropically distributed, in which D is the same in all directions. From the definition of the diffusion above, it occurs as a result of the random motion of the diffused particles which are always thermally activated. Thus, the diffusivity, D , is strongly temperature dependent. The relation is expressed as [7]:

$$D = D_o \exp\left(-\frac{Q}{k_B T}\right). \quad (2.3)$$

Where D_o is constant and Q is the activation energy. k_B is Boltzmann's constant. Almost all heat treatments take place at constant temperature; a diffusion coefficient obeying Eq. 2.3 is constant for a given experiment. Eq. 2.3 means that the diffusion coefficient is constant only at constant temperature. This temperature dependence is very practical from technology of materials point of view. For instance, in metallurgical processes, it is common to achieve a certain required configuration of the atoms of the material at high temperature, and then to reduce the temperature as rapidly as possible. This process, identified as quenching, freezes in the high temperature state, which is unlikely to be the correct equilibrium configuration at room temperature. The atoms proceed to diffuse to their correct positions in the crystal. Diffusivity values in solids at room temperature are so low that the accomplishment of equilibrium might take thousands of years [7], which is quite long enough to consider that the state is stable. The distinctive electrical properties of semiconductors are based on the fact that they have two mobile species which carry an electric current, electrons and holes. A semiconductor could be intrinsic, in which the numbers of electrons and holes are the same, n -type, in which the electrons are predominant, or p -type, in which number of holes exceeds that of electrons. A pure semiconductor is intrinsic. The other two types of semiconductor, known as extrinsic, are formed by adding impurities or dopants. The addition of the dopants is normally performed either by adding the material during the crystal growth or by diffusing it in from an external source at a later step. Controlling the doping levels in the semiconductor crystal, it is thus possible to control both the conduction type and magnitude of the conductivity. Recently, semiconductor devices depend on introducing different amounts of n -type and p -type dopants in different parts of the same crystal by combination of diffusion and masking processes. For example, a bipolar transistor is either an n - p - n or p - n - p sandwich.

Fick's second law is obtained by applying the continuity state to Eq. 2.1. The continuity condition states that the rate at which material accumulates in an element is equal to the rate at which it flows in, minus the rate at which it leaves. This gives the diffusion equation (second law of Fick) as:

$$\frac{\partial C}{\partial t} = D \frac{\partial^2 C}{\partial x^2}. \quad (2.4)$$

The mathematical solutions of the diffusion equation depend on the boundary conditions, which are controlled by the physical conditions of the experiment under consideration.

These solutions allow the determination of diffusion coefficient, D , from measurements of the concentration distribution as a function of position and time. Two simple examples are considered which are often relevant for the analysis of experiments.

2.2 Solution of diffusion equation

2.2.1 Thin-film solution

This corresponds to the common case of depositing a thin layer of the diffuser onto the flat surface of the semiconductor sample. The layer then becomes the diffusion source. Solving Fick's law is subject to the condition that the total amount of plated diffusant is constant. For simplicity, it can be considered that the slightly different case of an infinite bar along x direction with the thin layer located at the point ($x = 0$) perpendicular to the bar length. This is preferable since it is a symmetrical situation. The sample, thus the diffusant layer, is raised to the high temperature for diffusion to take place. After a time t , the distribution should be Gaussian which is expressed by:

$$C(x, t) = \frac{B}{t^{1/2}} \exp\left(-\frac{x^2}{4Dt}\right). \quad (2.5)$$

B is constant. This equation obeys Fick's law and the boundary conditions of the experiment in question; it is symmetrical with respect to $x = 0$, C goes to zero as $x \rightarrow \pm \infty$ for $t > 0$, and for $t = 0$ disappears everywhere, except for $x = 0$ where it is infinite. Assuming that the amount of the diffusing material per area, say α , is constant with time according to Eq. 2.5 can be expressed as:

$$\alpha = \int_{-\infty}^{+\infty} \frac{B}{t^{1/2}} \exp\left(-\frac{x^2}{4Dt}\right) dx. \quad (2.6)$$

The mathematical solution of that equation gives $\alpha = 2B (\pi D)^{1/2}$. Thus, the complete thin-layer solution is given as:

$$C(x, t) = \frac{\alpha}{2(\pi Dt)^{1/2}} \exp\left(-\frac{x^2}{4Dt}\right). \quad (2.7)$$

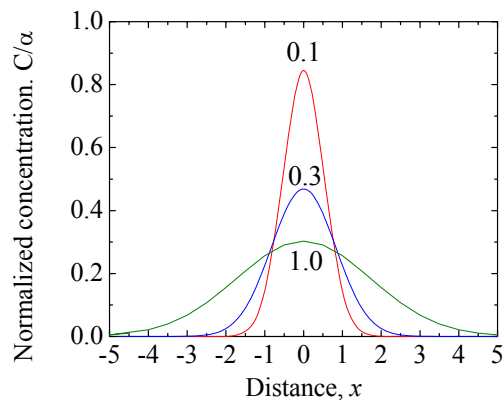


Fig. 2.1: Thin-layer solution of the diffusion equation for various diffusion times, plotted as C/α versus x . The numbers on the curves stands for different values of the quantity Dt .

Figure 2.1 represents Eq. 2.7 for different diffusion times.

The infinite problem is symmetrical. Thus, it can be sliced down in the middle and the solution for $+x$ direction only can be taken. That corresponds to the case of semiconductor diffusion, of a thin layer plated onto a semi-infinite slice. It should be noted that in the infinite problem, half of the mass goes in one direction and half in the other. If a comparable result is to be obtained in the region $x > 0$, this indicates that the amount of material deposited onto the semi-infinite specimen should be half that applied in case of infinite bar. Consider that the amount of diffusant deposited onto the semiconductor specimen is M , then

$$C(x, t) = \frac{M}{(\pi Dt)^{1/2}} \exp\left(-\frac{x^2}{4Dt}\right). \quad (2.8)$$

Taking into consideration that the semi-infinite specimen is one for which the dimension in the diffusion direction is larger than the diffusion depth. The quantity \sqrt{Dt} , so-called diffusion length, is a characteristic distance for the diffusion problems. It has the natural unit of length. For many diffusion experiments the time is selected to make the penetration depth small compared to the thickness of the semiconductor specimen, so the semi-infinite approximation is frequently valid. It is important to note that in case of Cu diffusion in GaAs and GaN the thin-film solution is used most likely for the treatment of the diffusion problem, where a thin layer of Cu deposited on the surface of the samples is used as a diffusion source. At the end of the experiment the layer disappears. Thus, it is also called exhausting layer.

2.2.2 Error function solution

Consider a couple of semi-infinite solid bars, one occupying the space $-\infty < x < 0$, the other occupying $0 < x < \infty$. The two bars are connected at the plane $x=0$, which is normal to the length of the bars. The first bar is homogeneously doped with a solute to a concentration C_s . No solute is contained in the other. Assuming that the two bars are identical, the boundary conditions may be stipulated as:

$$C = C_s \text{ for } x < 0 \text{ at } t = 0$$

$$C = 0 \text{ for } x > 0 \text{ at } t = 0$$

This problem can be easily solved by considering the left hand distribution to be made up of an infinite number of thin-films. The appropriate solution is expressed as:

$$C(x, t) = \frac{C_s}{2} \operatorname{erfc} \left(\frac{x}{2\sqrt{Dt}} \right). \quad (2.9)$$

Thus, the distribution of the diffuser is in the form of a normal function. Where the error function is defined as:

$$\operatorname{erf} z = \frac{2}{\sqrt{\pi}} \int_0^z \exp(-\eta^2) d\eta. \quad (2.10)$$

The complementary error function is expressed as:

$$\operatorname{erfc} z = 1 - \operatorname{erf} z \quad (2.11)$$

One of the common features of the erfc curve is that the value of the function is unity at $x=0$ for all times. Figure 2.2 shows a plot of Eq. (2.9), where the distance is presented in units of $2(Dt)^{1/2}$.

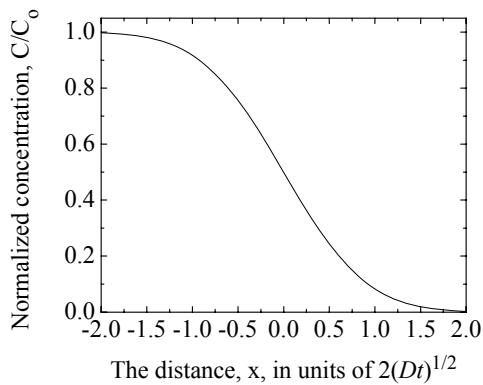


Fig. 2.2: Complementary error function curve plotted against $2(Dt)^{1/2}$ as the unit of length.

Eq. 2.9 indicates that at $x=0$, the concentration is always $1/2C_s$. It follows that for $x>0$, the problem described above is the just like one in which the surface concentration is kept for all times at $1/2C_s$. These conditions are common for diffusion in semiconductors. A semiconductor sample is kept in an ampoule at high temperature for the diffusion to take place, surrounded by a vapor of the

material to be diffused. At the temperature and vapor pressure of the experiment, the solute, diffusant, has a solubility in the semiconductor sample of C_o . Assuming that the surface of the sample achieves this concentration of the solute immediately. Providing that the vapor pressure is constant throughout the experiment, the surface concentration will be maintained at C_o and the diffusion profile can be expressed as

$$C(x,t) = C_o \operatorname{erfc} \left(\frac{x}{2\sqrt{Dt}} \right). \quad (2.12)$$

This profile is similar to Eq. 2.9 where C_o corresponds to $1/2C_s$ and the sample occupies the space $0 < x < \infty$. This solution of diffusion equation is also called constant surface concentration, where it describes the in-diffusion of a diffuser into a semi-infinite semiconductor sample with constant concentration C_o of that species at the surface. Thus, it is applicable to the in-diffusion of a volatile solute (diffusant) into a non-volatile solvent (sample). Another case is the diffusion of a solute from an inexhaustible diffusion source into a sample with solubility C_o . A typical example of such kind is the diffusion of Zn into GaAs and GaP semiconductors.

There are several other solutions for the diffusion equation depending on the initial and boundary conditions such as diffusion from a thick-film, diffusion into an evaporating specimen and diffusion from a growing epitaxial layer. Further details may be found in e.g. [7,8].

2.3 Diffusion mechanisms

Atoms in crystals, as well known in solid-state physics, oscillate around their equilibrium positions. Under certain conditions, these oscillations become large enough to allow an atom to change its site in the crystal. These jumps cause diffusion in solids. Several atomic mechanisms of diffusion in crystals have been identified and are described in what follows.

2.3.1 Diffusion without involvement of native point defects

Interstitially dissolved impurity atoms may diffuse by jumping from interstitial site to interstitial site as shown in Fig. 2.3. No native point defects are involved in this mechanism which is also denoted as direct interstitial diffusion mechanism. Commonly, the diffusivity is very high compared to those of the substitutionally dissolved atoms as can be seen in Fig. 2.4, which shows a survey of the diffusion data for different elements in Si. Examples of such mechanism are the diffusion of Cu, Fe and Li in Si. Oxygen may also diffuse in Si via this mechanism but with very low diffusivity compared to the other elements. Since the oxygen atom in Si occupies the bond centered interstitial positions and is covalently bonded to two Si atoms, it diffuses among only interstitial sites. The bonds breaking is required to allow the diffusion jump and this results in much lower diffusivity than the normal interstitial diffusivity but still higher than that of substitutionally dissolved atoms or dopants. It was suggested that Si self-diffusion in addition to diffusion of group III and group V dopants can be achieved without the involvement of native point defects.

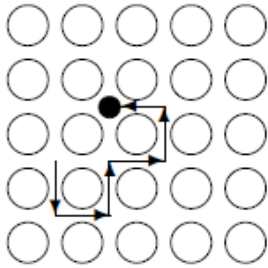


Fig. 2.3: Diffusion without involvement of native point defect (Direct interstitial mechanism).

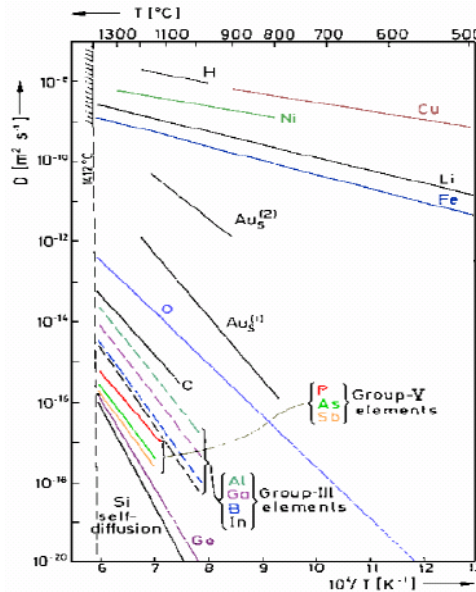


Fig. 2.4: The diffusivity of foreign atoms in silicon and silicon self-diffusion. The lines labeled with $Au_s^{(1)}$ and $Au_s^{(2)}$ correspond to different effective diffusivities of substitutional gold in Si. Taken from Ref. [9].

2.3.2 Simple vacancy exchange and interstitialcy mechanism

The presence of native point defects next to, or in the near vicinity of the substitutionally dissolved atom facilitates its diffusion. In the case of the simple vacancy exchange mechanism, the substitutionally dissolved atom jumps into a vacancy on an adjacent neighbor site of the lattice or sublattice as shown in Fig. 2.5.

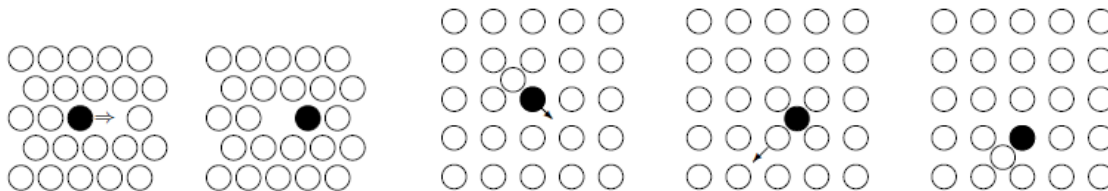


Fig. 2.5: Simple vacancy exchange mechanism, left part. Interstitialcy diffusion mechanism (right part).

In case of interstitialcy mechanism, or what is also called indirect interstitial mechanism, the substitutionally dissolved atom is exchanged by a self-interstitial and pushed into an interstitial site from which it changes over to a neighbor lattice site by pushing out that lattice atom. In contrast to self-diffusion where no pair formation between the lattice atom and native point defects is involved, substitutional impurities, e.g. dopants, can form complexes or pairs with native point defects. These point defect-impurities complexes commonly give rise to higher values of the dopant diffusion coefficient than that in case of self-diffusion, see, e.g. Fig. 2.4. The diffusivity D_S^V of the substitutionally dissolved atoms, in case of simple vacancy exchange, is proportional to the available thermal equilibrium vacancy concentration $D_S^V \propto C_V^{\text{eq}}$. C_V^{eq} depends on some thermodynamic variables which is expressed by [7,9]:

$$C_V^{\text{eq}} = \exp\left(\frac{S^f}{R}\right) \exp\left(-\frac{h^f}{RT}\right), \quad (2.13)$$

where s^f and h^f stand for the formation entropy and enthalpy of the vacancy, respectively. R is the gas constant. Likewise, substitutionally dissolved atoms diffuse via self-interstitial; the diffusivity is expressed as $D_s^I \alpha C_1^{\text{eq}}$. Both vacancies and self-interstitials may contribute to the total diffusivity D_s . Native point defects may also have various charge states x^r . Thus, the self-interstitial and vacancy contributions to the diffusivity under intrinsic and thermal equilibrium concentration can be expressed by [9]:

$$D_s(n) = \sum_x D_s^{x^r}(n_i) D_s^{I^r}(n_i) + D_s^{V^r}(n_i). \quad (2.14)$$

The summation is taken over the native point defects x for a given charge state r , where D_s is expressed as a function of the electron concentration n . n_i denotes the intrinsic carrier concentration.

2.3.3 Divacancy mechanism

Substitutional dissolved impurity atoms, or dopants, can also diffuse via bound pairs of vacancies (denoted as vacancy pairs or divacancy) as shown in Fig. 2.6.

Under thermal equilibrium condition, the monovacancies combine together and form divacancies according to the reaction [7]:

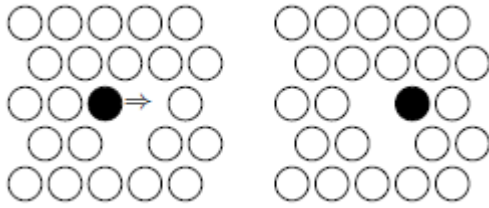


Fig. 2.6: Divacancy mechanism of diffusion.

Thus, the equilibrium concentration of divacancy depends on that of mono-vacancy and can be expressed according to the mass action law as:

$$C_{2V}^{\text{eq}} = K C_V^{\text{eq}}. \quad (2.16)$$

K is the proportionality constant, it is known as equilibrium constant or mass action constant. At high temperatures, the divacancies concentration C_{2V}^{eq} becomes more significant. This is based on the fact that under thermal equilibrium, monovacancy concentration C_V^{eq} increases with the increasing temperature. In case of face centered cubic (fcc) metals, divacancies have a mobility higher than that of monovacancies [10] what leads to some contribution of divacancies in addition to the vacancy mechanism.

2.3.4 Interstitial-Substitutional exchange mechanisms

In semiconductors, a considerable number of impurities, A , is present as interstitial-substitutional, i-s, species. Mainly, they are dissolved on substitutional sites, A_s , but achieve diffusion by changing into an interstitial configuration, A_i , in which their diffusivity D_i is tremendously higher than D_s whereas the opposite is true for the solubilities, for example Zn, Mn, Cr, Fe and Be in GaAs and Pt, Zn and Au in Si. The switching from a substitutional to interstitial sites or vice versa requires the participation of native point defects. There are two forms of the changing over between

the interstitial and substitutional sites for uncharged species. One is the Frank-Turnbull mechanism [11] which involves vacancies and can be expressed as,



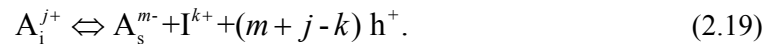
and the second is the kick-out mechanism [12] involving self-interstitials described by:



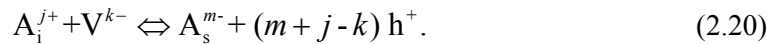
where I denotes self-interstitial. Both mechanisms are schematically represented in Fig. 2.7.

In case of III-V compound semiconductors even regular p -type dopants such as Zn, Mg or Be diffuse by the interstitial-substitutional mechanism. In such cases the charge state of the involved species should be considered.

The kick-out mechanism can be written as [9]:



Where j , k and m are integers standing for the charge state of the species and h^+ stands for the holes [13,14]. The self-interstitial is assumed to be made of the atomic species which forms the sublattice on which the substitutional impurity atom is dissolved, for instance, sulfur (S) substitutes on As sublattice in GaAs and thus creates As self-interstitials. The corresponding equation of the Frank-Turnbull mechanism can be expressed as [9]:



Generally, the native point defects in addition to the interstitial impurities may take place in more than one charge state.

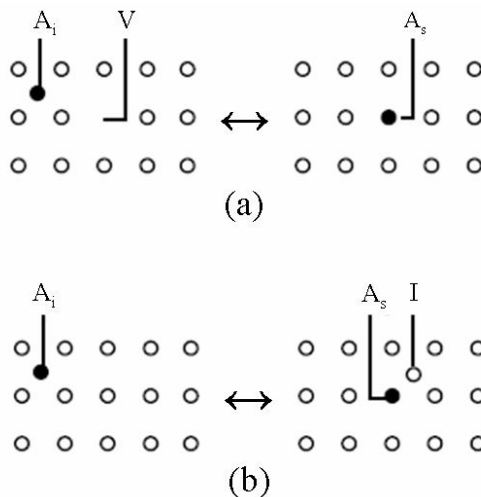


Fig. 2.7: Schematic representation of interstitial-substitutional exchange mechanisms of impurity atom diffusion. Frank-Turnbull mechanism (a) and kick-out mechanism (b).

The Frank-Turnbull mechanism is also denoted as dissociative mechanism (sometimes also Longini mechanism). Cu diffuses rapidly in Ge via the dissociative mechanism [15]. It is worth noting that the kick-out mechanism is the dynamic form of the Watkins replacement mechanism [16] in which a self-interstitial generated by low temperature electron irradiation pushes a substitutional atom into an interstitial site. The fast diffusion of Cu in GaAs has been attributed to the kick-out mechanism [11,17,18]. Au, Zn and Pt diffuse very fast in Si via this mechanism too [19,20]. Kick-out and interstitialcy mechanisms are very close to each other. The most important difference is: the foreign atom once in an interstitial site stays for many steps in kick-out mechanism but for only one step in case of interstitialcy mechanism. On the other hand, the vacancy exchange and Frank-Turnbull mechanisms are qualitatively different. In the vacancy exchange mechanism the diffusivity is enhanced with increasing the vacancy concentration. However, in case of the Frank-Turnbull mechanism, the effective diffusivity of the substitutional species decreases with increasing the vacancy concentration. The description of the diffusion

behavior of atoms changing by means of kick-out or Frank-Turnbull mechanisms requires the solution of a coupled system of three differential equations describing diffusion and reaction of A_i , A_s and the involved native point defect (either I or V). The solution of these equations can be obtained by numerical methods. More details can be found in the literature [19,20].

2.3.5 Recombination-enhanced Diffusion

In semiconductors, the transfer of the energy associated with the recombination of electrons and holes to the vibrational modes of the defects and their surroundings may enhance the thermally activated diffusion of defects. This has been distinguished early by Weeks et al. [21] and described theoretically [22]. The concentration of electrons and holes above the thermal equilibrium values can be influenced by particle irradiation, e.g. electron irradiation [23], by ion implantation or via plasma exposure [24] and optical excitation [21]. Carrier injection in devices [25] or the tip of a scanning tunneling microscopy (STM) [26] could also be used in order to induce higher concentration of electrons and holes. Consequently, the thermal activation energy of the diffusion may be reduced significantly or may even become effectively zero; this type of recombination enhanced diffusion is named as ‘athermal diffusion’. An example of athermal diffusion is the long-range diffusion of radiation-induced silicon self-interstitials at liquid helium temperatures, where the electron-hole excitation is expected to be induced via the particle irradiation. The recombination-enhanced diffusion of defects is technologically important in devices such as lasers, transistors and light-emitting diodes. The carrier injection during operation in these devices may cause unwanted movement of the defects. This movement may lead to a defect rearrangement, e.g. dislocation climb, influencing the functioning of the device adversely.

2.4 Techniques for studying the diffusion profiles

The diffusion coefficient and surface concentration are the important parameters which should be determined in a diffusion experiment. Several techniques can be used to obtain these parameters. The most suitable one depends on the details of the experiment under consideration.

2.4.1 Radiotracer method

The most direct way of obtaining the distribution of an element in a solid is to mark it by using a radioactive isotope of the element. As shown schematically in Fig. 2.8 the tracer is placed on a flat surface of the diffusion sample. It is more common that a radioactive isotope of the species under investigation is utilized as a tracer. The tracer deposition can be carried out in several ways, e.g. evaporation, dropping of a liquid solution or electrodeposition of the tracer onto the sample surface. In certain cases the tracer is ion-implanted as a thin layer underneath the surface of the sample to avoid the disturbing surface oxide keep-up and solubility problems. The sample is normally sealed in a quartz ampoule under vacuum or inert gas, for instance Argon. An isothermal annealing of the sample is carried out at temperature T for diffusion time t . At the end of the diffusion experiment the specimen is taken out. A thin layer is eliminated from the surface. The radioactivity of the layer is detected and compared with that from a standard sample of the doping element. The radioactivity can be appropriately determined by nuclear counting facilities (γ - or β -detectors, it is governed by the isotope). The standard sample has to be of the same radioactive level as that used in the diffusion and its weight is known. The weight of the element can be determined. Then, the mean concentration of the element in the layer can be obtained if its dimensions are known. The diffusion

profile of the element is plotted by removing further layers and repeating the same process. The difference between the isotope and the non-radioactive element in the sample cannot be obtained. The thickness of each layer should be so thin that there is no distinct difference in the concentration between the top and the bottom surfaces. It is preferable for the half-life of the used isotope to be longer than the diffusion experiment period. If it is shorter, then the decay must be taken into account.

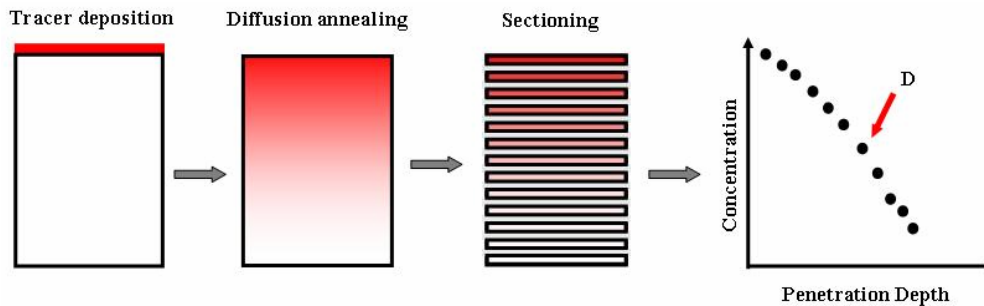


Fig. 2.8: Schematic illustration of the tracer method. The main steps, tracer deposition, diffusion annealing, serial sectioning and estimation of the depth profile are shown.

The accuracy of the plotted profile depends on the care with which sectioning and counting procedure is performed. Removing thin layers from the surface can be done through two methods. The surface can be scraped, i.e. mechanically polished. In this way the surface should be polished at right angles where a bevel of just few degrees leads to imprecise results. The second method, more recommended, is the chemical etching of the layers. Once the diffusion profile is plotted, the diffusion coefficient and diffusion mechanism can be obtained. The depth diffusion profile is described by Eq. (2.8) as long as the experimental conditions were chosen where the tracer layer is thin compared to the mean diffusion length. A logarithm of the concentration as a function of the squared depth is linear relationship according to Eq. (2.8). The diffusivity can be estimated from the slope and the diffusion time t . The tracer method has a noticeable advantage, the determination of the absolute tracer concentration is not essential.

2.4.2 Other Profiling and Detection Techniques

Several other profiling and detection methods can be used to measure concentration-depth profiles. The important ones are:

2.4.2.1 Secondary Ion Mass Spectrometry (SIMS)

SIMS is described in details in section 3.5.2. It is predominantly appropriate for the diffusion of foreign elements. In contrast to self-diffusion studies by radiotracer methods, in the case of stable tracers the concentration range of the diffusion profile is limited by the natural profusion of the stable isotope in the matrix. SIMS has the ability to distinguish between the different isotopes of the same element.

2.4.2.2 Auger Electron Spectroscopy (AES)

AES together with sputter profiling can be used to measure diffusion profiles in the range of several nm to several μm . AES distinguishes only between different elements. Thus, it is appropriate only in case of the diffusion of foreign atoms.

2.4.2.3 Rutherford Backscattering Spectrometry (RBS)

A high energy beam of monoenergetic α -particles or protons is applied in RBS experiments. These particles are scattered by heavy nuclei in the sample. Then, the concentration depth distribution of scattering nuclei can be determined from the energy spectrum of scattered α -particles (in case of using beam of α -particles). RBS technique is mostly appropriate for identifying the heavy elements in a matrix of considerably lower atomic weight. The profile depth is limited to less than a few μm because of the energy straggling of the incident beam.

2.4.2.4 Nuclear Reaction Analysis (NRA)

The diffusion of light elements can be investigated using high energy particles in case of the nuclei undergo a suitable resonant nuclear reaction. A good example is diffusion of boron in an alloy. α -particles are emitted in the course of the irradiation with high energy protons according to the nuclear reaction $^{11}\text{B} + \text{p} \rightarrow ^8\text{B} + \alpha$ [27]. The number and energy of emitted α -particles as a function of the incident proton energy is used for estimation of the concentration profile of ^{11}B . The energy straggling limits the depth resolution of NRA. Both techniques, RBS and NRA, require a depth calibration which is not usually based on very accurate data for the stopping power in the matrix for those particles released by the nuclear reaction. The depth resolution of NRA is less than that of radiotracer and SIMS profiling techniques. Further details about profiling techniques can be found in Ref. [27].

2.5 Thermodynamics of point defects in GaAs

The whole point defects in a crystal include those existing in a chemically perfect crystal (pure material), intrinsic defects, and those related with foreign atoms. The latter is called impurities if they are introduced inadvertently and termed dopants in case of they are consciously added. There are six main intrinsic point defects in gallium arsenide (GaAs): vacancies on both sublattices (V_{Ga} and V_{As}), Ga and As self-interstitials (I_{Ga} and I_{As}) and Ga and As anti-sites (Ga_{As} and As_{Ga} , respectively). Commonly, the expression “native defects” is related to the point defects which are in thermodynamic equilibrium with a host crystal and not introduced intentionally, e.g. by crystal deformation or irradiation. The equilibrium concentration of point defects in III-V compound semiconductors, e.g. GaAs, is a complicated function. It depends on the temperature, Fermi-level and activity of either one of the constituents (Ga or As), i.e. the crystal stoichiometry. Most likely, it depends on the vapor pressure of the more volatile component.

2.5.1 GaAs system

GaAs crystallizes in the zincblende structure at about 1513 K. The lattice constant is 0.5653 nm at 300 K [28]. At a given temperature, a III-V compound has a thermodynamically allowed region of homogeneity for $\text{Ga}_{1-x}\text{As}_x$. This is shown on the binary phase diagram in Fig. 2.9. The homogeneity region is represented by the shaded area within the solidus line a*-b*.

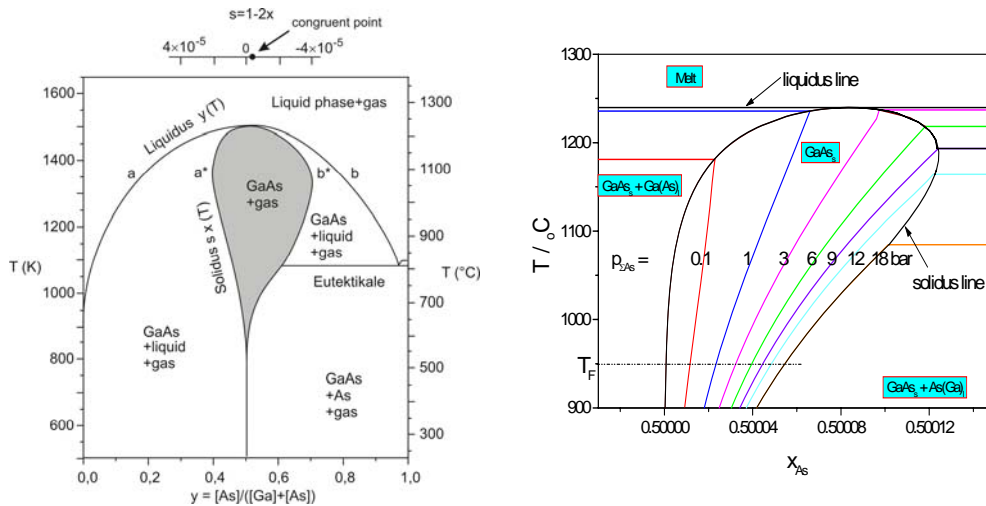


Fig. 2.9: Phase diagram of the GaAs system with thermodynamically allowed composition range greatly exaggerated. The figures are taken from Refs. [29,30] (left) and [31] (right).

The deviation of the compound composition from the stringent stoichiometry of $\text{Ga}_{0.5}\text{As}_{0.5}$ is constituted by the sum of all point defects. Therefore, within the thermodynamically allowed range the thermal equilibrium concentrations of native point defects in both sublattices change with the crystal composition deviations. The recent calculations [Fig. 2.9 (right)] showed that the deviation takes place only on As-rich side. The only suitable and dependable measure of the crystal composition is the vapor phase pressure, preferably of the more volatile group V element, either during the crystal growth or annealing. If the concentration of one of the components (e.g., As) goes beyond the value allowed by the solidus line b^* , the system consists of three phases – GaAs crystal, melt and gas. Both, the GaAs crystal and its gas phase are in thermal equilibrium in the homogeneity region surrounded by the solidus line.

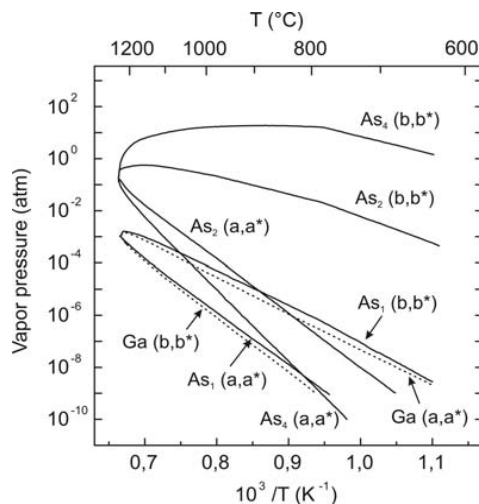


Fig. 2.10: Partial pressures of As , As_2 , As_4 in equilibrium with the most Ga rich ((a,a*) curves) and the most As rich GaAs ((b,b*) curves). (From Ref. [32])

Fig. 2.10 represents the corresponding vapor pressures determined along the solidus line. The four vapor phases, Ga_1 , As_1 , As_2 , and As_4 are in thermal equilibrium coexistence with the GaAs crystal as well as among themselves. Thus, in treating the point defect problem, it is sufficient to consider the role of only one of them, e.g. that of As_4 . In case of the arsenic-rich melt, the As_4 -pressure (P_{As_4}) governs whereas the vapor pressure of gallium is negligibly small. The resultant pressure is thus $\sim P_{\text{As}_4}$. On the gallium-rich side, As_2 is the dominating gas component. The Ga pressure (P_{Ga}) is important only at lower temperatures ($T < 800$ °C). The exact structure of the GaAs phase

diagram is unidentified at present. This question is still under consideration. The thermodynamic calculations [31] showed that there is no crystallization at all possible on the Ga-rich side [Fig. 2.9 (right)]. This may account for the fact that gallium precipitates were never observed even in the crystals grown from a very Ga-rich melt [33]. However, stronger experimental evidence is needed for the Wenzl's assumption. It is more frequently accepted that the congruent point, where the solidus and liquidus lines oscillate, lies on the As-rich side of the phase diagram (Fig. 2.9). Hence, growth from a stoichiometric melt always produces As-rich material [29,34]. The deviation from stoichiometry s is understood through the creation of point defects on both sublattices. The deviation is described as [29]:

$s = 1 - 2x = s_1 - s_2$, where s_1 and s_2 are expressed as:

$$\begin{aligned} 2s_1 &= [I_{Ga}] + [Ga_{As}] - [V_{Ga}] - [As_{Ga}] - [X_{Ga}], \\ 2s_2 &= [I_{As}] + [As_{Ga}] - [V_{As}] - [Ga_{As}] - [X_{As}] \end{aligned} \quad (2.21)$$

X_{Ga} and X_{As} stand for an arbitrary foreign atom on the Ga and As sublattice, respectively. The brackets represent defect concentration in atomic units. The type and concentration of the dominating point defects can thus be determined by measuring the stoichiometry deviation s . Two direct methods can be used for the estimation of s : 1) determination of the amounts of both Ga and As atoms in a given sample by means of the electrochemical titration method of one or both the species. 2) Estimation the average mass of the unit cell in the sample through measuring its density (the mass per unit volume of crystal) and the cube of its lattice parameter (the volume of the unit cell). The quotient of these two amounts is, therefore, the mass per unit cell. Subtracting from this the mass of an ideal unit cell (containing one Ga and one As atom), the excess mass per unit cell which is associate with the deviation from stoichiometry is obtained. A study of GaAs crystals grown from As-rich and Ga-rich melt using the above approaches demonstrated the dominance of deviations on the As sublattice [34]. Hence, at As-rich conditions, there are large concentrations of I_{As} and V_{Ga} grown into the crystals at the melting point. However, information on the dominating defects only, remain in the crystal after its cooling, can be obtained from s . This method cannot be used for investigating other point defects which may exist at high temperatures. Generally, there are some point defects present in the crystal at thermodynamic equilibrium. Those lead to minimization of the Gibbs free energy. The equilibrium concentrations of point defects in compound semiconductors depend on the crystal stoichiometry in addition to the temperature and Fermi level position, i.e. the defect concentration, crystal composition and ambient vapor pressure are in thermodynamic equilibrium and depend on each other. Additionally, point defects may exist in more than one charge state and interact strongly through their effect on the Fermi energy. The charged native point defects grown into the crystal play a strong role in dopant solubility and on the other hand, doping noticeably influences populations of the charged native point defect.

2.5.2 Chemistry of point defects in GaAs

Defect chemistry can be considered as a chemical approach to the problems dealing with defects in crystalline solids. It takes into consideration the generation of defects, interaction between them and between defects and ambient, since it is assumed that the crystal is in an equilibrium state for chemical reactions [35]. In GaAs, there are six point defects (in neutral states). They can be described by the following thermodynamic reactions [34]:



$$\text{Ga}_{\text{Ga}} = \text{V}_{\text{Ga}}^0 + \text{I}_{\text{Ga}}^0 \quad (2.25)$$

$$\text{I}_{\text{As}}^0 + \text{V}_{\text{Ga}}^0 = \text{As}_{\text{Ga}}^0 \quad (2.26)$$

$$\text{I}_{\text{Ga}}^0 + \text{V}_{\text{As}}^0 = \text{Ga}_{\text{As}}^0 \quad (2.27)$$

The superscript (0) denotes the neutral state. The external phase is involved in only one of the reactions (Eq. 2.22). It is possibly liquid or vapor. To avoid writing different equations for the two cases, the activity of the external phase is expressed in terms of the partial pressure of As dimers which would be in equilibrium either with the vapor or with a liquid which is in equilibrium with that vapor. The arsenic tetramer is selected because it is the dominating species in arsenic vapor (Fig. 2.10). Having articulated a condition of equilibrium of one component with the external phase, equilibrium relating to the other component (Ga) is described in terms of the partial pressure as [34]:

$$P_{\text{Ga}} P_{\text{As}_4}^{1/4} = \exp(-g^f / k_B T). \quad (2.28)$$

P_{Ga} is the partial pressure of gallium monomers. g^f represents the free energy of formation of GaAs from gaseous gallium monomer and arsenic tetramers at one atmosphere total pressure and temperature T. The reaction of V_{Ga} can be expressed by substituting Eq. 2.22 into Eq. 2.23 as follows:

$$\text{As}_{\text{As}} = \text{V}_{\text{As}}^0 + 1/4 \text{As}_4(\text{v}), \quad (2.29)$$

And that of V_{Ga} may be inferred from Eqs. (2.24) and (2.29)

$$1/4 \text{As}_4(\text{v}) = \text{V}_{\text{Ga}}^0 + \text{As}_{\text{As}}. \quad (2.30)$$

The mass-action law [36] is used to determine the concentration of point defects.

$$[\text{V}_{\text{Ga}}^0] = K_{\text{V}_{\text{Ga}}}(\text{T}) P_{\text{As}_4}^{1/4} \quad (2.31)$$

$$[\text{V}_{\text{As}}^0] = K_{\text{V}_{\text{As}}}(\text{T}) P_{\text{As}_4}^{-1/4} \quad (2.32)$$

$K_{\text{V}_{\text{Ga}}}$ and $K_{\text{V}_{\text{As}}}$ stand for the mass action constants of formation of gallium and arsenic vacancies, respectively. Eqs. 2.31 and 2.32 indicate that the concentration of V_{Ga} should increase and that of V_{As} decrease with increasing the arsenic vapor pressure. In case, the vacancies are charged, their ionization reactions and corresponding concentrations are described as follows [34]:

For V_{As} ,

$$\text{V}_{\text{As}}^0 = \text{V}_{\text{As}}^+ + e^- \quad (2.33)$$

$$[\text{V}_{\text{As}}^+] = [\text{V}_{\text{As}}^0] (N_c / n) \exp(-E_{\text{V}_{\text{As}}} / k_B T) \quad (2.34)$$

$$\text{V}_{\text{As}}^0 = \text{V}_{\text{As}}^- + h^+ \quad (2.35)$$

$$[\text{V}_{\text{As}}^-] = [\text{V}_{\text{As}}^0] (n / N_c) \exp(-E_{\text{V}_{\text{As}}} / k_B T) \quad (2.36)$$

Gallium vacancy

$$\text{V}_{\text{Ga}}^0 = \text{V}_{\text{Ga}}^{q-} + qh^+ \quad (2.37)$$

$$[\text{V}_{\text{Ga}}^{q-}] = [\text{V}_{\text{Ga}}^0] (n / N_c)^q \exp \left\{ \left(qE_g - \sum_q E_{\text{V}_{\text{Ga}}}^{q-} \right) / k_B T \right\} \quad (2.38)$$

E_g denotes the energy gap and $q=1,2,3$. $E_{\text{V}_{\text{As}}}$ is the ionization energy of arsenic vacancy and $E_{\text{V}_{\text{As}}}^{q-}$ is that of the q charge state of the gallium vacancy. n is the free electron density and N_c is the effective density of conduction-band states. However, these considerations give a quantitative description of vacancy formation and can be applied only if the mass action constants are known.

Tan et al. evaluated explicitly the concentration of equilibrium point defects [37,38]. The concentrations of neutral gallium and arsenic vacancies are expressed as:

$$[V_{\text{Ga}}^0] = (P_{\text{As}_4}/B_{\text{As}_4})^{1/4} \exp\left(-[g^f(V_{\text{Ga}}^0) - \delta g_{\text{As}}]/k_{\text{B}}T\right) \quad (2.39)$$

$$[V_{\text{As}}^0] = (B_{\text{As}_4}/P_{\text{As}_4})^{1/4} \exp\left(-[g^f(V_{\text{As}}^0) - \delta g_{\text{As}}]/k_{\text{B}}T\right) \quad (2.40)$$

$g^f(V_{\text{Ga}}^0)$ and $g^f(V_{\text{As}}^0)$ are the free energies of formation of neutral gallium and arsenic vacancies, respectively. δg_{As} is the difference and defined as:

$$\delta g_{\text{As}} = g_{\text{As}}(\text{GaAs}) - g_{\text{As}}(\text{As}_4). \quad (2.41)$$

$g_{\text{As}}(\text{GaAs})$ is the free energy of bonding an arsenic atom in the crystal and $g_{\text{As}}(\text{As}_4)$ is that of bonding of an As atom in the tetramer molecule. B_{As_4} is the gas constant and defined as $B_{\text{As}_4} = (2\pi m_{\text{As}_4}/h^2)^{3/2} (k_{\text{B}}T)^{5/2}$, assuming that As_4 is an ideal gas, where m_{As_4} is the mass of As_4 molecule and h is Planck's constant. The concentration of the charged defects is determined, according to this method [38], by:

$$[V_{\text{Ga}}^z] = [V_{\text{Ga}}^0] \exp\left\{\left(zE_f - \sum_{m=1}^z E_{am}\right)/k_{\text{B}}T\right\} \quad (2.42)$$

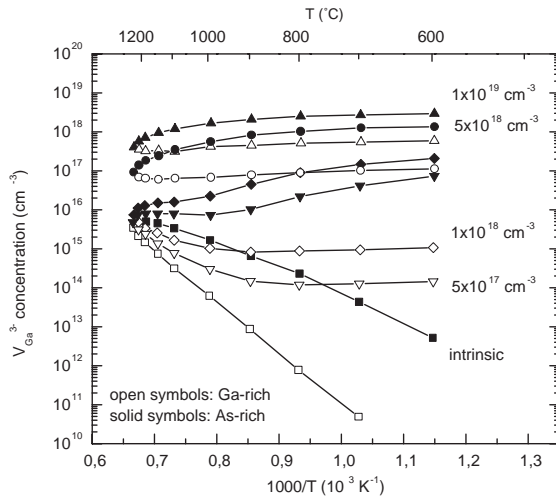


Fig. 2.11: Thermal equilibrium concentrations of V_{Ga}^{3-} in n -type GaAs, doped to different concentrations, calculated as a function of temperature [37,39].

E_f is the Fermi energy. z is the charge and E_{am} are the ionization energies of V_{Ga} measured from the valance band. Eq. 2.42 indicates that the concentration of the charged vacancy increases as the Fermi level position moves toward the conduction band bottom.

Physically, this can be attributed to the energy difference $E_f - E_a$ gained by the whole system (GaAs crystal) during the process of electron transition to the acceptor level E_a , i.e. formation of an additional acceptor. Since the concentration of the charge carrier reflects the position of the Fermi level, thus the dependence of the concentration of the charged point defect in a semiconductor on the charge carrier concentration is dubbed as Fermi level effect. The V_{Ga} concentration is calculated [40], where it was assumed that V_{Ga} is the only acceptor in the crystal. The As pressures corresponded to those illustrated in Fig. 2.10. The entropy terms are not included in the Gibbs free energies in Eqs. (2.39, 2.40). This means that Gibbs free energies were set equal to the corresponding formation enthalpies h^f , where $h_{V_{\text{Ga}}^0}^f = 2.59$ eV [41] and $\delta h_{\text{As}} = -0.69$ eV were applied. The data of ionization energies of V_{Ga} were taken from Ref. [42]. The results of the calculations carried out for different free electron concentrations in n -type GaAs are illustrated in Fig. 2.11. The concentration of V_{Ga} , in intrinsic material, has been found to increase with

increasing the temperature. On the other hand, the doped material showed a weak temperature dependence of $[V_{\text{Ga}}^{3-}]$. At high doping level, E_f is expected to be very close to the edge of conduction band whatever the temperature is. This may lead to temperature independence or even a small negative temperature dependence of the $[V_{\text{Ga}}^{3-}]$ [38]. A positron annihilation study of Te-doped GaAs gave the first experimental evidence of this effect [43]. In this study the formation enthalpy $h_{V_{\text{Ga}}^0}^f$ in addition to the formation entropy $s_{V_{\text{Ga}}^0}^f$ was taken into consideration and their values were estimated to be (3.2 ± 0.5) eV and $(9.6 \pm 1)k_B$, respectively.

2.6 Diffusion in GaAs

GaAs has received much attention owing to its important applications, which ranges from fast electronic to optoelectronic devices such as lasers. It is also used for the fabrications of superlattice structures. The diffusion of many elements in GaAs has been widely investigated [36]. Mainly, these studies focused on most important p -type dopants Zn, Be and n -type dopants Si, Se and Cr. As mentioned above, Zn, Be and a number of other elements diffuse by means of an interstitial-substitutional mechanism. Self-diffusion in GaAs is studied but with the advances in growing GaAs/AlAs-type superlattices utilizing molecular beam epitaxy (MBE) or metal organic chemical vapor deposition (MOCVD) methods. Al has acted as a significant foreign tracer element for explaining Ga self-diffusion mechanisms. The fabrication of laterally structured optoelectronic devices by locally disordering superlattices is opened up by the observation that the high concentration Zn diffusion into a GaAs/Al_xGa_{1-x}As superlattice causes a strong increase in the Al-Ga interdiffusion [44]. The role of self-interstitials and vacancies was established from the dependence of the diffusion processes on the As vapor pressure.

2.6.1 Gallium self-diffusion

The self-diffusion coefficient of Ga $D_{\text{Ga}}(n_i)$ in GaAs under intrinsic conditions has been measured [45,46] using radioactive tracer Ga atoms. These results are shown in Fig. 2.12.

This technique permits measurements of D down to 10^{-19} m²s⁻¹. The interdiffusion measurements of Ga and Al in GaAs/Al_xGa_{1-x}As superlattices allowed measuring much lower values [47]. The results have been fitted to the expression [48].

$$D_{\text{Ga}}^V(n_i) = 2.9 \times 10^8 \exp(-6 \text{ eV}/k_B T) \text{ cm}^2 \text{ s}^{-1}. \quad (2.43)$$

T is the absolute temperature and $D_{\text{Ga}}(n_i)$ stands for the gallium diffusivity under intrinsic and thermal equilibrium conditions. Eq. 2.43 is valid for GaAs crystals at As-rich composition. The superscript V in the quantity D_{Ga}^V indicates that the quantity is owing to the sublattice vacancy contribution to Ga self-diffusion. It was observed that at about 1 atm (1.0133 bar) of As₄ pressure, the disordering rate of the GaAs/Al_xGa_{1-x}As superlattices increases with increasing the ambient As₄ pressure [49]. The corresponding D_{Ga}^V values for GaAs crystals at the Ga-rich boundary condition can then be described as [9]:

$$D_{\text{Ga}}^V(n_i) = 3.93 \times 10^8 \exp(-7.34 \text{ eV}/k_B T) \text{ cm}^2 \text{ s}^{-1}. \quad (2.44)$$

It is turned out that triply negatively charged Ga vacancy V_{Ga}^{3-} is the responsible vacancy species. The Al-Ga interdiffusion coefficient is observed to increase at very low arsenic pressures. The role of V_{Ga} and I_{Ga} will become more clear below, when Ga diffusion in doped GaAs/Al_xGa_{1-x}As superlattices is considered and when considering also the p -type dopants Be and Zn.

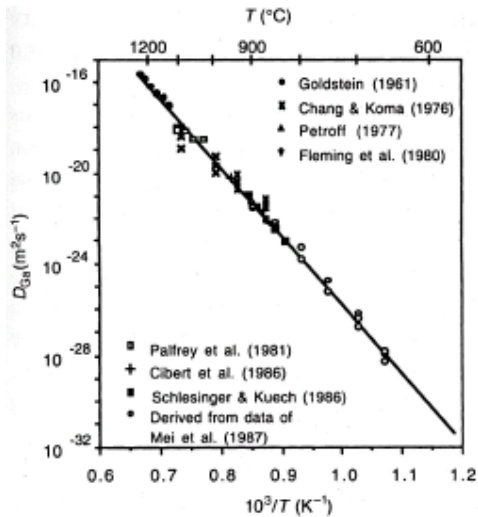


Fig. 2.12: Ga self-diffusion in GaAs and Ga-Al interdiffusion in GaAs/AlGaAs superlattice under intrinsic condition. (Ref. [9])

The Ga self-diffusion coefficient under Ga-rich composition is inferred from combining Al-Ga interdiffusion studies [50] and Zn and Cr diffusion [51-53]:

$$D_{\text{Ga}}^{\text{I}}(n_i) = 4.46 \times 10^{-8} \exp(-3.37 \text{ eV}/k_{\text{B}}T) \text{ cm}^2 \text{ s}^{-1}. \quad (2.45)$$

The corresponding values for GaAs crystals under As-rich boundary are expressed as:

$$D_{\text{Ga}}^{\text{I}}(n_i) = 6.05 \times 10^{-4} \exp(-4.71 \text{ eV}/k_{\text{B}}T) \text{ cm}^2 \text{ s}^{-1}. \quad (2.46)$$

The data of Ga self-diffusion studies using stable Ga isotopes [54,55] are fitted by:

$$D_{\text{Ga}}(n_i) = 4.3 \times 10^3 \exp(-4.24 \text{ eV}/k_{\text{B}}T) \text{ cm}^2 \text{ s}^{-1} \quad (2.47)$$

instead of Eq. 2.43. There is no reasonable explanation of the discrepancy between Eq. 2.43 and other expressions such as Eq. 2.47. According to the Fermi level effect, the Ga diffusion activation energy decreases by ~ 2 eV in n -doped GaAs [40]. This means that Eq. 2.43 is more acceptable. There are some reasons which may affect the accuracy of the experimental results. They comprise unintentional contamination by n -type nominal intrinsic materials and the fact that the materials did not have the As-rich composition to start with and the experimental time-temperature condition was not enough to convert the materials to As-rich for most of the experimental time [9]. The observed dopant enhanced Al-Ga interdiffusion is ascribed to two important effects [18,48]. 1) The enhancement of thermal equilibrium concentration of properly charged point defects by doping (Fermi level effect). In case of the n -type dopant Si, only the existence of the dopant is important, not its movement. Compensation doping, for instance with Si and Be, should not enhance the Al-Ga interdiffusion. 2) For a dopant with high diffusivity and solubility, where the product $D_{\text{S}}C_{\text{S}} \gg D^{\text{SD}}(n, p)$ holds, then the nonequilibrium native point defects are created. SD stands for self-diffusion. The enhanced disordering rate because of the effect of Fermi level may be further increased or decreased, depending on the development of a supersaturation or undersaturation of point defects. Such nonequilibrium native point defects drive the dopant diffused region crystal first toward a suitable allowed GaAs crystal composition. When the supersaturation or undersaturation of point defects becomes so large that the crystal local region goes beyond the allowed composition limit, extended defects are created to bring the composition of the region back to that composition boundary. Then, this allows describing the diffusion processes by an equilibrium point defect process suitable for the crystal local region, which is at an appropriate allowed composition boundary. The crystal is in a nonequilibrium state due to the spatially changing composition. The diffusion of high concentration Zn and Be in GaAs [51,56] and their effects on GaAs/Al_xGa_{1-x}As superlattices [57] seems to be such cases. The identification of the type and charge state of the native point defect dominating Ga self-diffusion in n -type GaAs is allowed

from studies of Al-Ga interdiffusion in n -type Si doped GaAs. Fig. 2.13 shows the enhanced Al-Ga interdiffusion coefficients under Si doping plotted as a function of the (n/n_i) of the appropriate temperature.

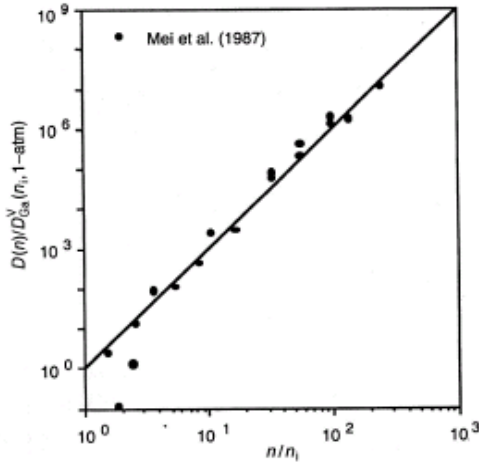


Fig. 2.13: The $(n/n_i)^3$ dependence of Al-Ga interdiffusion data of Mei et al. [58]. $D_{\text{Ga}}^{\text{V}}(n_i)$ is described by Eq. 2.43.

The data, obtained by Mei et al. [58], show a clear doping dependence described by [48]:

$$D_{\text{Al-Ga}}(n) = D_{\text{Ga}}(n_i)(n/n_i)^3, \quad (2.48)$$

where $D_{\text{Ga}}(n_i)$ is given by Eq. 2.43

Equation 2.48 shows clearly the involvement of a triply negatively charged native point defect species. The pressure dependence of interdiffusion coefficient of n -type superlattices [59] showed that this defect can only be the gallium vacancy $\text{V}_{\text{Ga}}^{3-}$. Taking into account the As vapor pressure, the Ga self-diffusion coefficient in n -type GaAs can thus be expressed as [9]:

$$D_{\text{Ga}}(n, P_{\text{As}}) = D_{\text{Ga}}^{\text{V}}(n_i)(n/n_i)^3 (P_{\text{As}})^{1/4}. \quad (2.49)$$

Equation 2.49 is valid for the n -doping level being adequately high. Moreover, a weak dependence of the $D_{\text{Ga}}(n_i)$ on the doping concentration than expected from Eq. 2.49 is shown in tellurium-doped GaAs based superlattices [60]. This is more probably owing to clustering; a part of Te atoms is electrically inactive and does not contribute to the electron concentration [61]. As shown in Fig. 2.14, Tan and Gösele [57] fitted the Al-Ga interdiffusion data in p -type GaAs based superlattices by:

$$D_{\text{Al-Ga}}(p) = D_{\text{Ga}}^{\text{I}}(n_i)(p/n_i)^2 \quad (2.50)$$

where $D_{\text{Ga}}^{\text{I}}(n_i)$ is determined by Eq. 2.45. Eq. 2.50 indicates that the dominant native point defects under p -doping with high enough carrier concentration are the Ga self-interstitials. The p^2 dependence of $D_{\text{Al-Ga}}(p)$ illustrates that the Ga self-interstitials are doubly positively charged.

The data presented in Fig 2.14 are under the dopant in-diffusion conditions. Under out-diffusion conditions, the dopant diffusivity values are so small that they cannot be consistently measured. The large difference between the results for in- and out-diffusion is owing to the nonequilibrium concentrations of native point defects induced by high concentration diffusion of the dopants, such as Zn and Be [9]. Contrary to the group II acceptors Zn and Be, the group IV acceptor carbon (C) substitutes on the As sublattices. It diffuses slowly. This permits the native point defects to be kept at their thermal equilibrium values. The prevalence of Ga self interstitials in Ga self-diffusion is verified by the pressure dependence of disordering of p -type superlattices [62].

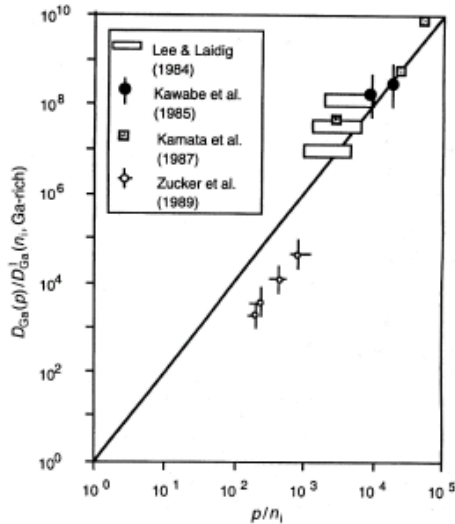


Fig. 2.14: Fitting of some *p*-dopant enhanced Al-Ga interdiffusion data. $D_{Ga}^I(n_i)$ is determined by Eq. 2.45. The data fitting shows an approximate quadratic dependence of (p/n_i) . The figure is taken from Ref. [9].

2.6.2 Arsenic self-diffusion

The As_4 pressure dependence of As self-diffusion showed that As vacancies are most likely the responsible native point defect species [63]. This is in inconsistency to the findings reached from other studies involving As atoms and other group V and VI elements that As self-interstitials are the responsible native point defect species. The latter studies comprise for instance: i) P and Sb interdiffusion into GaAs under suitable P and As pressures in order to avoid extended defect development which causes complications [64-66]. ii) Out-diffusion of N from GaAs [67]. iii) As-Sb and As-P interdiffusion in intrinsic GaAs/GaSb_xAs_{1-x} and GaAs/GaP_xAs_{1-x} superlattices taking into account x is small to prevent the large lattice mismatch [64-66]. For this study, the profiles behavior follows the error function. With P and Sb suggested to be interstitial-substitutional elements, such diffusion profiles are explained by an effective diffusivity as $D_S^{eff} = D_i C_i^{eq} / C_s^{eq}$ under thermal equilibrium of native point defect. This is fulfilled by the kick-out mechanism including As self-interstitials or the dissociative mechanism involving As vacancies. It was inferred that the As self-interstitials are the responsible species for this group of experiments, because the diffusion rate was found to increase with increasing the ambient As pressure. For instance, As self-interstitials are the responsible species in S interdiffusion experiments [68] because S profile is characteristic of that owing to kick-out reaction under self-interstitial supersaturation conditions.

2.6.3 Impurity diffusion in GaAs

2.6.3.1 Silicon diffusion

The main *n*-type dopant for GaAs is Si. As mentioned above, it substitutes mainly on the Ga sublattice but exhibits also a high degree of self-compensation at high concentrations owing to its increased solubility on the As sublattice. It was suggested [4, 18] that Si diffusion is governed by negatively charged Ga vacancies and its obvious concentration dependence is the Fermi level effect, which is confirmed by the results of Si diffusion into *n*-type Sn-doped GaAs. The diffusion coefficient of Si donor species Si_{Ga}^+ [4] is found to satisfy:

$$D_{Si}(n) = D_{Si}(n_i) \left(n / n_i \right)^3 \quad (2.51)$$

Eq. 2.51 illustrates that V_{Ga}^{3-} governs the diffusion of Si_{Ga}^+ , where, the quantity $D_{\text{Si}}(n_i)$ is described by:

$$D_{\text{Si}}(n_i) = 5.2 \exp(-4.98 \text{ eV}/k_{\text{B}}T) \text{ cm}^2\text{s}^{-1} \quad (2.52)$$

Si profiles, in Si out-diffusion experiments [69], are found to satisfy Eq. 2.51 but $D_{\text{Si}}(n_i)$ is given by:

$$D_{\text{Si}}(n_i) = 6.67 \exp(-3.91 \text{ eV}/k_{\text{B}}T) \text{ cm}^2\text{s}^{-1} \quad (2.53)$$

The $D_{\text{Si}}(n_i)$ expressed by Eq. 2.53 is several orders of magnitude larger than those determined by Eq. 2.52 at higher temperatures. This reveals the occurrence of an undersaturation and a supersaturation of V_{Ga}^{3-} , respectively under Si in- and out-diffusion conditions [69]. In case of in-diffusion, the starting GaAs material includes V_{Ga}^{3-} and neutral Ga vacancies V_{Ga}^0 to the thermal equilibrium concentrations of those of the intrinsic material. Upon Si in-diffusion, V_{Ga}^{3-} , and also V_{Ga}^0 , become undersaturated compared with the thermal equilibrium V_{Ga}^{3-} concentration values suitable for the n -doping conditions, which can only be improved by inflow of V_{Ga}^{3-} from the interface of the Si source material and the GaAs crystal. It seems that flow of V_{Ga}^{3-} into the GaAs crystal is restricted by the interface region structural and electrical behavior. In case of Si out-diffusion, V_{Ga}^{3-} diffusion is supposed to be more rapidly than that of the Si_{Ga}^+ atoms. In either case, there shall be no considerable spatial variations in the V_{Ga}^0 distribution whereas the spatial distribution of V_{Ga}^{3-} satisfies the local n^3 value.

2.6.3.2 Copper diffusion

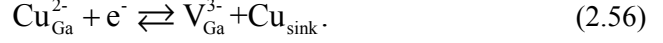
The solubility of Cu in GaAs was measured by Hall and Racette [17]. Copper exhibits a high solubility in extrinsic p -type and n -type GaAs, due to the enhanced solubility of the interstitial and substitutional species, respectively. For intrinsic material the solubility is most likely due to the substitutional Cu. This abnormally high solubility of Cu indicates the presence of a corresponding number of defects which may form complexes with the copper, thereby enhancing its solubility. No distinguished difference was observed between the solubility in the semi-insulating and n -type material [17]. Cu has two levels in the band gap of GaAs and thus a significant influence on the electronic properties. The formation of Cu precipitates on dislocation in GaAs was studied in accord with its diffusion temperature and cooling rate dependence, the results were interpreted considering the Cu influence on the equilibrium of point defects [70]. It was assumed that interstitial copper Cu_i^+ diffuses very fast via kick-out mechanism [40,56] which is expressed as:



where the Cu double acceptor $\text{Cu}_{\text{Ga}}^{2-}$ is identified by cathodoluminescence (CL). Dislocations are sinks for $\text{Cu}_{\text{Ga}}^{2-}$ and in case the Cu cannot reach a sink, precipitates are formed in the bulk. In the model of Tan and Gösele [40,18] the equilibrium concentration of the double positively charged Ga interstitials $C_{\text{GaI}^{2+}}^{\text{eq}}$ is expressed as a function of the carrier concentration p as:

$$C_{\text{GaI}^{2+}}^{\text{eq}} = C_o \left(p / n_i \right)^2. \quad (2.55)$$

C_o is the concentration of interstitials for the intrinsic carrier concentration n_i , $C_o = C_{\text{GaI}^{2+}}^{\text{eq}}(n_i)$. $C_{\text{GaI}^{2+}}^{\text{eq}}$ depends, in addition to the carrier concentration, on the temperature as well as As vapor pressure. The Cu concentration is expected to decrease by out-diffusion, e.g. if the samples are cooled down slowly. Thus, Cu diffuses to possible sinks, such as dislocations, loops or surfaces, and leaves Ga vacancies behind in the sample according to the expression [70]:



The triply charged Ga vacancies were found to react with Si donors, in Si doped GaAs, forming complexes [71,72]. The diffusion of Cu to dislocations during its out-diffusion is related by kick-out mechanism (Eq. 2.54) to a supersaturation of Ga interstitials around dislocations.

2.6.3.3 Sulfur diffusion

Sulfur is incorporated on the As sublattice. The diffusion parameters of As in GaAs were determined by S in-diffusion [73]. It was concluded that S in-diffusion is governed by the kick-out reaction [68]:



Where i_s stands for interstitial sulfur atoms and S_{As} for sulfur atoms on As sublattices. According to Eq. 2.57, S diffusion can allow determining the diffusion parameters of As self-interstitials (I_{As}). In case of the transport capacity of i_s is not higher than that of I_{As} , $D_{i_s} C_{i_s}^{\text{eq}} \leq D_{I_{\text{As}}} C_{I_{\text{As}}}^{\text{eq}}$, the condition for concentration of As $C_{I_{\text{As}}} = C_{I_{\text{As}}}^{\text{eq}}$ is met. The effective diffusion coefficient D_S^{eff} is determined as [73]:

$$D_S^{\text{eq}} = D_{i_s} C_{i_s}^{\text{eq}} / C_S^{\text{eq}} \quad (2.58)$$

The transport properties of S can be estimated under this condition. D_{i_s} is the diffusion coefficient of interstitials S and C_S^{eq} the equilibrium concentration of S_{As} . For the opposite case $D_{i_s} C_{i_s}^{\text{eq}} > D_{I_{\text{As}}} C_{I_{\text{As}}}^{\text{eq}}$, supersaturation of I_{As} is dominant during S in-diffusion. Under nonequilibrium condition the effective diffusion coefficient is given by [65]:

$$D_S^{\text{noneq}} = \frac{D_{I_{\text{As}}} C_{I_{\text{As}}}^{\text{eq}}}{C_S^{\text{eq}}} \left(\frac{C_S^{\text{eq}}}{C_S} \right)^2. \quad (2.59)$$

This expression is based on the postulation of $C_{i_s} > C_{i_s}^{\text{eq}}$. It is clearly shown from Eq. 2.59 that the diffusion coefficient under nonequilibrium conditions depends on C_S , what leads to a non-error-function-like shape of the in-diffusion. On the other hand, the values calculated using Eq. 2.58 corresponds to an almost error-function like diffusion profiles. It is found that the diffusion coefficient of S interstitials is lower than that of the As self-interstitials which leads to S in-diffusion profiles follow the shape given by Eq. 2.59 in the high concentration region (near the surface). A supersaturation of I_{As} is obtained for the nonequilibrium case owing to the high transport capacity of i_s . The effective diffusion coefficient of S is determined as [73]:

$$D_S^{\text{eff}} = 1.9 \times 10^{-3} \exp(2.4 \text{ eV}/k_B T) \text{ cm}^2 \text{ s}^{-1}. \quad (2.60)$$

The nonequilibrium diffusion profile of S was used to determine simultaneously the equilibrium concentration and diffusion coefficient of I_{As} , in particular the shape of the diffusion tail which depends on both factors [73], where the run of the S concentration profile is fitted using an appropriate choice of both $D_{I_{\text{As}}}$ and $C_{I_{\text{As}}}^{\text{eq}}$.

3. Experimental methods

3.1 Physical background of positron annihilation spectroscopy

The positron (e^+) is the first antiparticle to be identified. e^+ is the antiparticle of the electron (e^-). It was predicted by P.A.M. Dirac in 1928 as an interpretation of negative energy solutions of his quantum theory of electrons [74]. The first experimental evidence of the existence of the positron was verified by Anderson during his experiments on cosmic rays with the help of a Wilson cloud-chamber [75]. Since the positron is the antiparticle of the electron, it is unstable in matter. After its injection into the material, the positron is subject to thermalization, diffusion and annihilation. The thermalization process involves the energy loss of the positron via electron and phonon excitation. This process occurs in very short time compared to the positron lifetime. The time of thermalization was estimated to be 3-4 ps [76]. Thereafter, the movement of the positron is expressed as diffusion. The positron diffusion constant, D_+ , of $1.5-3 \text{ cm}^2 \text{ s}^{-1}$ in semiconductors was estimated [77-79]. The average positron diffusion length L_+ is given by [79]:

$$L_+ = \left(D_+ / \lambda_{eff} \right)^{1/2}. \quad (3.1)$$

λ_{eff} is the effective annihilation rate of positrons (the summation of annihilation rates in defect-free crystal bulk and defects). L_+ in defect-free material is in the order of 100...300 nm (GaAs: 100 nm, Si: 245 nm). When positrons are trapped into defects the diffusion length decreases. Then, the measurement allows the determination of the defect density. In the perfect (defect-free) material, the e^+ wave function is a delocalized Bloch wave showing maxima in the interstitial region owing to the Coulomb repulsion of the positron and atom nuclei. In an imperfect lattice crystal, the positron wave function could be localized at open-volume sites, i.e. at the vacancy, vacancy complex or other open-volume defects. That is because of the absence of the repulsing force of the missing atoms. Fig. 3.1 represents the calculated positron wave function in defect-free GaAs (left part) and in a Ga vacancy (V_{Ga}) in GaAs (right part). The calculation was performed using the superimposed-atom method for (110) plane [80].

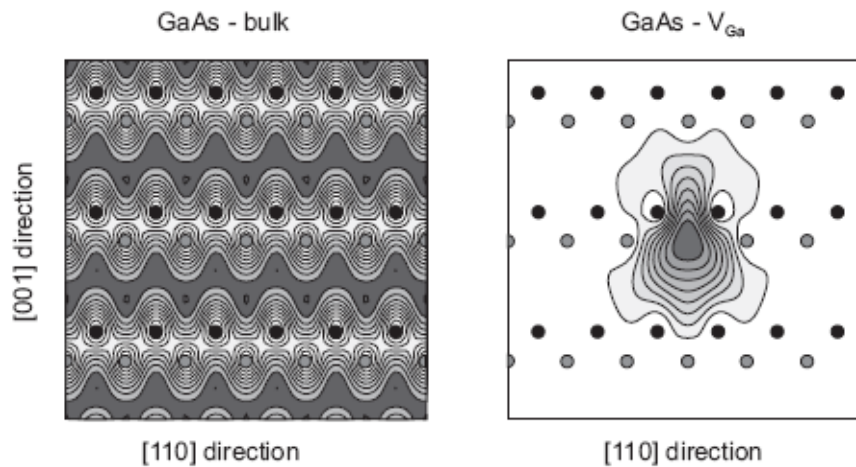
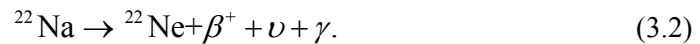


Fig. 3.1: Position probability density of the positrons in defect-free GaAs (on the left) and in a Ga vacancy (V_{Ga}) in GaAs (on the right). The atoms position are given (As - full, Ga - shaded). The calculations were carried out using the superimposed-atom model for (110) plane [76,80]. The darker shading corresponds to higher values of the wave function.

Thus, positron diffused to a vacancy, has the propensity to remain at that site which is energetically propitious. That is the so-called positron trapping process. Finally, positron life comes to an end by annihilation with an electron. When a positron and electron interact through a head-on collision, they annihilate, converting their total mass into energy following Einstein's equation ($E=m_0c^2$). The total amount of energy released when a positron and electron annihilate is 1.022 MeV, corresponding to the combined rest mass energies. Most likely, two γ -rays are released. Each of them has an energy of 511 keV = m_0c^2 (m_0 denotes the electron rest mass; c stands for speed of light in vacuum). The process obeys certain general laws of conservation such as conservation of energy and momentum. The most common positron source for PALS investigation is ^{22}Na . ^{22}Na decays by the emission of positron and electron capture to the first excited state of ^{22}Ne . This excited state de-excites to the ground state of ^{22}Ne by the emission of a 1.274 MeV γ -ray. The decay reaction can be expressed by the equation [79]:



Thus, the birth of the positron is almost simultaneous with the emission of 1.274 MeV γ -ray what is so-called start- γ . The death of the positron is accompanied with releasing the annihilation γ -quanta (stop- γ). The compulsory prerequisite is the presence of only one positron in a sample at a time. This can be verified by using sources having sufficiently low activities. The positron source is placed between two identical samples, what is called sandwich configuration.

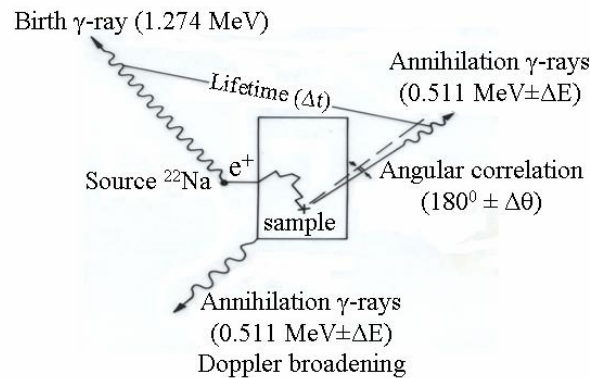


Fig. 3.2: Schematic representation of the different positron techniques. e^+ from a radioactive source, e.g. ^{22}Na , introduced to the sample, thermalizes within a few ps, diffuses, and finally annihilate. The thermalization distance amounts to $100\ \mu\text{m}$ which is much larger than the positron diffusion length L_+ . It is estimated to be about $100\ \text{nm}$.

The different positron techniques are illustrated in Fig. 3.2. They can be classified to two main categories according to positron sensitivity to the electron density (positron lifetime) and to the momentum distribution (Doppler broadening spectroscopy, DBS, and angular correlation of the annihilation radiation, ACAR). Information about the material can be obtained from the analysis of the annihilation radiation.

The positron annihilation rate λ , the inverse of the positron lifetime τ , depends on the overlap of positron density $n_+(\mathbf{r}) = |\psi_+(\mathbf{r})|^2$ and electron density $n_-(\mathbf{r})$ [76]:

$$\lambda = 1/\tau = \pi r_0^2 c \int d\mathbf{r} n_+(\mathbf{r}) n_-(\mathbf{r}) \gamma[n(\mathbf{r})]. \quad (3.3)$$

where r_0 is the classical electron radius and $\gamma[n(\mathbf{r})]$ is the enhancement factor describing the increase in the electron density at the annihilation site due to electrons-positron Coulomb attraction. $\psi_+(\mathbf{r})$ is the positron wave function. Positrons annihilate in the defect-free crystal with lifetime called bulk lifetime, τ_b . In case of semiconductors, τ_b is in the order of 200 ps (228 ps in GaAs).

The electron density in an open-volume defect, i.e. vacancy, is reduced compared to the defect-free crystal lattice. Then, positrons trapped to the vacancy have lifetimes higher than that of the bulk (V_{Ga} in GaAs ~ 260 ps). The longer lifetime of the open-volume defect, what is so-called defect-related lifetime, is a measure of the size of that defect. The strength of this component is directly proportional to the defect concentration.

3.2 Positron annihilation lifetime spectroscopy

The positron lifetime is measured as the time difference between the birth γ -quanta (1.274 MeV) and one of the annihilation γ -gammas (0.511 MeV). The sample, i.e. “sandwich”, is located between two γ -ray detectors. One of them used to detect the start γ -ray and the other detector for stop γ -quantum. Each detector consists of BaF₂ or plastic scintillator coupled with a photomultiplier tube. The output signals from the detectors are processed by constant fraction discriminators. The stop and start signals are discriminated by their energies (1.274 and 0.511 MeV). The output signals start and stop the time-to-amplitude converter (TAC). Its output signal amplitude is proportional to the time difference between the start and stop γ -quanta and, thus, represents the positron lifetime of a single event. A multi-channel analyzer (MCA) is used to save the detected events. This experimental arrangement is defined as fast-fast coincidence setup. The name of the setup is originated from the fact that the energy selection in addition to the time measurement is carried out in the fast channel. At the beginning of positron lifetime measurements, fast differential discriminators were not available. Thus, a slow channel was used for energy selection. This arrangement is called fast-slow setup. More experimental details can be found in [79]. A schematic diagram of the positron lifetime measurement is shown in Fig. 3.3. The resolution of the spectrometer and the real lifetime spectrum are convoluted within the experimentally obtained spectrum.

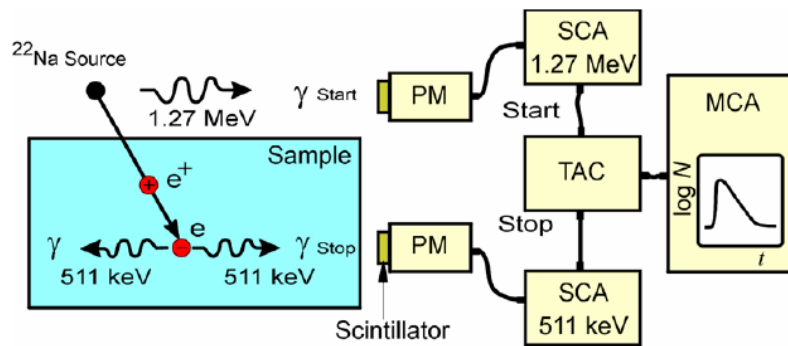


Fig. 3.3: A schematic diagram of fast-fast coincidence spectrometer. The lifetime is measured as the time difference between the appearance of the start and stop γ -rays. (PM: photomultiplier; SCA: single channel analyzer; TAC: time-to-amplitude converter; MCA: multi channel analyzer). (From Ref. [79])

3.2.1 Lifetime spectra analysis

The time dependent positron decay spectrum $D(t)$ in the sample is expressed as [79]:

$$D(t) = \sum_{i=1}^{k+1} I_i \exp(-t / \tau_i). \quad (3.4)$$

Where k denotes the number of defect types contributing to the positron trapping. A number of components, $k+1$, are involved in the spectrum with individual lifetimes τ_i and their corresponding

intensities I_i with $\sum I_i = 1$. In case of a defect-free sample, i.e. no positron traps, $k=0$ and the equation is diminished to $D(t) = \exp(-t/\tau_b)$.

The real positron lifetime spectrum is given by the probability $N(t)$ that the positron annihilates at time t [79,81,82] as:

$$N(t) = \sum_{i=1}^{k+1} (I_i / \tau_i) \exp(-t / \tau_i). \quad (3.5)$$

It is described as the time derivative of the positron decay spectrum $D(t)$. The decomposition of the lifetime spectra is performed using standard computer programs which are based on Gauss-Newton non-linear fitting routines. Examples of these routines are LIFSPECFIT [83] by Puska 1978 and PATFIT [84] by Kirkegaard. These programs can be classified into two categories. Up to four lifetime components can be deconvoluted in one of them such as POSITRONFIT program [84]. The problems encountered through the treatment of spectra using this kind of programs are the source correction and determination of number of component. The number of components should be given as an input parameter. The other kind of programs, e.g. the MELT program [85], provides the distribution of lifetimes and the number of components. The source correction should be performed precisely. The LT [86,87] is one of the widely used programs for the analysis of the lifetime spectra. Two measured lifetime spectra are shown in Fig. 3.4 as an example. One of them is measured in GaAs:Zn and shows only one component corresponding to the defect-free positron lifetime in GaAs:Zn (228 ps). The GaAs:Si sample contains native defects. As a result, the decomposition of the spectrum shows two components results in increasing the average lifetime to 256 ps.

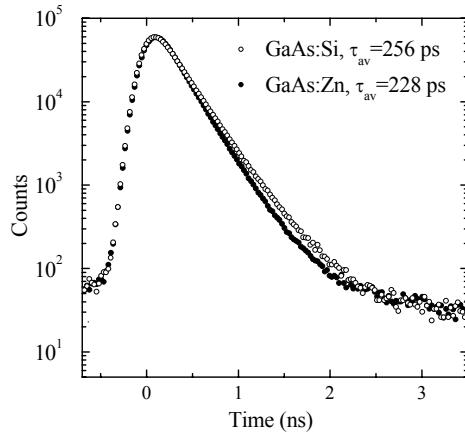


Fig. 3.4: Positron lifetime spectra measured in GaAs:Zn and GaAs:Si. The presence of native open-volume point defects in GaAs:Si increases the average lifetime compared to that of GaAs:Zn.

3.2.2 Trapping of positrons in defects

Positrons after being thermalized may be trapped into lattice defects. This allows measuring the involved defects by the different positron methods.

The trapping rate was obtained with the help of Fermi's golden rule formula [79]:

$$\kappa = \frac{2\pi}{\hbar} \sum_{i,f} P_i M_{if}^2 \delta(E_i - E_f), \quad (3.6)$$

where P_i is the probability that the initial state i is occupied with a positron and P_f is the probability that the final state f is allowed. M_{if} is the matrix element of the interaction potential.

The matrix element depends on the energy transfer during transition of positron from the initial state with energy E_i to the final state which has the energy E_f . The delocalized Bloch state of the

positron represents the initial state. The final state corresponds to the positron trapped in the defect. The energy conservation condition is met by taking the summation in Eq. 3.6 over all possible states. A Maxwell-Boltzmann form was assumed for the initial positron distribution. This leads to a temperature dependence trapping coefficient expressed as [76]:

$$\nu(T) = \sqrt{\frac{2}{\pi}} \left(\frac{m^*}{k_B T} \right)^{3/2} \int_0^\infty dE \kappa(E) e^{-E/k_B T} \sqrt{E}. \quad (3.7)$$

m^* is the positron effective mass.

Mostly, the trapping process is governed either by diffusion of positron to the defect or by transition of positron to the deep bound state. They are expressed diffusion-limited and transition-limited, respectively. As shown in the right part of Fig 3.5, in case of the diffusion-limited trapping, their energies are dissipated easily. That is because the defects have an extended potential well but the binding energy of positron is relatively small ≈ 0.1 eV. Examples are coherent precipitates in alloys or voids at room temperature. If the defects are in homogeneous distribution and spherical with radius r_d ($r_d \ll L_+$) the trapping rate is given by [81]:

$$\kappa_d = 4\pi r_d D_+ C_d. \quad (3.8)$$

C_d denotes the defect concentration. In the transition-limited trapping, positrons diffuse very fast to the defects and then they are subject to the transition to the localized state which is the deep bound state. Positrons lose their energy during the transition. This is ascribed to the deep and small potential well of the defects as represented in the left part of Fig. 3.5. The best example is vacancies in semiconductors or metals. In that case, the trapping rate is expressed by [81]:

$$\kappa_d = \mu C_d. \quad (3.9)$$

The proportionality coefficient μ is called trapping coefficient (specific trapping rate as reported in some literature). It should be determined for every defect type by an independent method, e.g. Hall measurement.

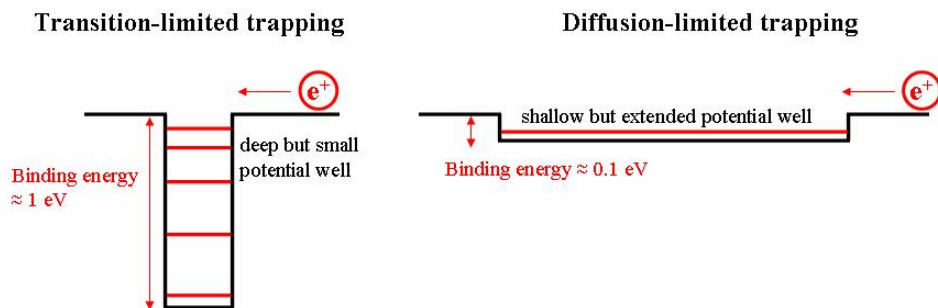


Fig 3.5: Schematic representation of the transition-limited trapping (left part) and diffusion-limited trapping (right part).

When positrons are trapped in vacancies, the trapping process is based on the attractive potential for positrons which originates from the missing repulsive force of the lacking nucleus. The trapping model was derived for the description of the positron trapping in defects provided that positrons are trapped after the thermalization as well as the defects are homogeneously distributed in the sample. It is taken into account that there is no interaction between the defects in the sample and also the positron wave function is localized at the lattice defect site. Information on the dominant trapping centers and their concentrations can be obtained if the analysis of the spectra with the trapping model is feasible. The data analysis based on the trapping model aims to the determination of the

trapping rate and hence the defect concentration. One open-volume defect type as the simplest case of the trapping model is represented in the next subsection.

3.2.2.1 Positron trapping into one-defect type

The trapping model for a single open-volume defect type such as a vacancy is schematically represented in Fig. 3.6.

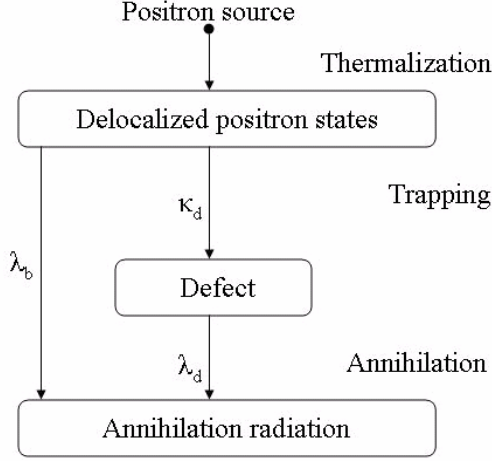


Fig 3.6: Schematic presentation of the trapping model with only a single defect type. A thermalized positron either annihilates from the delocalized state with annihilation rate λ_b or is trapped into the defect with the trapping rate κ_d and then annihilate with the annihilation rate λ_d .

This is used to illustrate the trapping model of positrons into a single defect type. The thermalized positrons may annihilate from the delocalized state in the defect-free bulk with the annihilation rate λ_b . A fraction of positrons diffusing through the sample may be trapped in the vacancy with the trapping rate κ_d as long as the vacancy concentration in the sample is sufficiently high. The thermal escape from the deep state of the vacancy is not taken into account in this model. Due to the reduction of the electron density in the defect site, positrons trapped to them annihilate with a lifetime τ_d which is higher than τ_b . The rate equation can be expressed as [79]:

$$\begin{aligned} \frac{dn_b(t)}{dt} &= -(\lambda_b + \kappa_d)n_b(t). \\ \frac{dn_d(t)}{dt} &= -\lambda_d n_d(t) + \kappa_d n_b(t). \end{aligned} \quad (3.10)$$

n_b and n_d are the number of positrons in the bulk and defect at time t . λ_b and λ_d denote the annihilation rates in the bulk and defect. κ_d is the positron trapping rate of the defect. The boundary conditions are $n_b(0) = N_0$, where N_0 is the total number of positrons at $t=0$, and $n_d(0) = 0$. This verifies the precondition that trapping of positrons occurs after reaching thermal energies. The solution of the Eq. 3.10 gives the decay spectrum of positrons,

$$D(t) = I_1 \exp(-t/\tau_1) + I_2 \exp(-t/\tau_2). \quad (3.11)$$

Eq. 3.11 is the same as Eq. 3.4 where number of defects $k=1$.

The two-component decomposition of the lifetime spectrum is possible; τ_1 and τ_2 , where:

$$\tau_1 = 1/\lambda_1 = \frac{1}{\lambda_b + \kappa_d}, \quad \tau_2 = 1/\lambda_2 = 1/\lambda_d. \quad (3.12)$$

Their relative intensities are:

$$I_1 = 1 - I_2, \quad I_2 = \frac{\kappa_d}{\lambda_b - \lambda_d + \kappa_d}. \quad (3.13)$$

Where λ_b , the inverse of τ_b , is the annihilation rate in the perfect lattice.

$\lambda_d = 1/\tau_d = 1/\tau_2$ is the positron annihilation rate from the localized (trapped) state. κ_d is the positron trapping rate to the defect. Eq. 3.3 shows that τ_d carries information about the electron density at the trapping and annihilation site. τ_d represents a characteristic value of the size of the open-volume of the defect. It is the reciprocal of the positron annihilation rate in the defect and it is assumed to be defect concentration independent.

The ratio τ_d/τ_b in case of monovacancies in semiconductors is ~ 1.2 [79].

The absolute value of the time derivative of Eq. 3.11 presents the lifetime as [79]:

$$N(t) = \left| \frac{dD(t)}{dt} \right| = \frac{I_1}{\tau_1} \exp\left(-\frac{t}{\tau_1}\right) + \frac{I_2}{\tau_2} \exp\left(-\frac{t}{\tau_2}\right). \quad (3.14)$$

The experimental lifetime spectrum includes in addition to Eq. 3.14 the resolution of the lifetime spectrometer as well as a constant background contribution. On the other side, the trapping rate is proportional to the defect concentration C_d , as described in Eq. 3.9. It can be obtained from the lifetime spectrum decomposition as:

$$\kappa_d = \mu C_d = I_2 \left(\frac{1}{\tau_1} - \frac{1}{\tau_2} \right) = \frac{I_2}{I_1} \left(\frac{1}{\tau_b} - \frac{1}{\tau_d} \right). \quad (3.15)$$

More frequently, the average lifetime τ_{av} is used widely, because it can be experimentally determined with high accuracy. It is given by:

$$\tau_{av} = \sum_{i=1}^{k+1} I_i \tau_i. \quad (3.16)$$

Consequently, it is quite insensitive to the fitting procedure applied.

Very often, the trapping rate may be determined from the average positron lifetime, in particular when both τ_b and τ_d are known. It is given by [79]:

$$\kappa_d = \frac{1}{\tau_b} \frac{\tau_{av} - \tau_b}{\tau_d - \tau_{av}} = \frac{\eta}{\tau_b(1-\eta)}. \quad (3.17)$$

η stands for the annihilation fraction (more often also called fraction of trapped positrons) determined by:

$$\eta = \int_0^{\infty} n_d(t) dt = \frac{\kappa_d}{\lambda_b + \kappa_d}. \quad (3.18)$$

3.2.3 Shallow positron traps

Shallow positron traps in semiconductors were observed clearly by Saarinen et al. [88] using a slow positron beam on undoped GaAs. The expression shallow trap does not indicate a shallow energetic position of the defect in the band gap but refers to the small value of binding energy to a positron. An increase in the positron diffusion length was observed in the temperature range 100-200 K, and this was accompanied with changes in the structure of the lifetime spectra at the same temperature range. This was ascribed to thermal positron detrapping from the shallow positron traps [88]. It was concluded that negatively charged non-open volume defects, such as ionized acceptors (e.g. C_{As}^-)

or negative antisite defects (Ga_{As}^-), act as shallow positron traps [88,89]. Positrons trapped at shallow traps have annihilation parameters, such as positron lifetime or the Doppler S parameter, very close to those of the bulk. That is because the position probability density of the positron is expanded to the bulk nearby the shallow traps. It is strongly reduced at the site of the nucleus. Considering that these traps are not of vacancy type and do not involve open volume, this results in difficulties for the detailed microscopic identification of the shallow traps. Negative charged ions can induce the observed shallow positron state. The appearance of shallow positron traps in semiconductors is not only constrained to negatively charged non-open volume defects. Very small open volume defects related to a small positron binding energy may also act as shallow traps. The A center in silicon and undisturbed dislocation are also examples for such defects. For negatively charged non-open volume defects, e.g. negative ions, positrons are captured in shallow Rydberg states caused by the long-range Coulomb potential. The attractive potential of the negative ions is superimposed on the strong repulsive potential of the nucleus. The small binding energy of the positron to the Rydberg state gives rise to an obvious temperature dependence of the positron trapping via the thermally induced detrapping. This positron detrapping is explained by the detrapping rate δ_r as [90]:

$$\delta_{\text{st}} = \frac{\kappa_{\text{st}}}{C_{\text{st}}} \left(\frac{m^* k_{\text{B}} T}{2\pi \hbar^2} \right)^{3/2} e^{-E_{\text{st}}/k_{\text{B}} T}. \quad (3.19)$$

κ_{st} is the positron trapping rate into shallow traps, C_{st} is the shallow traps concentration, and E_{st} denotes the positron binding energy to them.

The detection of defects requires that they have characteristic annihilation parameters differing from those of the bulk values. Thereafter, more likely shallow traps cannot be directly identified. The temperature dependence of positron trapping to shallow traps could be used for that reason. Positron shallow traps could be measured as a competing trapping center to an open-volume defect showing annihilation parameters noticeably different from the bulk. A more direct way for the detection of shallow traps is the measuring of the diffusion length L_+ using back-diffusion experiments. In such a method, the positron diffusion length is affected by the existence of shallow traps. The decrease in L_+ at low temperatures may point to the existence of shallow traps. Although the average lifetime and S parameter in the bulk did not show the existence of any open-volume defect, the decrease of L_+ in the low temperature region was explained by the presence of shallow traps [88]. The effect of competitive trapping into negative or neutral vacancies and in shallow positron traps on the average lifetime was considered theoretically [79] as shown in Fig. 3.7. In which shallow traps were considered as negatively charged non-open volume defects. Lifetimes of $\tau_v=270$ ps and $\tau_{\text{st}}=\tau_b=218$ ps were taken into consideration. Typical values of the trapping coefficient were considered. The trapping rate was chosen to be low enough to evade occurrence of the trapping saturation in one of the defects in carrying out the computation. A positron binding energy of 30-40 meV to the shallow traps was considered. For a neutral vacancy, a temperature independent average positron lifetime is obtained. That is according to the occurrence of transition-limited trapping process to the only defect. Such temperature independence of τ_{av} in neutral vacancy has not been observed in semiconductors so far but it is often obtained in metals. In case of considering a neutral vacancy as well as a shallow trap, a distinct decrease of τ_{av} at low temperature is observed. Consideration of competitive trapping into a negative vacancy and a shallow trap leads to a more complicated temperature dependence of the average positron lifetime.

Here, τ_{av} increases with decreasing the temperature up to 100 K then decreases even lower temperatures. Such temperature behavior of τ_{av} is observed experimentally by Polity et al. [91].

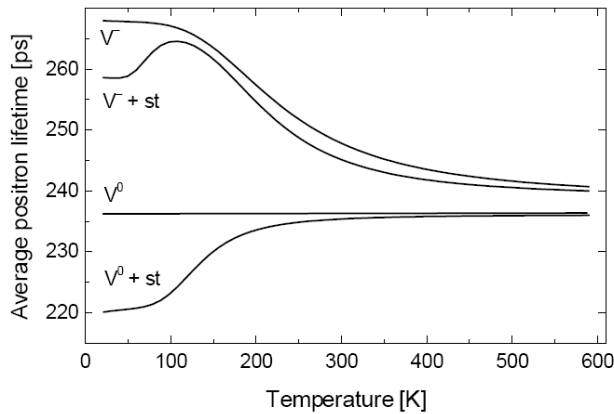


Fig. 3.7: Temperature dependence of the average positron lifetime for neutral and negative vacancies (V° and V^{-}) and shallow traps [79]. The effect of shallow positron traps, st , as competing trapping centers to both types of vacancies is shown.

The positron binding energy to shallow traps is estimated to be 43 meV [88]. Native point defects, e.g. Ga_{As} , in GaAs act as shallow traps. In Cu diffused GaAs:Te, Cu acceptors act as shallow traps and the positron binding energy to them is determined to be 79 meV [92]. The decrease of the average positron lifetime at low temperatures was the direct evidence of the existence of the shallow traps [92,93]. Thus, the possibility of positron localization around a negative point charge at low temperatures gives a conceivable model and interpretation for the experimental results.

3.2.4 Dependence of positron trapping on the temperature in semiconductors

The trapping coefficient in semiconductor, in contrast to metals, reveals some temperature dependence. This may differ for different semiconductor materials or different defect types. It is clear that the temperature behavior of the trapping coefficient is specific for a certain defect type and provides significant information about the defect properties. The ability of extraction this information requires a full understanding of the positron trapping process and its temperature dependence.

3.2.4.1 Theoretical considerations

Puska et al. [76,94] described theoretically the positron trapping into vacancies and its temperature dependence. They presumed a model potential for positron capture in differently charged and neutral vacancies to calculate the temperature dependence of the trapping coefficient as schematically represented in Fig. 3.8. A simple square-well potential was assumed to explain the positron capture to the neutral vacancy. The depth and width of the square-well were selected so that the s-like ground state had a binding energy and spatial extension similar to those obtained by first principles calculations for electron and positron states in semiconductors. This results in a temperature-independent trapping coefficient as shown in Fig 3.9. The charge of the vacancy is considered by superimposing the square-well potential with the long-range Coulomb potential ($V_{\pm}(r)=1/\epsilon_0 r$), where ϵ_0 is the dielectric constant. This gives rise to an additional attraction or repulsion in case of a negative or positive charge. The Coulomb tail cut-off was suggested to explain the delocalization of the charge. The Coulomb tail should be cut off when approaching the vacancy from infinity to imitate the weak localization of the “extra” electron charge. Thus, close to the vacancy the potential was shifted by the amount of $Q \times 0.1$ eV. Q denotes the charge state of the vacancy and 0.1 is the value of the Coulomb potential at the cut-off. This constant potential shift

does not change the positron localization in the bound state and the energy value is simply changed by the same amount as the potential. However, the potential shift and the Coulomb tail can have a considerable effect on the delocalized positron wave functions at thermal energies.

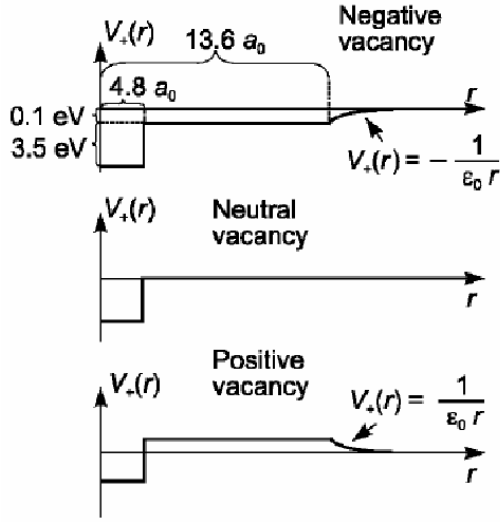


Fig. 3.8: A schematic representation of the positron potential V_+ for negative, neutral, and positive vacancies in Si according to Puska et al. [94]. a_0 is the Bohr radius. The Coulomb tail is cut off at a distance $r=13.6 a_0$ as a result of the charge delocalization. The value $4.8 a_0$ is assumed as a radius of the neutral vacancy.

A series of Rydberg states in addition to the deep bound state is introduced as a result of the assumption of the long-range Coulomb potential. In case of the positive vacancy, positron trapping is forbidden at low temperature. That is because the repulsion is extremely strong. The theoretical calculation expects that thermal excitation over the potential barrier could be induced at higher temperatures. What increases the trapping coefficient of the positive vacancies to be one order of magnitude lower than that for neutral vacancies at 300K as shown in Fig. 3.9. However, the positively charged vacancies have never been observed experimentally by positron annihilation spectroscopy. A probable reason is that the positron does not have enough time to tunnel through the repulsive Coulomb barrier. For a negatively charged vacancy, as shown in Fig 3.9, a distinct increase of the trapping coefficient in the low temperature region is expected. That is due to the existence of Rydberg states which are induced by the long-range Coulomb potential. These extended Rydberg states enhance the positron trapping process. In contrast to the neutral vacancy, positrons are trapped first from the delocalized state to these extended states, as a precursor state, with a high transition rate. Finally, they are trapped to the deep bound state of the square-well potential. This two-stage process leads to more efficient trapping. Thereafter, the trapping coefficient is higher than that of the neutral vacancy. The trapping coefficient of the negative vacancy is about one order of magnitude larger than that of the neutral vacancy. At room temperature (RT), it is determined to be $2\text{-}5 \times 10^{14}$ and $2\text{-}4 \times 10^{15} \text{ s}^{-1}$ for the neutral and negatively charged vacancy, respectively. These values are in good agreement with the trapping coefficients found experimentally for the negative gallium vacancy in GaAs [95,96]. At low temperatures, the trapping coefficient increases and is governed by a $T^{-1/2}$ power law. This divergence of temperature dependence is a direct result of the normalization of the initial positron wave function. The square of the amplitude of the Coulomb wave at the center of the vacancy, i.e. at the origin, is at maximum and described as [97]:

$$|u_{i,p}(0)|^2 \propto \frac{\alpha}{e^{2\pi\alpha} - 1}. \quad (3.20)$$

Where α is defined as;

$$\alpha = \frac{m^* Q}{\epsilon P}. \quad (3.21)$$

ϵ is the dielectric constant and P is the positron wave-vector. For a negative charge state Q , the square of the matrix element Eq. (3.6) and, thus, the positron trapping coefficient is proportional to the reciprocal of the square root of the positron energy. The integral over the energy in Eq. 3.7 becomes then proportional to the temperature, what leads to the $T^{-1/2}$ power law temperature dependence of the trapping coefficient. For very small values of α , the amplitude in Eq. 3.20 approaches a constant value and the wave function becomes a plane wave. Thus, the trapping coefficient of neutral vacancies does not deviate at low temperatures from its value at RT. However, this was never observed experimentally in a semiconductor. The positron binding energy to the Rydberg states amounts to ≈ 100 meV. The trapping coefficient for negative vacancies decreases with increasing the temperature owing to the thermal detrapping of positrons from Rydberg states. That is because of the small binding energy.

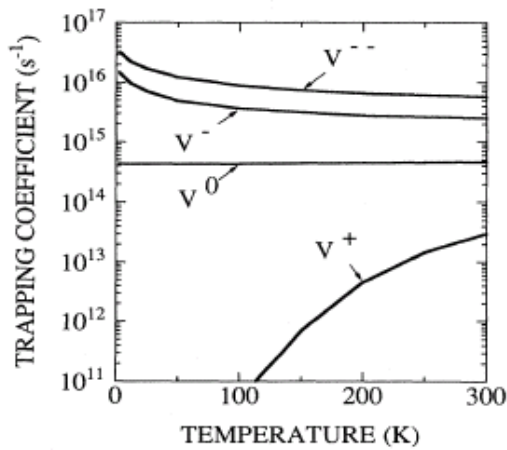


Fig. 3.9: Temperature dependence of the positron trapping coefficient of positively and negatively charged and neutral monovacancies in Si, according to Puska et al. [76].

Therefore, the trapping of the delocalized positron could occur in one of two ways: either direct trapping to the deep bound state of the vacancy or two-step trapping. In the later, the positron is trapped first into a weakly localized Rydberg state from which it then makes a transition into a deeper localized state in the vacancy. The positron has to lose its energy during the trapping process.

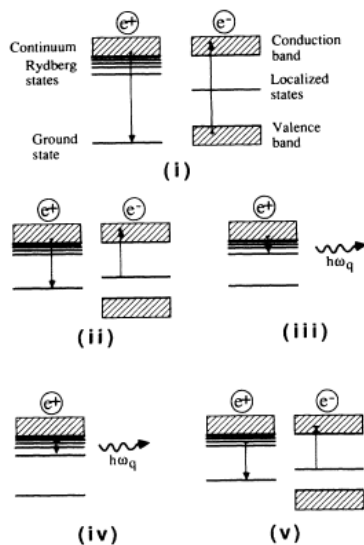


Fig. 3.10: Schematic representation of the mechanisms of positron energy-loss mechanisms: (i) interband electron-hole excitations; (ii) exciting of the electron from a defect level to conduction band; (iii) trapping into Rydberg states; (iv) transition between Rydberg states, and (v) between Rydberg and ground states [94].

Five mechanisms of the energy-loss were suggested, in which the energy of a delocalized positron is released as illustrated in Fig. 3.10.

In case of the direct trapping, two processes are possible:

- (i) electron-hole excitation from the valence to the conduction band;
- (ii) electron-hole excitation from the localized defect-level to the conduction band;

In case of two-step trapping there are three processes:

- (iii) phonon-assisted capture of a delocalized positron into a Rydberg state;
- (iv) phonon-assisted transitions between Rydberg states;
- (v) transition from a Rydberg state to the ground state.

The first three transition mechanisms only concern the capture of a delocalized positron and thus reveal the temperature dependence of the trapping coefficient. The most sensitive process to the temperature is the positron trapping into a Rydberg state of the shallow Coulomb potential of a negative vacancy. Because the binding energy of the positron to the extended defect is weak, there is a certain probability that the positron escapes from the trap back to a delocalized state what is the so-called detrapping process. When the delocalized and the trapped states are in thermal equilibrium, the ratio of the detrapping to the trapping rates at a given temperature is given as [76]:

$$\frac{\delta_r}{\kappa_r} = \frac{1}{C_r} \left(\frac{m^* k_B T}{2\pi \hbar^2} \right)^{3/2} e^{-E_R/k_B T}. \quad (3.22)$$

Where δ_r is the detrapping rate from Rydberg states and κ_r is the trapping rate to Rydberg states.

E_R is the positron binding energy to the Rydberg states, and C_r is the concentration of defects.

A more qualitatively description of the positron trapping in vacancies was given by using a simple two-state model. In which, the Rydberg states series is replaced by a single level as schematically depicted in Fig. 3.11.

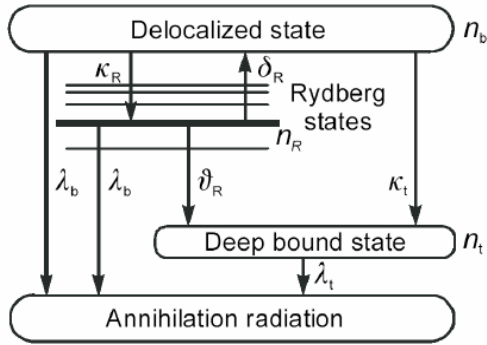


Fig. 3.11: A scheme of two-stage positron into negatively charged vacancy. The Rydberg states (thin lines) are replaced by a single level [79].

Positrons get trapped into the Rydberg state with the trapping rate κ_R or directly to the vacancy at deep bound state with trapping rate κ_t . Positrons trapped in the Rydberg state either pass over to the deep ground state of the vacancy with transition rate ν_R or may escape thermally stimulated with detrapping rate δ_R . λ_b and λ_t denote the annihilation rate in the defect-free bulk and vacancy, respectively. n_b stands for the number of positrons in the delocalized state (bulk). n_R and n_t refer to the number of trapped positrons into Rydberg and deep bound states, respectively. Positrons annihilating from the Rydberg state are supposed to have the same annihilation rate of the bulk, λ_b . That is because positrons in Rydberg states are presumed to sense the bulk electron

density. Positrons may re-escape from the Rydberg states with detrapping rate δ_R expressed by Manninen and Nieminen [90] as:

$$\delta_R = \frac{\kappa_R}{C_V} \left(\frac{m^* k_B T}{2\pi \hbar^2} \right)^{3/2} e^{-E_R/k_B T}. \quad (3.23)$$

E_R is the positron binding energy to the Rydberg state and C_V is the vacancy density. The resulting trapping rate of the two-stage trapping process, in which positrons are first trapped into Rydberg states then to the deep state of the vacancy, is described by [94]:

$$\kappa = \frac{\kappa_R \nu_R}{\nu_R + \delta_R}. \quad (3.24)$$

3.2.4.2 Positron trapping model for experimental data fitting

A description of the positron trapping model for fitting the temperature dependence average lifetime τ_{av} (T) curves obtained experimentally is considered in this subsection. The choice of τ_{av} instead of the decomposition results for fitting the data is attributed to the fact that it represents the center of mass of the spectrum and, thus, it is stable and more reliable in the procedure of spectra analysis which does not depend much on the details of the decomposition. The trapping of positrons to the Rydberg states induced by the long-range coulomb potential is taken into consideration.

3.2.4.2.1 Trapping of positron by negatively charged vacancy

The trapping rate of positron trapping at a single defect is given by Eq. 3.17. The average positron lifetime can be obtained from the transformation of Eq. 3.17 as:

$$\tau_{av} = \tau_b \frac{1 + \kappa_d \tau_d}{1 + \kappa_d \tau_b}. \quad (3.25)$$

As shown in the two-step trapping model (Fig. 3.12), the total trapping rate κ_d is obtained by the sum of two trapping mechanisms: direct and indirect two-step trapping. In the two-step trapping model, positrons are captured into the Rydberg states of the long-range Coulomb potential with trapping rate κ_R . Positrons trapped to Rydberg states may pass over to the deep bound state of the vacancy with transition rate η_R or thermally re-escape back to the delocalized state with detrapping rate δ_R or annihilate with annihilation rate $\lambda_{st} \sim \lambda_b$. The direct trapping to the ground state of the vacancy occurs at a rate κ_V . Where κ_V is related to the defect concentration through the relation $\kappa_V = \mu_V C_V$ and μ_V is in the order of $1.5-3 \times 10^{16} \text{ cm}^{-3} \text{ s}^{-1}$ [95]. The ratio $\kappa_R / \kappa_V \geq 5$ is considered, what reflects the larger overlapping of the localized wave function with the extended Coulomb potential. A single effective state is considered to approximate the series of Rydberg states to which positrons have a binding energy E_R . It is in the order of $70 \pm 30 \text{ meV}$. The ratio between the rates of positron trapping into Rydberg states to the positron transition is assumed to be $\mu_R / \eta_R \approx 10^4 - 10^5$ [95].

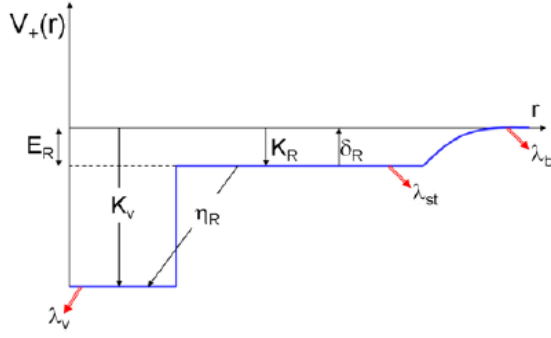


Fig. 3.12: Model of positron trapping into a negative vacancy. It involves positron capture into Rydberg states of the attractive Coulomb potential at a rate κ_R and positron detrapping from these states at rate δ_R . (From Ref. [39])

The trapping rate of two-step trapping is expressed as [94]:

$$\kappa_{\text{indirect}} = \frac{\kappa_R \eta_R}{\delta_R + \eta_R}. \quad (3.26)$$

Thereafter, the total trapping rate can be described as [95]:

$$\kappa_d = \kappa_{\text{direct}} + \kappa_{\text{indirect}} = \kappa_v + \frac{\kappa_R}{1 + \frac{\mu_R}{N\eta_R} \left(\frac{m^* k_B T}{2\pi\hbar^2} \right)^{3/2} \exp\left(-\frac{E_R}{k_B T}\right)}. \quad (3.27)$$

where N is the atomic density in the defect-free crystal and μ_R is the trapping coefficient of the positron to the Rydberg state, related to κ_R through $\kappa_R = \mu_R C/N$. Supposing that both κ_R and κ_v follow the theoretically predicted temperature dependence of $T^{-1/2}$ power law. Then, κ_d can be expressed as [95]:

$$\kappa_d = \kappa_v (20K) \left(\frac{T}{20K} \right)^{-1/2} + \frac{\kappa_R (20K) \left(\frac{T}{20K} \right)^{-1/2}}{1 + \frac{\mu_R}{N\eta_R} \left(\frac{T}{20K} \right)^{-1/2} \left(\frac{m^* k_B T}{2\pi\hbar^2} \right)^{3/2} \exp\left(-\frac{E_R}{k_B T}\right)}. \quad (3.28)$$

The temperature dependence of the average lifetime $\tau_{\text{av}}(T)$ can be obtained from Eq. 3.25 by substituting κ_d (Eq. 3.28). $\tau_{\text{av}}(T)$ depends on four independent parameters mentioned above; κ_v , κ_R , E_R and μ_R/η_R .

3.2.4.2.2 Trapping of positron into two defects: negative vacancies and shallow traps

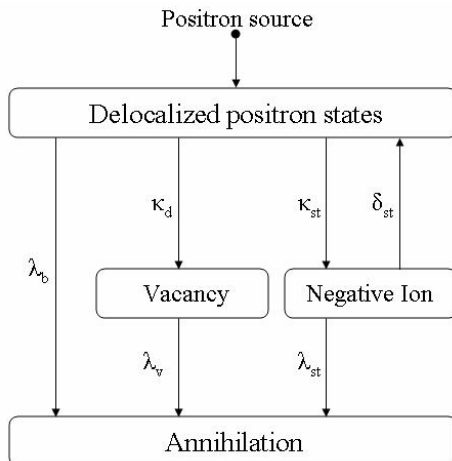


Fig 3.13: Schematic presentation of the trapping model for two types of defects (neutral vacancies and shallow traps). A thermalized positron may be trapped to the vacancy with trapping rate κ_d or to the shallow trap with trapping rate κ_{st} . Positrons trapped to the shallow traps either annihilate with annihilation rate $\lambda_{st} \approx \lambda_b$ or escape back to the delocalized state with detrapping rate δ_{st} .

When shallow positron traps are present in the crystal as well as vacancies, the one-defect trapping model described above is only appropriate at temperatures higher than 300 K. In the low temperature region, positrons are trapped into both, vacancy and shallow trap defects and thus the two-defect trapping model must be used. However, in that case the detrapping of positrons from the shallow traps has to be taken into account, as shown in Fig 3.13. τ_{av} is expressed as [95]:

$$\tau_{av} = \tau_d \frac{(\lambda_d + \kappa_d) \left[\frac{\lambda_{st}}{\kappa_{st}} + \frac{\delta_{st}}{\kappa_{st}} \right] + \lambda_d}{(\lambda_b + \kappa_d) \left[\frac{\lambda_{st}}{\kappa_{st}} + \frac{\delta_{st}}{\kappa_{st}} \right] + \lambda_{st}}. \quad (3.29)$$

$\lambda_{st} = 1/\tau_{st}$ and $\lambda_d = 1/\tau_d$ are the annihilation rates in the shallow trap and the vacancy defects, respectively. The ratio of detrapping and trapping rates δ_{st}/κ_{st} is determined by Eq. 3.19. It is suggested that κ_{st} varies like $T^{-1/2}$. At low temperatures ($T < 100$ K), the detrapping from shallow traps may be approximately neglected. Thus, $\kappa_{st}(20$ K) is determined using the simple two-defect type trapping model as [95]:

$$\kappa_{st}(20 \text{ K}) = \lambda_b \frac{\tau_{av}(20 \text{ K}) - \tau_b}{\tau_{st} - \tau_{av}(20 \text{ K})} - \frac{\tau_{av}(20 \text{ K}) - \tau_d}{\tau_{av}(20 \text{ K}) - \tau_{st}} \kappa_d(20 \text{ K}). \quad (3.30)$$

It was assumed that $\tau_{st} = \tau_b$. This formula is useful, if κ_d at high temperatures, where no effect of the shallow traps is to be expected, can be determined using the one-defect trapping model. Then, $\kappa_d(20$ K) could be estimated considering the trapping rate temperature dependence of $T^{-1/2}$ [95].

3.3 Doppler broadening spectroscopy

3.3.1 Principle

The momentum conservation during the annihilation results in the transfer of the momentum of the e^-e^+ pair to the annihilation photons. Thus, the annihilation radiation carries information on the electron momentum distribution at the annihilation site. That is useful for studying the electron structure of the material to investigate the defects. Two techniques are possible to study the momentum distribution: Doppler broadening spectroscopy and angular correlation of annihilation radiation. The annihilation process of electron and positron is followed by the emission of two γ -rays. In the center-of-mass frame, the total momentum of the e^-e^+ pair is zero. Due to the conservation of energy and momentum before and after the annihilation process, the two quanta are released in opposite directions; each one has an energy equal to 511 keV. In the laboratory frame, the e^-e^+ pair carries a total moment \mathbf{p} , which is transferred to the photon pair, as illustrated in the momentum diagram in Fig. 3.14.

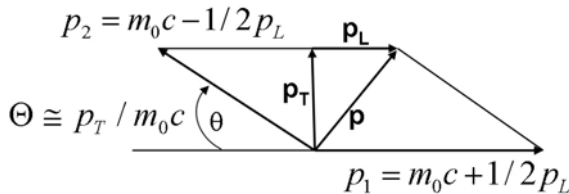


Fig. 3.14: The vector diagram of the momentum conservation during the 2γ -annihilation process. \mathbf{p} stands for the momentum of e^-e^+ pair. p_L and p_T denote the longitudinal and transverse components, respectively.

The Doppler shift (ΔE) of the annihilation line, 511 keV, is caused by the longitudinal momentum p_L . ΔE is expressed as [79]:

$$\Delta E = \frac{1}{2} p_L c. \quad (3.31)$$

Since the positron annihilate only after being thermalized, then its momentum, as thermalized positron, is very small compared to that of the electrons in the crystal lattice. What allows us to consider that p_L corresponds to the momentum of the annihilating electrons. This provides the possibility of the investigation of the electron momentum distribution of the investigated sample. Because of the equal-probability for both momentum \mathbf{p} directions, to and from the detector, both positive and negative ΔE are measured, giving rise to the Doppler broadening of the annihilation radiation gamma line of 511 keV. Thus, the broadening of the energy line is caused by the individual Doppler shifts in both direction $\pm z$. The Doppler spectrum is given by accumulation of numerous annihilation events.

The other two momentum components $p_{x,y}$, perpendicular to the propagation direction, cause the angular deviation from the colinearity of the annihilation γ -quanta according to [79]:

$$\Theta_{x,y} = \frac{p_{x,y}}{m_0 c}. \quad (3.32)$$

This formula holds for small angles. $\Theta_{x,y}$ can be registered at the same time in both x and y directions by a coincidence measurement. The momentum of the thermalized positron is less significant than that of most electrons. This may be ascribed to the Pauli principle and the resulting distribution of the electron momenta up to the Fermi momentum. Even though positron is a Fermion, it can thermalize, because there is only one positron in the sample at a given time. Thus, positron probes the electron distribution in the momentum space. The electron structure studies are mostly performed by ACAR because of the insufficient momentum resolution of DBS. In case of the localization of positrons in open-volume defects, the fraction of core electrons participates in the annihilation process decreases relative to that of valence electrons. The momentum distribution of the annihilating electrons shifts to smaller values. That is based on the fact that the momentum of the valence electrons is distinctly lower. This implies that a smaller Doppler broadening of DBS and a smaller deviation of the ACAR are obtained in this case.

3.3.2 Measurement of annihilation radiation Doppler broadening

The measurement of Doppler broadening necessitates an energy-dispersive system. Liquid-nitrogen cooled pure germanium (Ge) detectors are used for that purpose. The annihilation photons create electron-hole pairs in a high-purity Ge crystal. Under a high-voltage field, a charge separation is obtained. This generates an electric pulse in the preamplifier. Its amplitude is proportional to the photon energy of the detected γ -quantum and can be stored after main amplification and digitizing in the multi channel analyzer. The collection of several millions counts is allowed by the digital peak-stabilizing system integrated in the MCA. The measurement time is short relative to that of the lifetime experiments. To evade the pile-up effect in the detector, Ge-detector must be kept sufficiently far from the sample. This allows performing both lifetime and Doppler broadening experiments simultaneously. The diagram of the experimental setup is shown in Fig. 3.15.

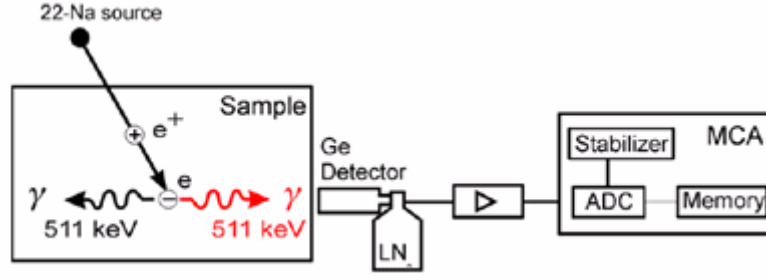


Fig. 3.15: Schematic diagram of the Doppler broadening experiment. A LN_2 cooled Ge-detector is used to measure the energy distribution of the annihilation line. The signal of the Ge-detector is processed by the preamplifier included in the detector. The output signal of the amplifier is provided to a spectroscopy amplifier. Its output signal is stored in the MCA after analog-to-digital conversion. Taken from Ref. [79].

3.3.3 Line shape parameters

Positrons trapped into open-volume defects have a clear effect in the Doppler broadening spectrum $N_D = f(E)$ as shown in Fig. 3.16. There are two parameters for describing the Doppler broadening of the annihilation line. The S parameter, the so-called valence annihilation parameter, is calculated as the number of events of the central low momentum region of the spectrum, N_S , divided by the total area under the whole curve N_O after subtraction of the background [79],

$$S = \frac{N_S}{N_O}, \quad N_S = \int_{E_0 - E_S}^{E_0 + E_S} N_D dE. \quad (3.33)$$

Moreover, the W parameter, or core annihilation parameter, is considered in the high momentum area of the spectrum as illustrated in Fig. 3.16. It is defined as the number of events in a fixed energy interval N_W divided by N_O ,

$$W = \frac{N_W}{N_O}, \quad N_W = \int_{E_1}^{E_2} N_D dE. \quad (3.34)$$

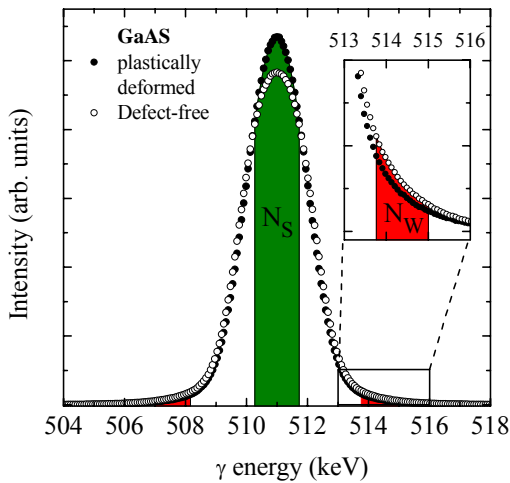


Fig. 3.16: Doppler broadening spectra of two samples: for the defect-free GaAs:Zn, reference and plastically deformed GaAs [79]. S and W parameters are evaluated by the illustrated areas divided by the area under the whole curve. Both spectra are normalized to the same area.

S and W parameters are also called Shape and Wing parameter, respectively. The S parameter is calculated whereas the interval limits are chosen around the center of the annihilation line energy $E_0 = 511$ keV, $E_0 \pm E_S$. The limits for the evaluation of W parameter, E_1 and E_2 , should be selected far outside the center, so that there will be no influence of the valence electrons any more.

The chosen limits must remain constant for all spectra to be evaluated and compared. In Fig. 3.16, the intersection positions of the two curves of the reference and plastically deformed samples are taken as the interval limits for the determination of S parameter. In such a way, a maximum sensitivity for the defect-induced change in the line shape could be obtained. Frequently, the interval limits are chosen to give an S parameter of 0.5 in the defect-free, reference, sample. Thereafter, W parameter should be evaluated starting at a limit considerably far away from the limits of S parameter. The limits were set to (511 ± 0.8) keV for evaluation of S and to $E_1=513.76$ and $E_2=515$ keV for the W parameter [79]. Usually, S and W parameters are normalized to their corresponding values of the bulk defect-free sample, S_b and W_b . This leads to a reliable comparison of the obtained values. This holds only for the spectra measured with the same spectrometer. This is because the normalized line shape parameters depend on the energy resolution of the system. S and W parameters are responsive to the type and concentration of the defect. But W parameter is more sensitive to the chemical surrounding of the annihilation site. That is due to the fact that the core electrons have high momenta and contribute mainly to the W parameter. The chemical surrounding of the annihilation site can be identified using the high momentum part of the momentum distribution [98-101]. This permits the identification of vacancies and vacancy-impurity complexes, in particular when measurements are compared to the theoretical calculations of the momentum distribution [98]. A third parameter, R , was introduced. It depends only on the defect types involved and not on the defect concentration [102]. It is defined as:

$$R = \frac{\left| \frac{S - S_b}{W - W_b} \right|}{\left| \frac{S_d - S_b}{W_d - W_b} \right|}. \quad (3.35)$$

The S -versus- W plot is used rather than the numerical computation of R using Eq. 3.35. The slope of the straight line through (W_b, S_b) and (W_d, S_d) gives the value of R for one defect type. S_d and W_d correspond to the complete annihilation in the defect (saturated trapping). Then, in some cases, the analysis of the linearity of the S - W curve can be used to identify how many defect types are detected by positrons. Moreover, the fraction of positrons annihilating in the defects may be estimated [103,104]. In case of the existence of only one defect type, the apparent S parameter can be derived by weighting the sum of the S_b and S_d as [103]:

$$S = (1 - \eta)S_b + \eta S_d. \quad (3.36)$$

η , the weighting factor, is the fraction of positrons annihilating in the defect and is expressed as [79]:

$$\eta = \int_0^{\infty} n_d(t) dt = \frac{\kappa_d}{\lambda_b + \kappa_d}. \quad (3.37)$$

η can be determined from one Doppler measurement provided that S_b and S_d are known from reference experiments [79]. The trapping rate can be determined as:

$$\kappa_d = \frac{1}{\tau_b} \frac{S - S_b}{S_d - S}. \quad (3.38)$$

Thereafter, the defect concentration can be estimated.

3.3.4 Coincidence Doppler-broadening spectroscopy

The high momentum part of the Doppler spectrum measured with a single Ge detector shows a relatively high background. Thus, it may not be used for the analysis of the core electron annihilation. The background comes from the pile-up effect in the Ge detector and Compton scattering of the start γ -quanta, 1.274 MeV, released from the ^{22}Na source. The coincident detection

of both 511 keV gamma quanta from a single annihilation event, the so-called coincidence Doppler broadening spectroscopy (CDBS), reduces effectively the disturbing background and hence permits clearly the observation of the high momentum annihilation distribution [98-100]. Two Doppler spectra are shown in Fig. 3.17. One is measured using only one Ge detector and the other by coincidence Doppler broadening. The dimension of the background reduction is clearly shown in the figure. Using CDBS, the background may be additionally suppressed by more than two orders of magnitude.

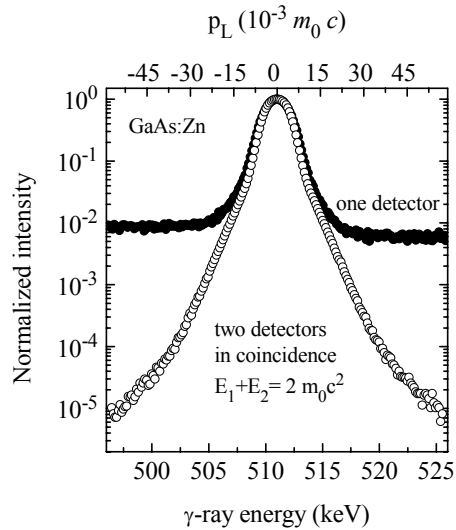


Fig. 3.17: Two Doppler broadening spectra of GaAs:Zn normalized to the same area. One of them is measured (●) with a single Ge detector and the other was measured (○) by CDBS. The background reduction is clearly demonstrated.

Important information on the chemical surrounding of the annihilation site is carried by the high energy part of the Doppler spectrum [98,105,106]. The momentum properties of core electrons are not affected by chemical bonds and are specific for a certain atom. Positrons are localized in an open-volume defect, e.g. a vacancy, annihilate with the electrons of the adjacent neighbor atoms. Hence, in compound semiconductors, the analysis of the high momentum part allows the identification of the vacancy sublattice or impurity-vacancy complexes [98,101]. Frequently, the specific spectrum of a chemical element of interest is obtained by carrying out CDBS measurements in a pure defect-free elemental crystal. Often, in various environments, the characteristic features of the high momentum region in the spectrum are preserved. This allows us to identify whether the detected vacancy is isolated or surrounded by a certain atom (e.g. Cu in GaAs:Te). The analysis and interpretation of the Doppler spectrum is found to be easier by introducing ratio curves [107,108]. The ratio curves can be obtained by dividing the measured spectra to the spectrum of the defect-free reference sample.

3.4 Procedure of positron annihilation experiments

The present study is based predominantly on the results of temperature-dependent measurement of the positron lifetime. A conventional fast-fast coincidence system with a time resolution of 225 ps was used. A small quantity of radioactive liquid ^{22}Na -salt was deposited on 4.5 μm thick Al-foil. It was used as a positron point source. The source is located in sandwich geometry between two identical samples. The whole sample-source arrangement is wrapped in aluminum foil. Typical source activities are 0.75-1.3 MBq. The measurement temperature could be varied in the range from 20 K – 550 K. Usually, the temperature program of lifetime experiments is set to start the measurement at the lowest temperature and increase the temperature in steps of 33K. So, in this work, most often the temperature program will include following temperatures: 30 K, 66 K, 100 K,

133 K, 166 K, 200 K, 233 K, 266 K, 300 K, 333 K, 366 K, K, 400 K, 433 K, 466 K, 500 K, 533 K, and 550 K. About 4×10^6 annihilation events were accumulated in each lifetime spectrum. Semi-insulating (SI) or *p*-type Zn-doped GaAs samples showing no positron trapping were used as reference samples and give a positron lifetime of 228 ps [109,110]. Three lifetime components were assumed for the source correction. Two components correspond to the annihilation of positron in the NaCl or Na₂CO₃ source (τ_{NaCl}) and the covering Al foil (τ_{Al}). The third component is related to the annihilation from a positronium state (surface state). Usually, the source correction is carried out by the analysis of the spectrum of a defect-free reference sample. τ_{NaCl} and τ_{Al} are fixed to 380 ps and 162 ps respectively [111]. The third component and the intensities of all components are used as fitting parameters, they are left free. The source parameters are considered as resolved when a positron bulk lifetime of 228 ps was obtained. Frequently, the source contribution is in the order of 16 %, where the intensity of the third component is always less than 0.5 %.

Two Ge- γ -detectors were used to perform the coincidence Doppler broadening spectroscopy measurements. About 5×10^7 coincident events during 6 days were accumulated in each Doppler spectrum. Usually, the CDBS curves are normalized to that obtained in a SI or Zn-doped GaAs reference sample showing no positron trapping for more qualitative analysis. In case of the conventional Doppler spectroscopy (one detector only), more than 1×10^6 counts are accumulated for the annihilation peak. *S* and *W* values are obtained as described above.

3.5 Other techniques

In addition to positron annihilation spectroscopy techniques, some further methods were used for the characterization of the samples in this work.

3.5.1 Hall-effect measurement

The basic idea of Hall-effect is the creation of the potential difference (Hall voltage) on the opposite sides of the sample through which an electric current is flowing, created by a magnetic field perpendicular to the current. Hall voltage is perpendicular to both the direction of the current through the sample and the direction of the external magnetic field. The preparation of Ohmic contacts is necessary for carrying out Hall-measurement. The Hall-effect technique is a well-known method in semiconductors for the determination of the type, concentration and mobility of the charge carriers. Temperature dependent Hall-measurements (TDH) enable the determination of the activation energy of the predominating donor or acceptor defect when the level is not too deep in the gap. It also supplies information on the defect density. The carrier concentration can be used to estimate the position of Fermi level, which helps in the interpretation of positron annihilation data. The defect concentration may be calculated in some cases. The determination of the defect level using the Hall-effect measurements is possible only in special situations.

3.5.2 Secondary ion mass spectroscopy

Secondary ion mass spectrometry (SIMS) works on the principle that bombardment of a sample with a beam of ions with medium energy (1-30 keV) results in the ejection or sputtering of atoms from the sample surface. A fraction of these ejected atoms leave as positively or negatively charged ions, which are referred as secondary ions. The collection of these sputtered secondary ions provides information on the composition of the sample. The elements are identified by their atomic mass which is analyzed by a mass spectrometer. Thus, SIMS is a destructive technique. The SIMS

sensitivity is affected by the yield of secondary ion sputtering, which depends on the energy, nature and incidence angle of the primary ion beam, the sample material and specimen crystallographic orientation. Therefore the sensitivity of SIMS is enhanced by the appropriate choice of the primary ion beam. Often, oxygen atoms are used for sputtering electropositive elements or those having low ionization potentials such as Na and Al. Sputtering of negative ions from electronegative elements, e.g. C and As, can be performed using cesium atoms. The fundamental components of a SIMS spectrometer are illustrated in Fig. 3.18. There is an ion gun to produce the primary ion beam, an extraction electrode in order to collect the secondary ions of given polarity, a mass spectrometer to separate and sort out the secondary ions according to their mass, and finally the detector. In some machines, an electron flood gun is used to compensate the charge that builds up during ion bombardment of poorly conducting samples. All components are built in an ultra-high vacuum chamber.

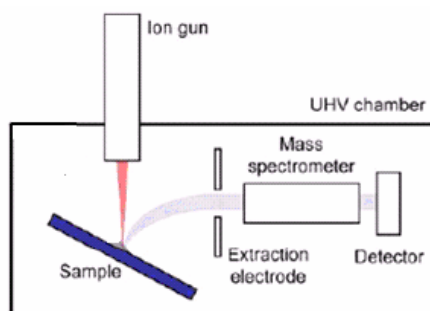


Fig. 3.18: Schematic diagram of a SIMS spectrometer.

Monitoring the secondary ion emission with respect to the sputtering time provides the depth profile of the composition of the sample. Depth profiling aims to obtain information on the variation of the decomposition as a function of the depth below the initial surface. The depth profile can be obtained by registering sequential SIMS spectra as the surface of the sample is gradually etched away by the incident primary ion beam probe. Thus, the intensity of a given mass signal as a function of time reflects exactly the variation of its concentration with the depth below the surface. SIMS has several advantages over other composition analysis methods: Its ability to identify all elements comprising H and He and its sensitivity to elements present in very low concentration level, e.g. dopants in semiconductors.

4. Variable energy positron annihilation spectroscopy

4.1 Introduction to slow positron beam technique

Positrons emitted from the source, in case of sample-source sandwich, penetrate instantaneously the sample. A large implantation depth of positron is caused by the broad positron energy distribution up to 540 keV for ^{22}Na . In semiconductors, investigation the thin layers and defects in the near surface region and at the interfaces is of importance. The conventional techniques have only a limited applicability to such studies. These investigations became accessible by the advent of the slow positron beam technique. Simple linear accelerators are used to set the monoenergetic positrons (slow positrons) to defined energies, which leads to a defined small penetration depth. This technique is also called as variable energy positron annihilation spectroscopy (VEPAS). Setting the positron energy in a range of a ~ 0 keV to several tens of keV allow the monitoring of defects as a function of depth, what is called defect depth profile. Monoenergetic positrons are obtained through the moderation process. A small fraction of less than 1% of the incident positrons undergoes the moderator. Unmoderated positrons must be separated from the monoenergetic positron beam that is used for the defect experiment after certain acceleration. The moderation needs a spatial separation between the source and sample, and thus a beam guidance system should be used.

4.2 Positron source and moderation process

The energy emission spectrum of radioactive ^{22}Na source is illustrated in Fig. 4.1. Moderation process is related to the fact that many solids have a negative positron work function Φ_+ .

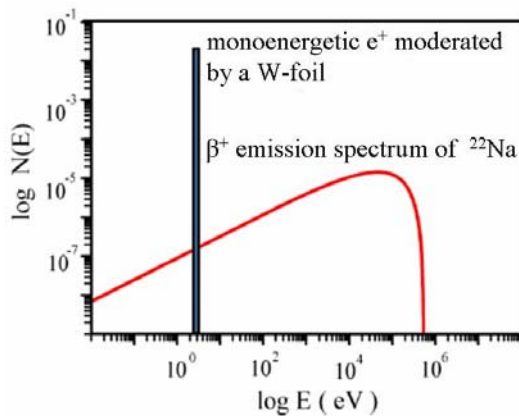


Fig. 4.1: Positron emission spectrum of a ^{22}Na source is schematically represented [79]. $N(E)$ is the number of positrons per energy channel E . The narrow curve positioned at 3 eV shows the energy distribution after moderation in tungsten.

Usually, transmission geometry with a thin moderator foil located directly on the top of the source capsule is used. The thickness of the moderator foil is much thinner than the positron mean penetration depth. As a result, the majority of positrons penetrate the foil unhindered with high energy and only a small fraction of positrons thermalize and then diffuse there. Once they reach the surface, during their diffusion, they are reemitted from the film with a kinetic energy of about the thermally broadened work function Φ_+ . Fig. 4.2 shows a scheme of positron moderation process in transmission geometry by a (110) tungsten foil.

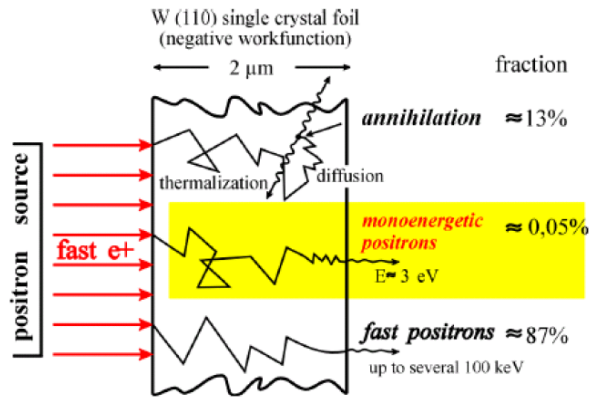


Fig. 4.2: Schematic representation of positron moderation process in transmission geometry by a (110) tungsten foil. A small fraction stops in the foil and annihilates there. They may spontaneously be released upon reaching the surface due to the negative work function of W. The majority of positrons leave the moderator foil with a high energy. (From Ref. [79])

Moderators are preferred to be made from high atomic number materials, since the ratio of the mean diffusion length to the thermalization distance is larger. A defect-free single crystal of tungsten (W) with several μm thick is an appropriate material. Vehanen et al. [112] have determined the work function of (110) oriented single crystal W to be $\Phi_+ = -3 \text{ eV}$. The moderation efficiency is defined as the ratio of the number of moderated slow positrons to the total number of the incident positrons. It amounts to 10^{-4} for W. Solid-state rare gas moderators are obtained by depositing a thin film of rare gas such as neon on a carrier foil at low temperature [113]. These moderators are characterized by very high efficiency. SiC as a field-assisted positron moderator could be also used [114]. A stronger positron sources, and thus an intensive radiation protection, is required for positron beam technique because of the low moderation efficiency.

4.3 Guidance systems of slow positron beam

The monoenergetic positrons leaving the moderators should be separated from those which are unmoderated before they can be used in the experiment. This separation occurs by an energy filter through the beam guidance. It may be achieved in a magnetically guided system using internal electrodes in an $E \times B$ filter or by utilizing external magnetic fields perpendicular to the beam direction. Bent solenoids are preferred to be used which is a simpler method. The unmoderated positrons are stopped in a shield.

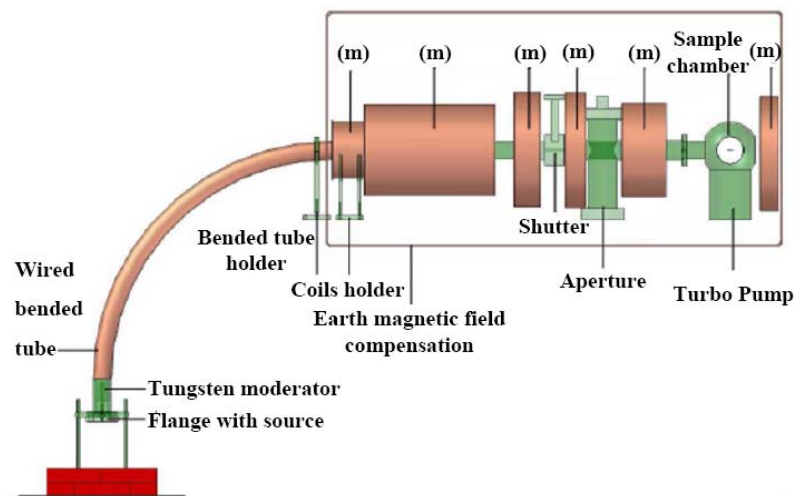


Fig. 4.3: Schematic diagram of the slow-positron-beam system POSSY at Martin Luther University Halle-Wittenberg. Moderated positrons are fed through the collimator by the solenoids and are accelerated to the sample. The whole longitudinal magnetic field is generated by the guidance coils (m).

A schematic diagram of the positron beam technique at Martin Luther University is shown in Fig. 4.3, in which bent solenoids are used. High vacuum of 10^{-8} bar is enough for the guidance system and positron studies near the sample surface. Ultra high vacuum is needed for surfaces studies. In this situation, a differential pumping station should be used to separate the sample chamber. As illustrated in Fig. 4.3, the source-moderator arrangement is placed in front of the bended tube which acts as a filter. The monoenergetic positron beam leaving is guided into the system axis and through a linear accelerator supplying a maximum energy of 50 keV. Positrons are compelled to undergo in a helical path due to the longitudinal magnetic field which is generated by a system of guidance coils (Fig. 4.3). These coils guarantee that all released positrons reach the sample.

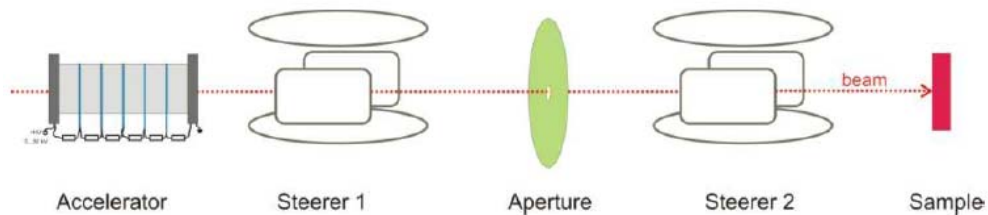


Fig. 4.4: Schematic representation of the steerers which guide the positron beam to hit the target.

An aperture of about 5 mm diameter is used. As illustrated in Fig. 4.4, two steerers should be utilized in order to the positron beam passes through the aperture and finally hits the sample. One is set between the accelerator and the aperture and the other is present between the aperture and the sample. These steerers should be adjusted via their calibration. The correct values of the current for X-Y deflection of the steerers are determined by the count rate contour plot. The calibration has to be done under vacuum. In case of the aperture calibration, the Ge detector should be placed at the aperture and shielded by lead blocks to reduce the background. A scan is carried out by varying the current of the coils, which are located before the aperture. Measurement for 5 seconds for each point during the scan gives a clear picture, from which one can determine the position of the aperture. Fig. 4.5 represents an example of contour plot at the aperture which indicates the presence of the aperture approximately at the middle, where the count rate is minimum value. From such plot one should determine both X and Y coordinates, which will be used for the calibration of the beam. The section deviation, as shown in Fig. 4.5, of the space between the coils corresponds to the current of the coils. This is digitized by using a computer program, where 0 corresponds to -1 Ampere, 2000 corresponds to 0 Amp and 4000 corresponds to +1 Amp. The coordinates X-Y of the deflection coils of the aperture at 10 keV, Fig. 4.5, are 1905-1970.

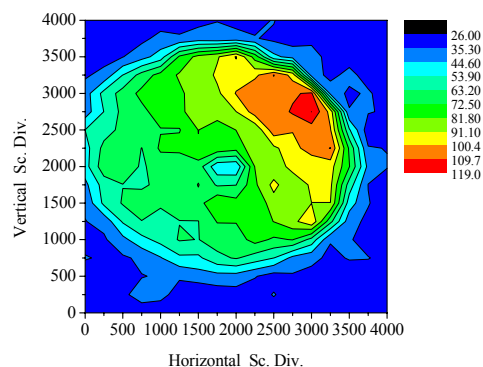


Fig. 4.5: Scan of the aperture at 10 keV.

For calibration at the sample position one should put the Ge detector close to the sample and repeat the same procedure but using the X-Y values determined previously for the aperture. Fig. 4.6 illustrates a contour plot of sample calibration at 3 keV which is performed by varying the current of the coils before the sample. The position of the sample is clearly shown at the middle where the count rate has the maximum value. X-Y values for the sample steerers at 3 keV are 1917-2120. X-Y (current settings) for both aperture and sample steerers should be tabulated for all energies which are used as an input data for a real experiment. More details about the build up and construction of the slow positron beam can be found in [115].

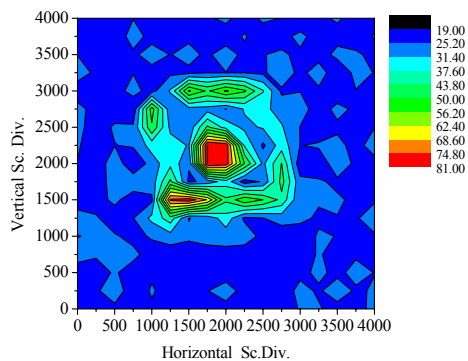


Fig. 4.6: Contour plot obtained by calibration the coils pairs of the sample at 3 keV. One can see obviously the sample position at the middle of the plot.

4.4 Basics of the measurement

Doppler broadening is the most suitable technique to be applied for a slow positron beam. It is completely like the conventional procedure, where the Ge detector is placed close to the sample outside the sample chamber. This is possible since the energy of the annihilation radiation is high enough to permit the transmission of the γ -quanta through a thin stainless-steel wall of the beam system. As mentioned previously, both line shape parameters S and W are used to identify the defects and estimate their concentrations. In contrast to conventional Doppler, the birth γ -quanta do not contribute to the background of the spectrum, because the sample is present far from the source in case of a slow positron beam system. Also, there is no source contribution to the spectrum ascribed to the annihilation in the foil source. These features lead to high quality Doppler spectrum. The annihilation parameters are measured as a function of the positron beam energy, i.e. positrons implantation depth. Positron lifetime is applicable only in case of using pulsed beams providing the start pulse by a particularly designed bunching system. For more details see e.g. [116-118]. On the other hand, the conventional lifetime setup is not appropriate for POSSY because the time of flight is much longer than the lifetime of the sample itself. ACAR can be also carried out in the slow positron beam, which is of fundamental importance for obtaining information about the electronic structure at the surface, interfaces or in thin epitaxial layers (e.g. [119]). It is important to note that the back diffusion experiment in the slow positron system is also applied for determining the defect densities. The annihilation parameters at the surface or the fraction of positronium formed at the surface can be used for determining the fraction of positrons diffusing back to the surface, f_s . This is because the annihilation parameters of the surface frequently differ from those of the bulk. Positronium formation can usually occur in semiconductors at the surface [79]. Due to the fact that the trapped positrons can not reach the surface again, the back-diffusing fraction of positrons is a function of the defect concentration in addition to the positron diffusion constant and the implantation depth. f_s is measured as a function of the incident positron energy which allows determining the trapping rate versus the depth. Correlation of positron lifetime and Doppler broadening measurements is preferred for more reliable results. The total trapping rates for all

positron traps can be determined from the back-diffusion measurements. Therefore, the defect densities can be estimated even in case of trapping saturation, i.e. at very high concentrations, which can not be determined in case of the conventional measurements. The total trapping rate in plastically deformed Ni samples, showing complete trapping, was determined from positron diffusion length which is obtained by back-diffusion experiment [120].

The total trapping rate (κ_{total}) is given by [120]:

$$\kappa_{\text{total}} = \frac{1}{\tau_b} \left(\left(\frac{L_{\text{ref}}}{L} \right)^2 - 1 \right) \quad (4.1)$$

L_{ref} is the diffusion length in the defect-free sample. L is the diffusion length measured in the sample under investigation.

4.5 Defect depth profile

The defect depth profile is obtained from the measured change of the annihilation parameters as a function of the incident positron energy provided that the positron implantation profile is known. The variation of the positron energy permits the revealing of defects as a function of the penetration depth z , what is so-called defect depth profiling. The penetration or implantation profile $P(z, E)$ of positrons having energy E is expressed by [121,122]:

$$P(z, E) = \frac{mz^{m-1}}{z_0^m} \exp \left[- \left(\frac{z}{z_0} \right)^m \right] \quad \text{where } z_0 = \frac{AE^r}{\rho \Gamma \left(1 + \frac{1}{m} \right)}. \quad (4.2)$$

A , m and r are empirical parameters and their extensively used values are $4.0 \mu\text{gcm}^{-2} \text{keV}^{-r}$, 2 and 1.6, respectively. These parameters were also experimentally determined by Gebauer et al. [123]. ρ and Γ denote the mass density of the sample under investigation and gamma function. The mean penetration depth is given by [122]:

$$\bar{z} = AE^r / \rho \quad (4.3)$$

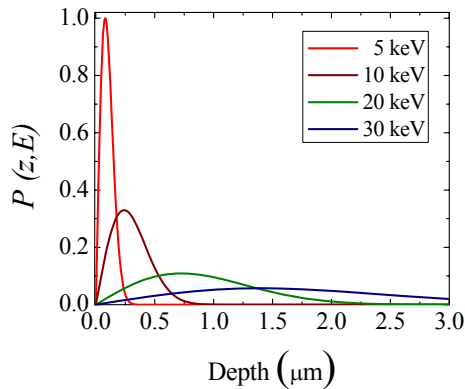


Fig. 4.7: Implantation profile in GaAs calculated for different incident positron energies according to Eq. 4.2 using the values of parameters which are mentioned above.

The positron penetration profile is known also as Makhov profile. The profile parameters can be theoretically calculated from Monte-Carlo simulations [124]. The theoretical calculation showed that the parameters A and r depend on the material [125]. The thermalized positrons exhibit, during their diffusion, a depth distribution as described by Eq. 4.2. Figure 4.7 illustrates an example of Makhov profiles in GaAs for different positron energies. As one can see, the full width at half maximum (FWHM) at low energies is small which is indicative of the small mean penetration depth, as can be also calculated from Eq. 4.3. With increasing the positron energy the

penetration depth and thus the FWHM increase. The peak flattens at high energies. This increases the probability of positrons to be found in different depths.

At high positron energies the defect depth profiling has some noticeable limitations, as sharp defect structures present relatively deep in the sample are smeared out when folded with the broad positron penetration profile. The $S(E)$ plot can be used for determining the parameters of the implantation profile. VEPFIT (variable energy positron fit) program is used to fit the S parameter curves using systematically varying A and r parameters of the Makhov profile.

The profile of the possible annihilation parameters, such as line shape parameters, lifetimes or their intensities, in terms of the depth represents the depth profile convoluted with the implantation profile $P(z,E)$ which is affected by the positron diffusion. Usually, the defect depth profile can hardly be identified directly. In the numerical programs, the sample should be split into layers which are considered to be so thin that a constant defect concentration and constant positron density are assumed there. Fitting the measured annihilation parameter as a function of the energy is normally carried out in a non-linear method, which gives the defect distribution perpendicular to the surface. VEPFIT is one of the most widely used computer programs for fitting the data of the slow positron beam [126]. A Gaussian function or a step function or a simple slice structure must be chosen as the defect profile. Sometimes it is difficult to decide which function is the better choice to imitate the real defect profile. This is because the broad implantation profile of positrons and positron diffusion, which depend on the defect concentration. The fraction of positrons diffusing back to the surface can be obtained also from these programs.

4.6 Determination the lateral resolution of POSSY

The lateral resolution of the positron beam at the sample position is determined by using three aluminum sample holders with holes at the sample position having different diameters (2, 3 and 4 mm). This is carried out by a scan of the sample holder through the vertical direction by moving it in steps of 1 mm.

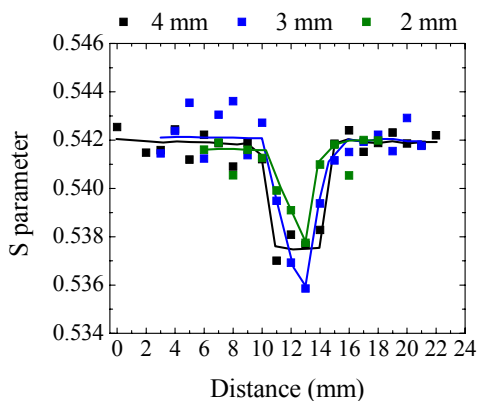


Fig. 4.8: Low momentum parameter as a function of the distance through scanning the sample holder in the vertical direction. The positron energy is 10 keV. The lateral resolution at the sample position is ~ 4 mm.

If the positron beam strikes the Al sample holder positrons annihilate with Al electrons having characteristic annihilation parameters. Fig. 4.8 shows the S parameter measured at a positron energy of 10 keV while scanning the sample holder through its vertical direction. It is expected to obtain a different value of the S parameter in case when the positron beam hits the position of the hole, i.e. positrons pass through the hole and do not annihilate in the Al sample holder but annihilate somewhere else such as the wall of the beam system. Thus, if the beam hits the Al sample holder either above or below the aperture position S parameter of about 0.542 is obtained. As shown in Fig. 4.8, the S value decreases to reach 0.538 in the distance between 11 and

14 mm in case of using the 4 mm diameter of the aperture, where most of positrons pass through the hole and thus do not annihilate in the Al sample holder. For smaller diameters of the aperture (2 and 3 mm), at 11 and 14 mm the S parameter decreases below the value of Al. However, this decrease is not complete compared to the 4 mm aperture. This is because that only a fraction of positrons passes through the aperture and the other annihilate in the Al sample holder which increases the S parameter over the corresponding value for sample holder of 4 mm aperture. In case of the 2 mm diameter hole, only small fraction of positrons pass through the hole, thus S parameter in the distance between 11 and 14 mm is higher than the corresponding values for the larger diameter holes as clearly shown in Fig. 4.8. Then, it can be inferred that the lateral resolution (diameter) of the positron beam at the sample position is about 4 mm.

5. Vacancy generation during Cu diffusion in semi-insulating and Zn-doped GaAs

5.1 Introduction

Despite extensive studies of GaAs during the recent decades, the native point defects in this material are not yet fully understood. The thermodynamic properties of these defects in GaAs are of great technological interest. The thermodynamic analysis allows predicting the concentrations of the point defects incorporated into the crystal under equilibrium conditions [34,127]. The positron is sensitive to the electrical potential of point defects and has proved to be a valuable nondestructive probe for vacancy-type defects. During the past decades, PAL has been intensively applied to characterize defects in various semiconductors [79]. But in many cases it is difficult to conclude from the annihilation parameters alone which defect is responsible for the positron trapping. The basic thermodynamic considerations displayed in this chapter helped a lot in characterizing the origin of the observed vacancy-complex. The native point defect concentration can be expressed as a function of temperature and arsenic vapor pressure according to the law of mass action [34]. Taking into consideration that PALS is not very sensitive to the surrounding of the observed vacancy-like defects, coincidence Doppler broadening spectroscopy can be performed to obtain information on the chemical environment of positron trapping centers. Copper is found as an unintentional impurity in most semiconductors. This is owing to the fact that Cu is a rapidly diffusing contaminant already at low temperatures. Cu exhibits an unusually large diffusion coefficient in many semiconductor crystals. In GaAs, it was found to be as high as $D = 1.1 \times 10^{-5} \text{ cm}^2 \text{ s}^{-1}$ at 500 °C and $D = 1.8 \times 10^{-9} \text{ cm}^2 \text{ s}^{-1}$ at 100 °C [17]. Cu diffuses very fast by interstitial diffusion (kick-out process) [11].

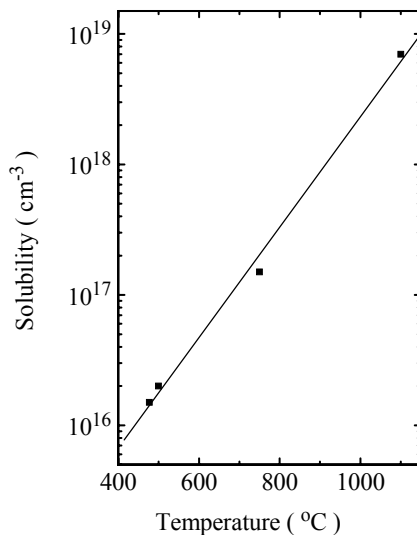


Fig. 5.1: Solubility of Cu in undoped GaAs as a function of temperature (Ref.[17]).

Figure 5.1 presents the experimentally obtained solubility of Cu as a function of temperature as reported in Ref. [17]. Moreover, the solubility was calculated to be $5 \times 10^9 \text{ cm}^{-3}$ at 100 °C [17]. Depending on the cooling speed after a diffusion process, only a small fraction of the total Cu concentration is electrically active as acceptors. The portion of Cu that remains electrically inactive forms Cu-Ga precipitates [128]. The study presented in this chapter aims to the

investigation of point defects quenched from different equilibrium states by means of positron annihilation lifetime spectroscopy (PALS).

5.2 Experimental work

At temperatures lower than its melting point (1240 °C), the GaAs system is composed of two phases (solid and gas). In this case, it has two degrees of freedom in accordance with Gibbs' phase rule. In order to keep the samples under certain equilibrium condition, it is required to fix two important parameters, which are the sample temperature and As ambient gas pressure. At high temperatures, the gas phase consists mainly of the arsenic tetramer As_4 and the partial vapor pressure of gallium is small and thus can be neglected [32]. The defect concentration will therefore be a function of the sample temperature and arsenic vapor pressure. Keeping the sample temperature fixed and varying the As vapor pressure, the chemical composition of the crystal can then be changed. This provides a possibility to investigate the formation of point defects as a function of crystal stoichiometry. However, it is difficult to measure directly the defect concentrations at the high temperatures necessary for their creation. As a result, the high-temperature defect configuration is often frozen by quenching the investigated sample from high to low (room) temperatures. This method was applied in this work. The investigated samples were cut from the semi-insulating undoped and zinc-doped ($[Zn]=3.8 \times 10^{16} \text{ cm}^{-3}$) liquid encapsulated Czochralski (LEC) grown GaAs wafer (5x5x 0.5 mm). The wafers were provided by FCM (Freiberger Compound Materials GmbH). The resistivity of initial SI GaAs material was about $10^6 - 10^7 \text{ } \Omega\text{cm}$. The samples were covered by 30 nm Cu by evaporating it under ultra high vacuum (UHV) conditions. This amount of Cu corresponds to a volume concentration of $6 \times 10^{18} \text{ cm}^{-3}$ which is approximately the upper solubility limit of Cu in GaAs at 1100 °C [17]. The deposited layer thickness was controlled by a thickness measurement device (frequency shift of a crystal oscillator) which was calibrated before by Atomic Force Microscopy (AFM). High purity copper-free quartz ampoules HSQ300 (Heraeus Quarzglas GmbH&Co) were used for the Cu diffusing annealing. Pure As (99.999%) was used as arsenic source. The samples and the arsenic source were sealed in quartz ampoules under high vacuum. Annealing was performed for three hours in a two-zone temperature furnace at 1100 °C (sample temperature). Fig. 5.2 shows the temperature profile of the two-zone furnace, which was used for the annealing process.

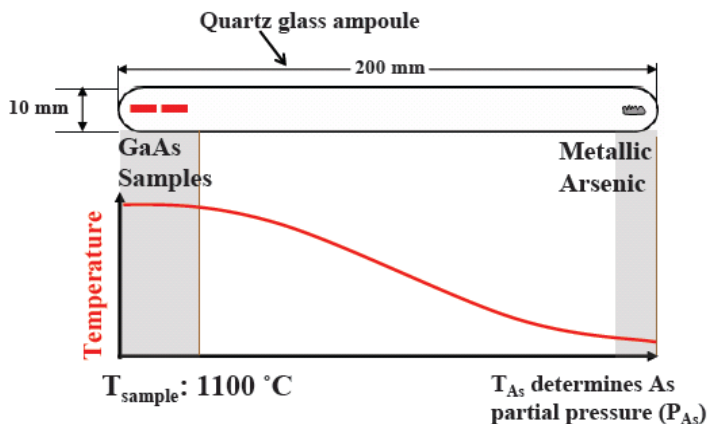


Fig. 5.2: Temperature profile of the two-zone furnace used for the annealing of GaAs samples under different As pressures.

The arsenic vapor pressure is determined by the temperature at the coldest end of the ampoule and corresponds thus to the temperature of the metallic arsenic (T_{As} in Fig. 5.2) provided that a sufficient amount of arsenic has to be used to avoid its complete sublimation. The temperature of

the arsenic source was varied in the region of 550 – 740 °C, what corresponds to an As-pressure of 0.2 – 9.68 bar [129]. Corresponding arsenic pressure values were determined according to the temperature dependence of P_{As} taken from Ref. [129] (Fig. 5.3).

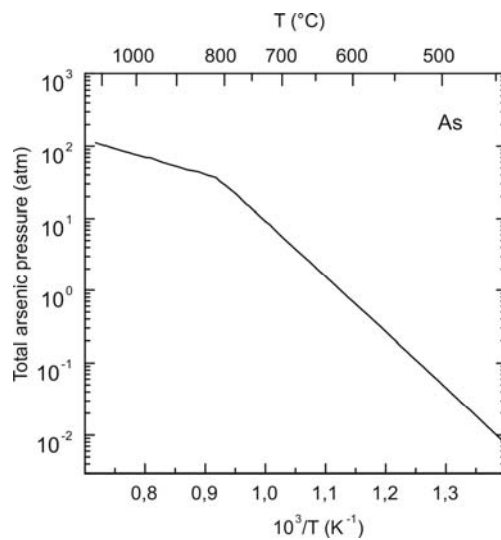


Fig. 5.3: Vapor pressure of metallic As as a function of the temperature, taken from Ref. [129].

After annealing, the ampoules were quenched into water at room temperature. According to the solubility, Cu is in oversaturated state and Cu atoms have the tendency to leave the lattice and start the out-diffusion, e.g. by forming precipitates. Hall-effect measurements were applied to measure the samples in the as-quenched state. Thereafter, the samples were isochronally annealed in the temperature range up to 900 K. The samples were cooled down relatively slowly after each annealing step. Between the annealing steps, PALS measurements in the temperature range of 20 – 500 K were carried out using a conventional fast-fast coincidence system with time resolution of 225 ps. The ²²Na positron source was sandwiched between two identical 4.5 μm thick Al foils and placed between two identical samples. The spectra were analyzed with the two-component trapping model (one defect type) after source and background correction. Coincidence Doppler broadening spectroscopy (CDBS) was performed with two Ge-γ-detectors with a channel width of 70.60 eV and an energy resolution of 0.9 keV at 511 keV. The annealed SI GaAs samples were investigated by temperature dependent Hall-effect (T = 293...373 K). The SI GaAs samples, annealed at 0.2 and 9.68 bar of As vapor pressure were chosen for chemical analysis by titration measurements.

5.3 Results and discussion

5.3.1 Reference measurement

Semi-insulating and Zn-doped GaAs without any treatment were measured as reference samples. Both samples show single component spectra with a lifetime value of 228 ps at 300 K, which presents the defect-free bulk positron lifetime of GaAs crystal [130]. The results are shown in Fig. 5.4. A small increase in the average positron lifetime is observed in the high temperature region (T > 500 K), this is a sign of the detection of vacancies but with very low concentration.

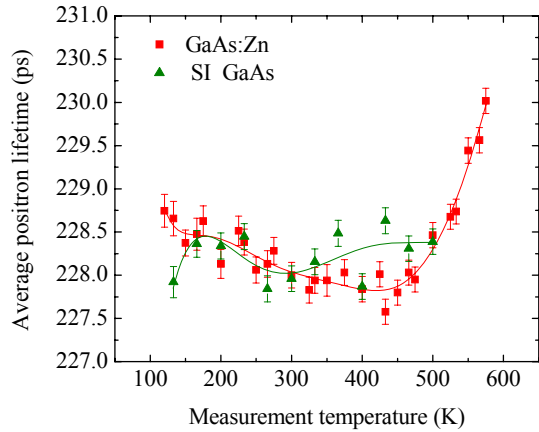


Fig. 5.4: Average positron lifetime as a function of the sample temperature in semi-insulating and Zn-doped GaAs without treatment.

5.3.2 Semi-insulating GaAs

The semi-insulating undoped GaAs sample without any Cu deposition (reference sample) did not show any positron trapping. After Cu in-diffusion, the average lifetime increases only slightly in the high-temperature region, what indicates that a small number of vacancy-type defects is detected.

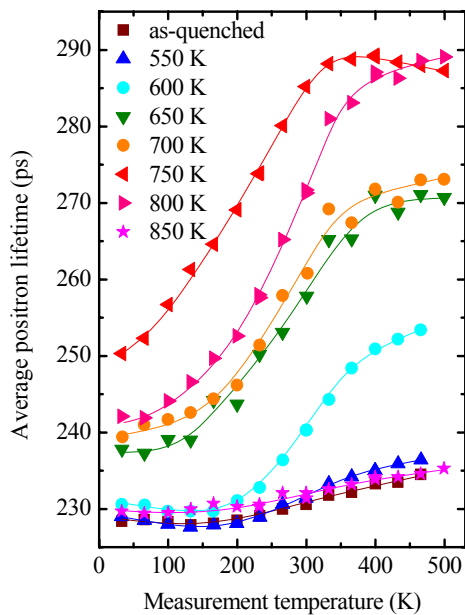


Fig. 5.5: Average positron lifetime as a function of sample temperature in undoped SI GaAs. Prior to the experiment, about $6 \times 10^{18} \text{ cm}^{-3}$ Cu atoms were introduced by evaporating a layer of 30 nm Cu onto the sample surface and by subsequent annealing at 1100 °C under 0.2 bar of As pressure (3h, then quenched into water). The temperature-dependent lifetime experiment was carried out after each annealing step as illustrated in the figure.

Figure 5.5 represents the average positron lifetime versus measurement temperature after different annealing steps performed after Cu in-diffusion. A distinct decrease of the average lifetime at low temperatures is clearly shown for all curves. This is a typical dependence for shallow positron traps (negatively charged, non-open volume defects, such as ionized acceptors), which tend to trap positrons in the extended region of the Coulombic potential, reflecting thereby the properties of the bulk as the annihilation characteristics of the positrons [79,88]. Because of small positron binding energy, shallow traps are effective only at low temperatures, while at higher temperatures positrons are detrapped due to the high detrapping rate. Here, after Cu in-diffusion, the shallow traps must be ionized Cu acceptor. Their concentration is up to $3 \times 10^{17} \text{ cm}^{-3}$ according to the Hall-effect measurements. During annealing up to 750 K, the average positron lifetime increases strongly up to the value of 290 ps, indicating the presence of vacancy-type defects. With

a further increase of the annealing temperature, a rapid decrease of the average positron lifetime was observed. With annealing at temperatures higher than 800 K the vacancy clusters grow and the distance between them becomes larger than the positron diffusion length. Thus, they become invisible for positrons [131]. Another possible reason for the disappearance of the vacancy signal is that vacancy clusters are dissolved. This cannot be distinguished by the obtained data alone.

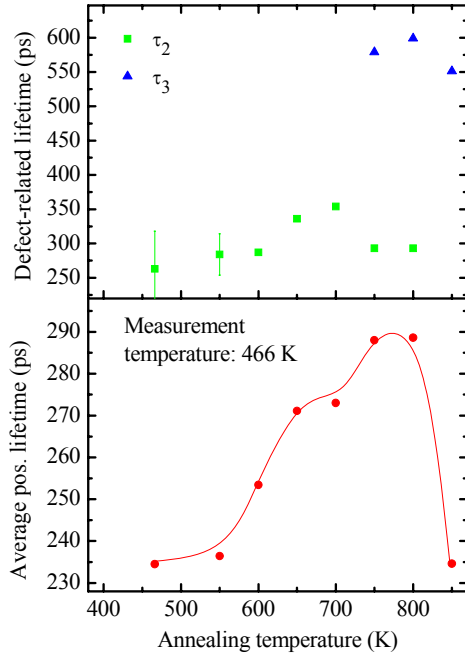


Fig. 5.6: Positron lifetime results of the annealing experiment of undoped semi-insulating GaAs after in-diffusion of $6 \times 10^{18} \text{ cm}^{-3}$ Cu atoms at 1100°C under 0.2 bar of As pressure. The average lifetime is shown in the lower panel. The defect-related lifetime versus the annealing temperature is plotted in the upper panel. The spectra were measured at a sample temperature of 466 K to diminish the influence of the shallow traps.

Figure 5.6 shows the annealing behavior of the average and defect-related lifetimes. It can be shown that the open volume of the detected vacancy-type defect increases during annealing. The defect-related lifetime is much higher than that for monovacancies (250-260 ps) [79]. This must be explained by trapping of positron at small microvoids. The defect-related lifetime τ_3 reaches the value of 600 ps corresponding to vacancy clusters with number of vacancies (n) > 15 .

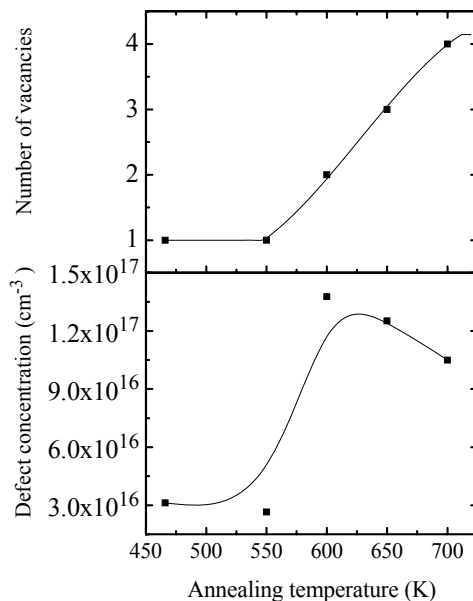


Fig. 5.7: Defect concentration and the number of vacancies as a function of the annealing temperature in undoped SI GaAs after in-diffusion of $6 \times 10^{18} \text{ cm}^{-3}$ Cu atoms at 1100°C under 0.2 bar of As pressure. The number of vacancies in the observed clusters is shown in the upper panel. The defect concentration versus the annealing temperature is plotted in the lower panel. These Data were calculated using the positron lifetime results presented in Fig. 5.5.

The lower panel of Fig. 5.7 represents the defect concentration versus the annealing temperature where the defect concentration increases from $3 \times 10^{16} \text{ cm}^{-3}$ at 466 K up to 10^{17} cm^{-3} at 700 K. The

defect concentration is determined according to Eq. (3.17). Where μ is the trapping coefficient and taken as 10^{15} s^{-1} at 300 K [96,130], τ_b is the bulk lifetime 228 ps [95,132], τ_{av} is the average positron lifetime, it is calculated from the spectra decomposition and τ_d is the defect-related lifetime. The upper panel in Fig. 5.7 represents the number of vacancies versus the annealing temperature where the number of vacancies increase from 1 at 466 K up to 4 vacancies after annealing at 700 K. This was concluded according to the calculation in Ref. [133], which is based on the superimposed-atom model by Puska and Nieminen [80].

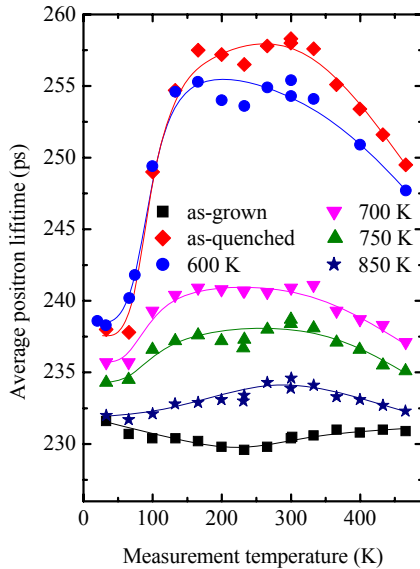


Fig. 5.8: Average positron lifetime as a function of sample temperature in undoped SI GaAs. The samples were annealed at 1100 °C under 0.2 bar of As pressure. The samples were not treated with copper as a reference experiment to the results shown in Fig. 5.5. The temperature-dependent lifetime experiment was carried out after each annealing step as illustrated in the figure.

To show the effect of Cu, the results above are compared to the sample which was not treated with Cu and annealed under very similar conditions. As shown in Fig. 5.8, the as-quenched sample shows a higher value of the average lifetime. This can be attributed to the trapping of positrons in vacancies. With increasing the annealing temperature the average lifetime decreases. This is owing to the fact that the vacancies disappear. In contrary, in case of GaAs samples after Cu in-diffusion (Fig. 5.5), almost no change of the average positron lifetime was observed in the as-quenched state. However, during the annealing steps until 750 K the average positron lifetime increases strongly, and at annealing temperatures higher than 850 K the vacancy cluster signal almost disappears.

Figure 5.9 illustrates the temperature dependence of the average and defect-related lifetime on the sample temperature for undoped semi-insulating GaAs annealed at 1100 °C for 3 hours under different arsenic vapor pressures compared with an unannealed reference sample. No Cu was incorporated into the samples. As shown in the lower part, no vacancy defects were observed in as-grown semi-insulating GaAs. The average positron lifetime of the reference sample is close to the defect-free bulk value of 228 ps at all measurement temperature. After annealing, the average positron lifetime is strongly enhanced what proves the generation of vacancy-like defects during the annealing treatment.

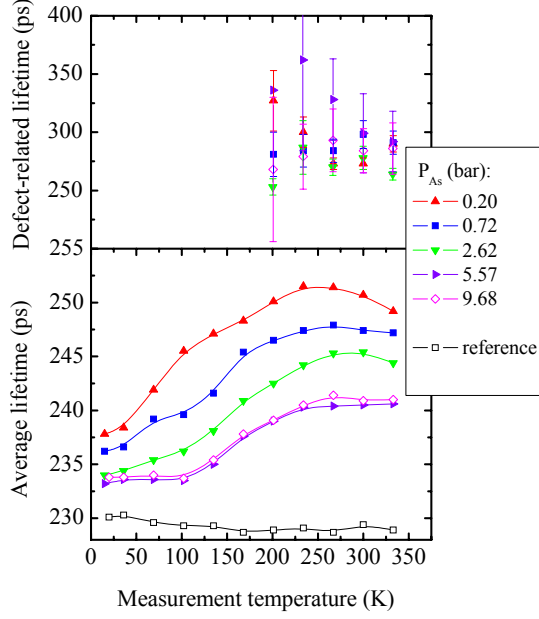


Fig. 5.9: Average and defect-related positron lifetime versus measurement temperature for undoped semi-insulating GaAs annealed at 1100 °C for 3 hours under different arsenic pressures compared to a not annealed reference sample. Lines are to guide the eye only.

The decrease of the average positron lifetime at low temperatures is due to positron trapping at shallow positron traps. With increasing the arsenic vapor pressure during annealing, the average positron lifetime decreases. The maximum average lifetime is observed after annealing at 0.2 bar. Since the average positron lifetime determines the magnitude of the positron trapping rate and thus the concentration of the vacancy-like defects, the pressure dependence of τ_{av} reflects an inverse relation between the concentration of the vacancy defects at 1100 °C and the arsenic vapor pressure. The upper part in Fig. 5.9 presents the defect-related lifetime obtained from the two-component decomposition of the spectra as a function of the measurement temperature. The defect-related lifetime for all the samples at 300 K is 293 ± 10 ps, what is distinctly higher than the lifetimes in Te- and Si-doped GaAs (254 and 262 ps respectively) where Ga vacancies were found to be responsible for the positron trapping. But this value still lies in the region for a monovacancy, because the value calculated for the $V_{Ga}-V_{As}$ divacancy defect in GaAs is 332 ps [101]. From the defect-related lifetime alone one cannot determine unambiguously to which sublattice the detected vacancy belongs to. However, this question can be answered by the help of simple thermodynamic considerations.

Taking into account the basic thermodynamic reactions for the vacancy formation in GaAs as:



for Ga Vacancy and



for As vacancy. The arsenic tetramer was chosen because it is the dominating As vapor component [37]. Thus, the concentrations of the Ga and As vacancies at a certain temperature should depend on the arsenic vapor pressure. According to the mass action law, the concentrations of these defects can be derived as:

$$[V_{Ga}] = K_{V_{Ga}} \times P_{As}^{1/4}, \quad (5.3)$$

$$[V_{As}] = K_{V_{As}} \times P_{As}^{-1/4}, \quad (5.4)$$

where $K_{V_{Ga}}$ and $K_{V_{As}}$ are mass action constants for gallium and arsenic vacancies at a certain temperature and P_{As} is the ambient arsenic vapor pressure. From Eqs. (5.3 and 5.4), it is clear that the concentrations of V_{Ga} and V_{As} should have an opposite behavior with respect to As vapor

pressure and the V_{As} concentration is inversely proportional to the arsenic vapor pressure, what provides the possibility to discriminate between these two vacancies in both sublattices.

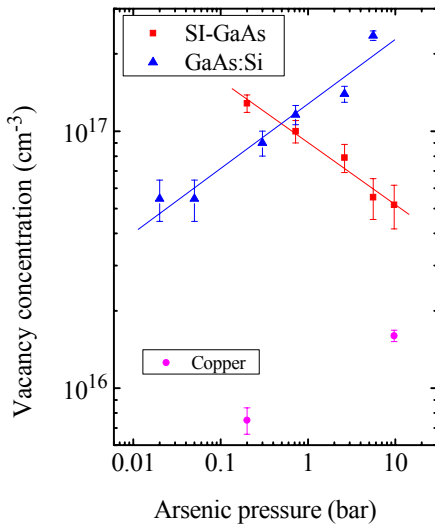


Fig. 5.10: Vacancy defect concentrations in semi-insulating and Si-doped GaAs versus As vapor pressure during annealing at 1100 °C (Ref. [134]). Solid lines are the power law fits to the data points. Closed circles present the concentration of Cu impurities obtained with the help of titration measurements for the samples annealed at 0.2 and 9.68 bar.

Figure 5.10 reveals an opposite behavior of the concentrations of the vacancy-like defects with increasing P_{As} . Compared to the data for n -type Si-doped GaAs ($[Si] = 2 \times 10^{19} \text{ cm}^{-3}$) [134]. The two-component trapping model and the specific trapping coefficient of 10^{15} s^{-1} at 300 K were used for calculating the vacancy concentrations. The fits to the experimental data (solid lines in Fig. 5.10) represent the power law and yield an exponent close to 0.25 for GaAs:Si and -0.25 for SI GaAs. As shown, for the GaAs:Si the vacancy concentration increases with increasing arsenic pressure, what refers to the Ga vacancy and is in accordance with the well-known formation of the $V_{Ga}-Si_{Ga}$ defect complex in this material [96]. The same pressure dependence was also found in Te-doped GaAs [135]. The vacancy concentration in SI GaAs exhibits an opposite behavior and decreases with increasing arsenic pressures, what is characteristic for the V_{As} . Based on these results, the origin of observed vacancy-like defects in annealed semi-insulating GaAs is ascribed to V_{As} . On the other hand, it cannot be the isolated As vacancy. Arsenic vacancies should be positive (and thus not detectable with positrons) in semi-insulating or in p -type GaAs, where the position of Fermi level is in the middle or in the lower part of the band gap. The Hall-effect measurements showed that all investigated annealed samples became slightly p -type with a concentration of $[p] = 10^{11}-10^{12} \text{ cm}^{-3}$ that corresponds to the position of Fermi level at 0.4-0.5 eV above the valence band. Also all theoretical calculations agree that the arsenic vacancy is always positive in SI or p -type GaAs and thus it should be invisible for positrons [79]. These results suggest the existence of a V_{As} defect complex which is not any more positively charged. Since Cu is the most common impurity in annealing studies [128,136,137], Cu is the first candidate that can be responsible for the formation of such a complex.

The concentration of the Cu impurities for the two samples annealed at 0.2 and 9.68 bar was determined by titration measurements (full magenta circles in Fig. 5.10). As can be seen, the Cu concentration was about 10^{16} cm^{-3} only; that is one order of magnitude lower than the measured number of the vacancy-complex. This means that copper is not a constituent of the observed defect complex. Another possibility to check whether the vacancy is neighbored by Cu atoms is to perform coincidence Doppler broadening spectroscopy. The most important parameter which is sensitive to the chemical surrounding of the annihilation site is the form of the high-momentum distribution. Copper being incorporated on the gallium sublattice is a nearest neighbor to arsenic vacancies and thus should be perfectly seen at the high-momentum part of a CDBS spectrum.

Figure 5.11 shows the results of Doppler broadening measurements normalized to an undoped SI GaAs reference sample showing no positron trapping. In the upper part of the figure the ratio curve of annihilation momentum distribution obtained in pure copper is shown. In the lower part, two samples are compared, SI GaAs after copper in-diffusion and SI GaAs annealed at 1100 °C under $P_{As} = 0.2$ bar.

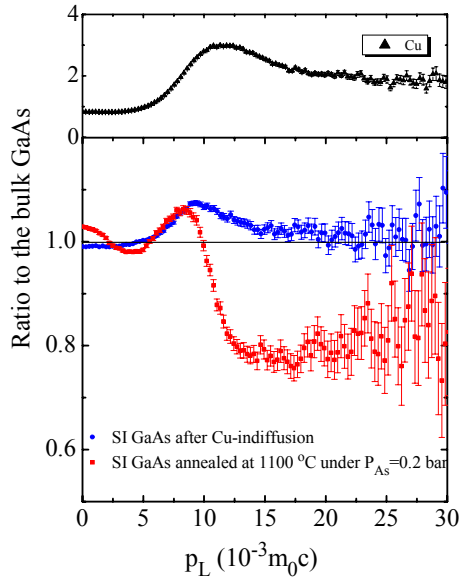


Fig. 5.11: Normalized annihilation momentum distribution measured at room temperature in pure Cu (upper panel) and SI GaAs after Cu in-diffusion and SI GaAs annealed at 1100 °C under $P_{As} = 0.2$ bar (lower panel).

In case of positron annihilation with copper core electrons, the intensity in the high momentum region of the Doppler peak at $(10-20) \times 10^{-3} m_0c$, is higher than in bulk GaAs [ratio is larger than 1, upper part of Fig. 5.11]. Thus, the presence of Cu atoms in the immediate vicinity of a positron trap can be seen as such characteristic increase of the intensity of the electron momentum distribution like it was observed for SI GaAs after Cu in-diffusion. In contrast, in SI GaAs annealed at $P_{As} = 0.2$ bar, no sign of Cu in the neighborhood of detected vacancies was observed. Hence the results of the high momentum part of annihilation momentum distribution for the Cu-diffused GaAs is determined by the annihilation of positrons with the electrons of Cu atoms [131,138], and strongly differs from annealed SI GaAs provided additional support for the assumption that copper is not responsible for the observed vacancy-like defect complex in annealed SI GaAs. The observed V_{As} -like defect should be related to a native defect-complex. The exact nature of this complex cannot be determined from the results of positron annihilation alone. More likely, the electrically active part of Cu impurities acts as shallow positron traps. It causes the decrease of average positron lifetime in the low temperature region. Indeed, the temperature-dependent Hall-effect measurements has revealed the presence of an acceptor level at $E_V + 0.5$ eV that is usually attributed to Cu_{Ga} related defects [136,137].

Figure 5.12 represents the average positron lifetime versus measurement temperature after different annealing steps performed on a Cu-diffused sample, where the Cu diffusion was carried out under 5.57 bar of As vapor pressure. The behavior of the curves is similar to those observed above. A noticeable decrease of the average lifetime in the low temperature region is clearly shown for all curves. Cu acceptor, as shallow traps, is responsible for such decreasing. During annealing up to 750 K, the average positron lifetime increases strongly up to the value of 260 ps, signifying the presence of vacancy-type defects. With a further increase of the annealing temperature, a rapid decrease of the average positron lifetime was observed. With annealing at temperatures higher than 800 K the vacancy clusters grow and the distance between them becomes larger than the positron diffusion length. As a result, they cannot be observed by positrons [131].

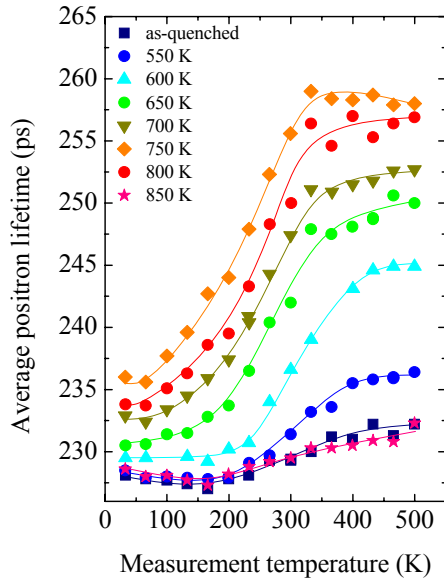


Fig. 5.12: Average positron lifetime as a function of sample temperature in undoped SI GaAs. Prior to the experiment, about 6×10^{18} Cu atoms were introduced by evaporating a layer of 30 nm Cu onto the sample surface and by subsequent annealing at 1100 °C under 5.57 bar of As pressure (3h, then quenched into water). The temperature-dependent lifetime experiment was carried out after each annealing step as illustrated in the figure.

Figure 5.13 shows the annealing behavior of the average and defect-related lifetimes and its intensity. It can be shown that the open volume of the detected vacancy-type defect increases during annealing. The defect-related lifetime increases with increasing the annealing temperature but lies in the monovacancy region until the annealing temperature of 750 K. The defect-related lifetime reaches the value of 332 ps at 800K but with low intensity what corresponds to divacancies (upper panel of figure 5.14).

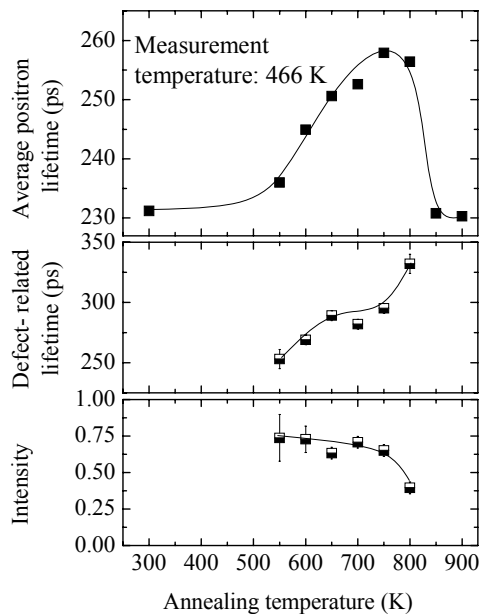


Fig. 5.13: Positron lifetime results of the annealing experiment of undoped semi-insulating GaAs after in-diffusion of $6 \times 10^{18} \text{ cm}^3$ Cu atoms at 1100 °C under 5.57 bar of As pressure. The average lifetime is shown in the upper panel. The defect-related lifetime and its intensity versus the annealing temperature are plotted in the lower two panels. The spectra were measured at a sample temperature of 466 K to diminish the influence of the shallow traps.

The lower panel of Fig. 5.14 represents the defect concentration versus the annealing temperature where the defect concentration increases from $6.97 \times 10^{16} \text{ cm}^{-3}$ at 550 K up to $1.49 \times 10^{17} \text{ cm}^{-3}$ at 750 K and decreases again at 800 K. The defect concentration is determined according to Eq. (3.17). The upper panel in Fig. 5.14 represents the number of vacancies versus the annealing temperature where the number of vacancies is one vacancy in the temperature range up to 750 K and increase to be 2 vacancies at 800 K. This was estimated according to the calculation in Ref. [133].

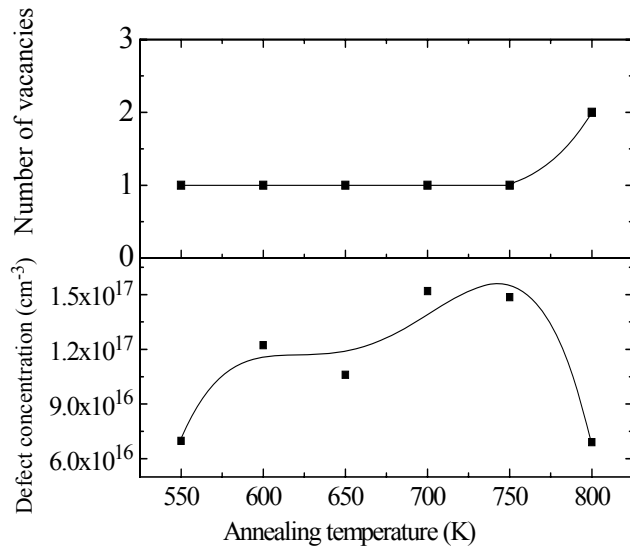


Fig. 5.14: Defect concentration and the number of vacancies as a function of the annealing temperature in undoped SI GaAs after in-diffusion of $6 \times 10^{18} \text{ cm}^{-3}$ Cu atoms at $1100 \text{ }^\circ\text{C}$ under 5.57 bar of As pressure. The number of vacancies in the observed clusters is shown in the upper panel. The defect concentration versus the annealing temperature is plotted in the lower panel. These Data were calculated using the positron lifetime results presented in Fig. 5.13.

A sample was annealed under similar conditions but without Cu treatment. The results are shown in figure 5.15. The as-quenched sample shows a higher value of the average lifetime. This can be attributed to the trapping of positrons in vacancies. The pronounced decrease of the average positron lifetime at temperatures below 200 K may be explained by positron trapping at negative ions (shallow traps), C_{As}^- . Where semi-insulating high resistive crystals are produced by intentional doping of GaAs with carbon atoms, which are incorporated exclusively on the As sublattice forming shallow acceptor-like defects, C_{As} [34]. But this cannot be identified from the results of positron lifetime alone. With increasing the annealing temperature the average lifetime decreases. This is owing to the fact that the vacancies vanish. On the contrary, in case of GaAs samples after Cu in-diffusion under 5.57 bar (figure 5.12), the as-quenched sample did not show an observable change in the average positron lifetime. However, during the annealing steps until 750 K the average positron lifetime increases strongly, and at annealing temperatures higher than 800 K the vacancy cluster signal almost vanish.

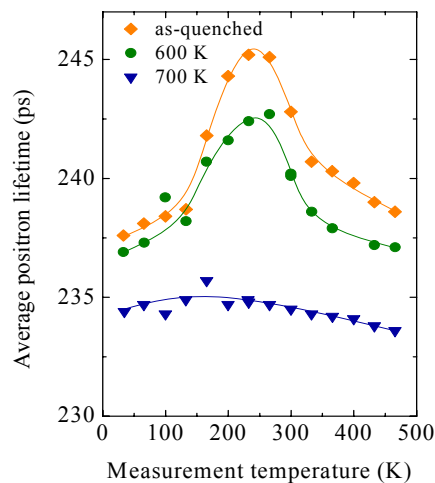


Fig. 5.15: Average positron lifetime as a function of sample temperature in undoped SI GaAs. The samples were annealed at $1100 \text{ }^\circ\text{C}$ under 5.57 bar of As pressure. The samples were not treated with copper as a reference experiment to the results shown in figure 5.12. The temperature-dependent lifetime experiment was carried out after each annealing step as shown in the figure.

5.3.3 Zinc-doped GaAs

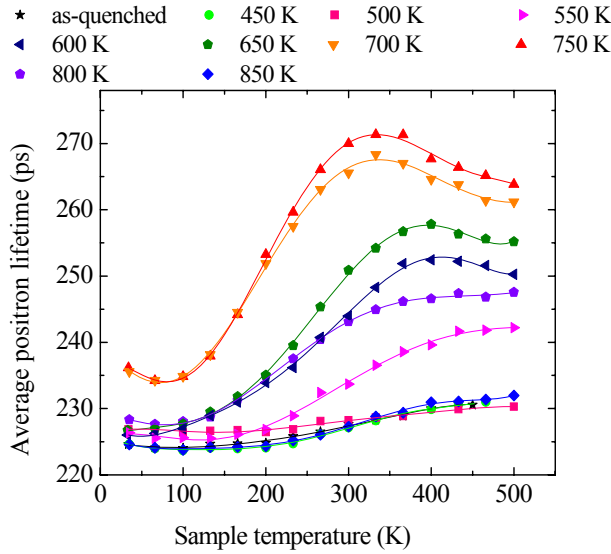


Fig. 5.16: Average positron lifetime as a function of sample temperature in GaAs:Zn. Prior to the experiment, a layer of 30 nm Cu was deposited onto the sample surface and introduced by subsequent annealing at 1100 °C under 0.2 bar of As pressure. The temperature-dependent lifetime experiment was carried out after each annealing step as displayed in the figure.

Positrons annihilate in the GaAs:Zn ($[Zn]=3.8 \times 10^{16} \text{ cm}^{-3}$) sample without any Cu deposition (reference sample) from the defect-free state. After Cu in-diffusion, the average lifetime increases only slightly in the high-temperature region, what illustrates that a small number of vacancy-type defects is detected. The average positron lifetime versus measurement temperature after different annealing steps performed after Cu in-diffusion is shown in figure 5.16. An obvious decrease of the average lifetime at low temperatures is clearly shown for all curves. This is a direct sign for detection shallow positron traps (negative ions). After Cu in-diffusion, the shallow traps can be only ionized Cu acceptor. Upon annealing up to 750 K, the average positron lifetime increases strongly up to the value of 272 ps, reflecting the existence of vacancy-like defects. With a further increase of the annealing temperature, a rapid decrease of the average positron lifetime is monitored. Upon annealing at temperatures higher than 800 K the vacancy clusters grow and the distance between them becomes larger than the positron diffusion length. Thus, they become invisible for positrons [131].

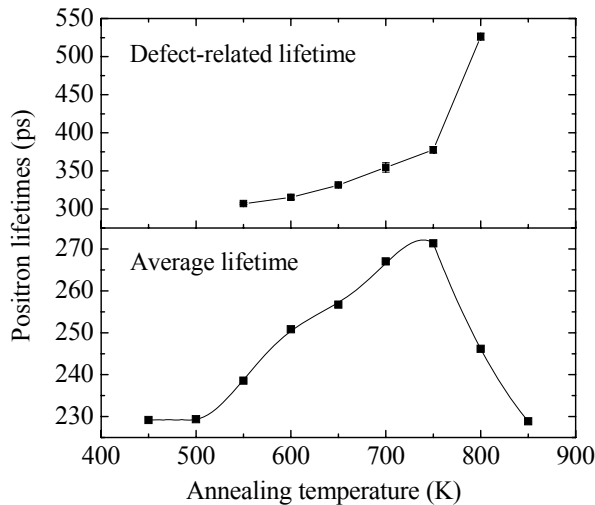


Fig. 5.17: Lifetime results of the annealing experiment of Zn doped GaAs after Cu in-diffusion at 1100 °C under 0.2 bar of As pressure. The average lifetime is shown in the lower panel. The defect-related lifetime versus the annealing temperature is plotted in the upper panel. The spectra were measured at a sample temperature of 466 K to diminish the influence of the shallow traps.

Figure 5.17 represents the behavior of the average and defect-related lifetimes as a function of the annealing temperature. This sample shows only two lifetime components, where three lifetime components were obtained in Cu-diffused SI GaAs samples. As clearly shown in the figure, the increase of τ_d is indicative of the increase of the open volume of the observed vacancy-type defects. At annealing temperature of 550 K τ_d is larger than that of the monovacancy but still lies in the monovacancy region. At 600 K it corresponds to a divacancy. With further increasing of the annealing temperature, τ_d increases to reach 526 ps at 800 K. This higher value of the defect-related lifetime can be only explained by trapping of positron at vacancy clusters. It is corresponding to vacancy clusters of more than 10 vacancies [133].

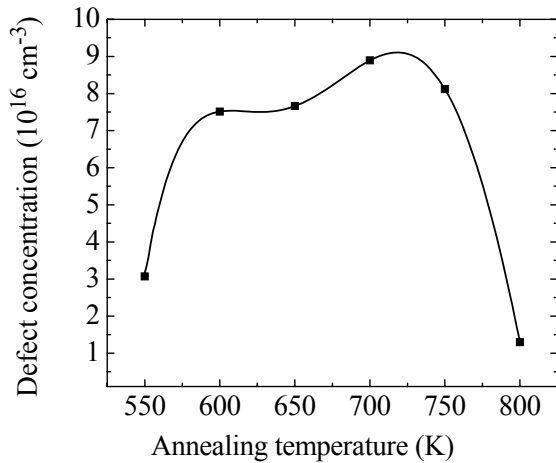


Fig. 5.18: Defect concentration versus the annealing temperature in GaAs:Zn ($3.8 \times 10^{16} \text{ cm}^{-3}$) after in-diffusion of $6 \times 10^{18} \text{ cm}^{-3}$ Cu atoms at 1100 °C under 0.2 bar of As pressure. The data were calculated according the positron lifetime results in Fig. 5.16.

Fig. 5.18 represents the defect concentration as a function of the annealing temperature in Cu-diffused GaAs:Zn where the defect concentration increases from $3 \times 10^{16} \text{ cm}^{-3}$ at 550 K up to $9 \times 10^{16} \text{ cm}^{-3}$ at 700 K then decreases. The defect concentration is estimated using Eq. (3.17).

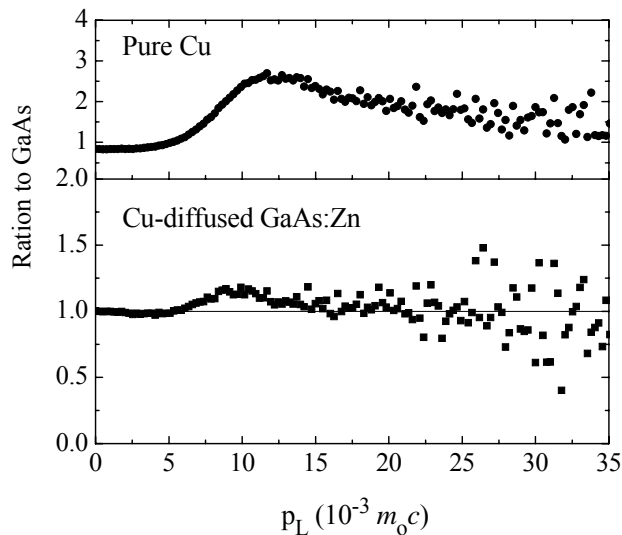


Fig. 5.19: Normalized annihilation momentum distribution measured at room temperature in pure Cu (upper panel) and Cu-diffused GaAs:Zn (lower panel). Cu in-diffusion was performed by annealing the sample at 1100 °C under $P_{As} = 0.2$ bar. The sample was subject to an isochronal annealing up to 750 K, which shows a maximum effect on the lifetime.

Figure 5.19 shows the results of CDBS measurements normalized to an undoped SI GaAs reference sample showing no positron trapping. In the upper panel of the figure the ratio curve of annihilation momentum distribution obtained in pure copper is displayed. In the lower panel, Zn-doped GaAs ($[Zn]=3.8 \times 10^{16} \text{ cm}^{-3}$) after copper in-diffusion at 1100 °C and $P_{As} = 0.2$ bar. The sample was subject to an isochronal annealing up to 750 K then measured by CDBS. As mentioned above, the existence of Cu atoms in the direct neighborhood of a positron trap can be observed as

such characteristic increase of the intensity of the electron momentum distribution. This is obviously monitored in the Cu-diffused GaAs:Zn sample, where the ratio curve is higher than 1 (lower part of Fig. 5.19). Hence, CDBS results support the assumption that copper is responsible for the observed vacancy-like defect complex in Cu-diffused GaAs:Zn annealed under 0.2 bar. The observed defect is most likely $V_{As}-Cu_{Ga}$ complex. The theoretical calculations support this assumption, which predict the presence of one Cu atom in the near vicinity of arsenic vacancy $V_{As}-1Cu_{Ga}$ (Fig. 6.12).

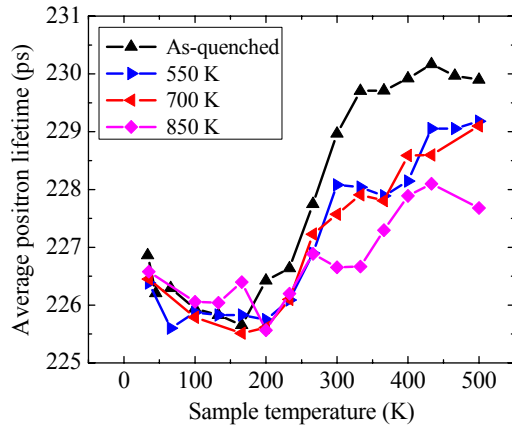


Fig. 5.20: Average positron lifetime versus sample temperature in Zn doped GaAs. The samples were annealed at 1100 °C under 0.2 bar of As pressure without Cu treatment. The temperature-dependent lifetime experiment was performed after different annealing steps.

To show that the observed vacancy-like defects are Cu-related, a GaAs:Zn sample was annealed under the similar conditions but without Cu treatment. The obtained lifetime results of this sample are displayed in figure 5.20. As shown in the figure and independently of annealing, the as-quenched sample shows an average lifetime close to that of the reference sample. It shows an average lifetime of 230 ps at 300 K. The decrease of average lifetime in the low temperature region is ascribed to trapping of positron to shallow traps. Impurities in the sample act most likely as shallow traps. With increasing the annealing temperature the average lifetime in the temperature range $T > 300$ K decreases. This is owing to disappearance of vacancies which are probably created during annealing of the sample at 1100 °C. The average lifetime changes within only 2 ps, which indicates the presence of very low density of defects, whereas in Cu diffused GaAs:Zn an increase of 45 ps in the average lifetime is observed. This behavior stands in obvious contrast to data of Cu-diffused GaAs:Zn samples.

5.3.4 Estimation of the positron binding energy to shallow traps

In order to determine the positron binding energy, the three-state trapping model is used. This model comprise positron annihilation in the free state, trapping to vacancy-like defects with κ_v and trapping to shallow traps with κ_{st} and detrapping from shallow traps with δ . The positron detrapping transition is formulated experimentally by the solution of the kinetic trapping equation [139].

$$\frac{\delta}{\kappa_{st}} = \left[\frac{I_2}{I_1 \kappa_v - I_2 (\lambda_b - \lambda_2)} - \frac{1}{\kappa_{st}} \right] (\lambda_{st} - \lambda_2). \quad (5.5)$$

Where $\tau_2 = \lambda_2^{-1}$ is the lifetime of the longest component in the lifetime spectra which has the intensity I_2 . $\lambda_b = \tau_b^{-1} = (228 \text{ ps})^{-1}$ is the annihilation rate in the bulk crystal. $\lambda_{st} = \tau_{st}^{-1} = (224 \text{ ps})^{-1}$ is assumed, which is the lowest value given by the as-quenched sample in the low temperature region. The value of κ_v is evaluated at high temperature, $T > 300$ K, where the effect of shallow traps is

vanished. κ_{st} is estimated at very low temperature, close to 0 K, where the thermal detrapping can be neglected. Eq. (5.5) illustrates that the detrapping rate is totally governed by the intensity of the vacancy component I_2 .

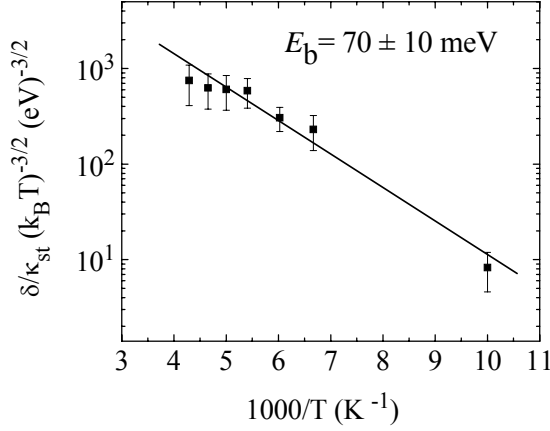


Fig. 5.21: The ratio of the detrapping and trapping rates in Cu diffused GaAs:Zn annealed under 0.2 bar of P_{As} calculated from the decomposition of the lifetime spectra after annealing the sample at 750 K using Eq. (5.5). The solid line is the fit of Eq. (5.6) to the experimental data with $E_b = 70$ meV.

A thermodynamic approach to calculate the positron detrapping from defects gives the ratio of the detrapping to trapping rates as [90]:

$$\frac{\delta}{\kappa_{st}} = \frac{1}{C_{st}} \left[\frac{m^*}{2\pi\hbar} \right]^{3/2} (k_B T)^{3/2} \exp \left[\frac{E_b}{k_B T} \right], \quad (5.6)$$

where E_b is the positron binding energy to the shallow traps with the concentration C_{st} . Figure 5.21 demonstrates the Arrhenius plot of the measured detrapping rates from Eq. (5.5) in Cu-diffused GaAs:Zn annealed under 0.2 bar of P_{As} determined from decomposition of positron annihilation lifetime spectra measured after annealing at 750 K. The solid line in Fig. 5.21 represents the fit of Eq. (5.6) to the experimental data. The slope yields a binding energy of 70 ± 10 meV. All the lifetime spectra measured after annealing the sample at 650 K show two-component decomposition. But the decomposition below 100 K is not so reliable; therefore a 255-ps component is fixed to diminish the statistical uncertainties of the fitting. Positron binding energy in the first Rydberg state is calculated theoretically to be 81.7 meV [88]. The value determined experimentally is close to the calculated one. Thus, most likely positrons are detrapped from the first Rydberg state. Shallow trap concentration is roughly estimated to be $5 \times 10^{16} \text{ cm}^{-3}$.

5.4 Summary

The formation of point defects in undoped semi-insulating and Zn-doped GaAs samples during the diffusion of copper was investigated by positron annihilation lifetime and Doppler spectroscopy. The experiment findings can be summarized as follows:

- 1) Almost no positron trapping is found after quenching from diffusion temperature (1100 °C), when Cu is disturbed all over the crystal, i.e. after in-diffusion. During a subsequent annealing up to 750 K after the diffusion treatment (out-diffusion), the average positron lifetime increases strongly indicating the generation of vacancy-type defects. With a further increase of the annealing temperature to 850 K, a rapid decrease of the average positron lifetime was observed. It is due to the fact that vacancy clusters grow and the distance between them becomes larger than the positron diffusion length.
- 2) It can be shown from the annealing behavior of the average lifetime of the Cu-diffused GaAs samples that the open volume of the detected vacancy-like defect increases during

annealing, in contrast to the GaAs samples annealed under very similar conditions but not treated with Cu. The average lifetime decreases with increasing the annealing temperature.

- 3) The defect concentration increases with increasing the annealing temperature up to 700 K. The number of vacancies incorporated in the observed clusters in the Cu-diffused GaAs samples annealed under 0.2 bar of P_{As} is found to increase with increasing the annealing temperature and reaches 4 vacancies at 700 K. The size of the vacancy clusters at 750 K increases to become microvoids. On the hand, the Cu-diffused SI GaAs samples annealed under 5.57 bar of P_{As} showed a defect-related lifetime which corresponds to monovacancies up to 750 K annealing temperature and divacancies only at 800 K.
- 4) Vacancy-like defects and shallow positron traps (negatively charged non-open volume defects, such as ionized acceptors) were observed.
- 5) On the basis of positron annihilation parameters and thermodynamic considerations, it was concluded that the observed vacancy-like defect contains an arsenic monovacancy. The results obtained at undoped SI GaAs were compared to the results of similar experiments done on *n*-type Si-doped GaAs to confirm the reliability of such thermodynamic considerations, where the existence of donor-gallium vacancy complex is well known.
- 6) The difference of the arsenic vapor pressure dependence of the vacancy concentration for undoped SI and *n*-type Si-doped GaAs was clearly shown. Taking into account that the isolated V_{As} in a *p*-type sample is positive and accordingly invisible to positrons, the presence of a vacancy complex containing an As vacancy was assumed. The charge of this complex must be neutral or negative in the *p*-type samples.
- 7) Due to the high solubility and high diffusion coefficient of copper in GaAs, it was the first candidate that could be responsible for this complex. The contamination of Cu atoms in SI GaAs samples was confirmed with means of titration measurements but the concentration was almost one order of magnitude lower than the vacancy concentration that was calculated from positron lifetime measurements.
- 8) Doppler broadening coincidence measurements performed on Cu-diffused SI GaAs samples indicated the absence of the copper in the vicinity of the As vacancy. Thus, it can be hypothesized that the observed vacancy complex is not bound to Cu impurities and represents a native defect complex. But the structure of the complex cannot be exactly determined from positron annihilation parameters alone.
- 9) CDBS measurements carried out on the Cu-diffused GaAs:Zn samples illustrated the presence of Cu in the neighborhood of the As vacancy. The observed defect in these samples is more probably a V_{As} - Cu_{Ga} complex.
- 10) The positron binding energy to the shallow traps is estimated in Cu-diffused GaAs:Zn samples to be 70 meV.
- 11) The observed shallow traps can be explained by copper contamination. Cu atom placed on a Ga sublattice forms a double acceptor Cu_{Ga}^{2-} (energy level $E_V + 0.5$ eV) that acts as a positron shallow trap.
- 12) The temperature-dependence Hall-effect measurements confirmed the existence of this acceptor level.

6. Identification of defect properties in Te-doped GaAs after Cu in-diffusion by positron annihilation

This chapter contains the results of an extensive systematic positron annihilation spectroscopy study of defects introduced by Cu diffusion in Te-doped GaAs grown by liquid-encapsulated Czochralski technique. The discussion in this chapter is concentrated on the identification of the defects introduced during Cu-out diffusion by both experimental and theoretical PAS results. PALS results were used to estimate the shallow traps concentration by applying the trapping model and the binding energy of positrons considering thermodynamic approximations.

6.1 Introduction

Point defects play a major role on the important properties of semiconductor materials such as GaAs. They reduce the density of free carriers [140,141] or mediate, e.g., dopant diffusion [40]. The detailed microscopic identification of vacancies and vacancy complexes in GaAs was found to be difficult. The theoretical calculations [37,142,143] in addition to diffusion studies [40] indicate a predominant role of negative Ga vacancies (V_{Ga}) in *n*-doped GaAs. In contrast, a recent calculation showed that also the As vacancy (V_{As}) could be an abundant defect in highly *n*-doped GaAs because of the low value of formation energy [144]. Furthermore, acceptor-like vacancies with positive donor complexes also are expected owing to Coulomb attraction. Evidence for such complexes is given by photoluminescence [145], infrared absorption [140], and theoretical considerations of the doping behavior [141]. Si_{Ga} -donor- V_{Ga} complexes on cleavage planes of highly Si-doped GaAs were identified by scanning tunneling microscopy (STM) [146]. But for other *n* dopants, e.g., tellurium, no such direct identification has been obtained so far. Positron annihilation spectroscopy (PAS) has extensively served as a non-destructive probe for open-volume defects in semiconductors [79]. Open-volume defects (e.g. vacancy-like defects) act as attractive and deep trapping centers for positrons. Positrons trapped in an open-volume defect are accompanied with subsequent changes in their specific annihilation parameters [147]. Because of the reduced electron density in these defects, the trapped positrons have longer lifetimes and a narrower momentum distribution [147,148]. PAS application to semiconductors has successfully led to reliable information on vacancy-related defects such as their concentration, their energy levels, or charge states [76,149,150,151]. PAS studies showed the existence of native vacancies in *n*-doped GaAs [152,153]. However, the positron lifetime measurement alone is not able to identify the defects as a given isolated gallium [154] or arsenic [152] vacancy, or as a vacancy-impurity complex [153]. One possibility to overcome this difficulty is the performance of positron annihilation momentum distribution. The chemical surrounding of the annihilation site can be identified using the high momentum part of this distribution [98,99,100,101,108]. This is based on the fact that tightly bound core electrons with high momenta retain their element-specific properties. This permits the identification of vacancies and vacancy-impurity complexes, in particular when measurements are compared to theoretical calculations of the momentum distribution [98].

When the positron binding energy to the defects is very small ($\ll 1\text{eV}$), subsequently, the positron wave function is weakly localized. These defects are identified as shallow positron traps [88]. The positron annihilation parameters in shallow traps are practically very close to those in defect-free bulk. Due to the weak binding energy, positrons are effectively trapped only at low temperatures. At higher temperatures they are thermally detrapped. Impurities in semiconductors

lead to the formation of shallow levels for electron and holes in the forbidden gap. The long-range Coulomb field around the negative impurities may bind positrons to Rydberg-like states. Their binding energies could be determined by the positron effective mass. In metals, dislocation lines [155-157] and grain boundaries [158] have been suggested to act as shallow traps. It has been observed that the A center in Si [79] shows a typical behavior of shallow traps. Some of the difficulties which have been observed in positron annihilation studies in semiconductors could be explained by shallow traps [159-162]. Positron annihilation was used to study the defects in semi-insulating (SI) GaAs after Cu in-diffusion. It was found that Cu atoms form double acceptors $\text{Cu}_{\text{Ga}}^{2-}$ which act as a positron shallow trap [93].

The coincident detection of both 511 keV gamma quanta from single annihilation events reduces the disturbing background and hence permits the observation of the high-momentum annihilation distribution [98,99,100,108]. Ga vacancies in Si-doped GaAs were observed using coincidence Doppler-broadening spectroscopy (CDBS) [163]. However, the experiment could not determine whether the vacancies are isolated or forming a complex. That is because of the expected low contribution of Si_{Ga} donor on the second adjacent site to the annihilation [163]. Consequently, the identification of the impurity-vacancy complexes in GaAs using positron annihilation is still an open question. It is well known that tellurium is incorporated into the As sublattice only [141]. If coupling with nearest Ga vacancies happens, a detectable contribution to the annihilation is expected. Then, this complex, most likely, can be identified. Nevertheless, the momentum distribution for the vacancy cannot be unquestionably determined, especially, when the fraction of trapped positrons (η) is unknown. Thus, correlated positron lifetime measurements can be used to obtain η [105]. The experimental results are compared with theoretical calculations of the annihilation characteristics to get a reliable interpretation. Cu may be introduced during crystal growth or subsequent processing steps [164]. Cu diffuses in GaAs very fast by interstitial diffusion (kick-out process) [165]. In GaAs, Cu has two levels in the band gap and thus a significant influence on electronic properties. Depending on the cooling speed after a diffusion process, the concentration of electrically active Cu atoms is much lower than the total concentration incorporated [128,166]. This is because of the low solubility of Cu in GaAs at room temperature which is about $1 \times 10^{16} \text{ cm}^{-3}$ [165]. After Cu in-diffusion in SI GaAs, vacancy complexes containing an As vacancy were observed. CDBS showed that Cu is not bound to the observed vacancy complex [93]. Cu in-diffusion in the investigated samples was performed upon annealing the samples at 1100 °C under different As pressure, where the samples were covered with a thin layer of Cu. These Cu pre-introduced samples were subjected to isochronal annealing in ambient containing no Cu source which leads to Cu out-diffusion. The positron lifetime results give evidence that below 300 K positrons are trapped to open-volume defects (vacancies) as well as at shallow traps with no open volume. The shallow traps are believed to be Cu acceptors. The concentration of shallow traps is determined and found to be in a good agreement with the acceptor concentration found by Hall measurements. Positron localization in Rydberg states around the negative double acceptor Cu in Cu diffused samples is suggested to be responsible for the origin of shallow traps. The presence of shallow traps in n -type GaAs was observed earlier [88]. Their origin was suggested to be negative acceptor like centers, which are residual impurities or native defects [88]. As it will be shown that Cu out-diffusion depends on the in-diffusion conditions, especially on the arsenic vapor pressure during Cu in-diffusion.

The chapter is organized as follows: in the next section the details of the experimental work are given. Positron lifetime and coincidence Doppler broadening results are presented in sections 6.3 and 6.4 respectively. In section 6.5 the concentration of shallow traps and positron binding energy at them are determined. Section 6.6 concludes the chapter.

6.2 Experimental work

The samples investigated were cut from Te-doped GaAs crystals grown by the liquid encapsulated Czochralski technique (LEC) ($5 \times 5 \times 0.55 \text{ mm}^3$). The carrier concentration was $n = 3.5 \times 10^{17} \text{ cm}^{-3}$. The samples were covered at one side by 35 nm Cu by evaporating it under UHV conditions. The samples and the arsenic source were sealed in quartz ampoules under high vacuum. Annealing was performed for 3 h at 1100 °C (sample temperature). The temperature of the arsenic source was 550 and 740 °C. The annealing time was chosen in such a way that a homogeneous Cu concentration was established in the whole sample. This was calculated according to the diffusion coefficient of Cu in GaAs at 1100 °C [17]

$$D = 0.03 \text{ cm}^2 \text{ s}^{-1} \exp\left(\frac{-0.53 \text{ eV}}{k_B T}\right), \quad (6.1)$$

The annealing conditions were chosen to maintain arsenic-rich stoichiometry. Hall-effect measurements were applied to measure the samples in the as-quenched state. Thereafter, the samples were isochronally annealed in the temperature range up to 900 K. Between the annealing steps, temperature dependent positron lifetime measurements in the temperature range of 29–500 K were carried out using a conventional fast-fast coincidence system with a time resolution of 220 ps. After source and background corrections, the lifetime spectra were analyzed with one, two or three exponential components,

$$n(t) = \frac{I_1}{\tau_1} e^{-\lambda_1 t} + \frac{I_2}{\tau_2} e^{-\lambda_2 t} + \frac{I_3}{\tau_3} e^{-\lambda_3 t}, \quad (6.2)$$

convoluted with the Gaussian resolution function of the spectrometer. In Eq. (6.2), the annihilation rate, λ_i , is the inverse of positron lifetime ($\lambda_i = \tau_i^{-1}$). I_i is the relative intensity of the lifetime component τ_i in the spectrum. The average positron lifetime is calculated from the experimental lifetimes and their intensities according to Eq. (3.16).

The spectra were analyzed using the LT9 program [86,87]. The annihilation momentum distribution was observed by coincidence spectroscopy measured at 466 K using two Ge- γ -detectors in collinear geometry [99,108]. The Ge- γ -detectors have both an energy resolution of 1.4 keV at 514 keV of ^{85}Sr .

6.3 Positron lifetime results

6.3.1 Sample annealed under 10 bar of P_{As}

In a defect-free crystal, positrons annihilate with a single lifetime τ_b , which it has found to be 228 ps in SI GaAs [109,110,167]. After Cu in-diffusion at 1100 °C under 10 bar of arsenic vapor pressure, the as-quenched sample showed a decrease of the average lifetime in the low-temperature region ($T < 100 \text{ K}$) and a saturation level of the average lifetime at 220 ps which is distinctly lower than the value measured in the bulk SI GaAs (228 ps). That indicates a detection of non-open volume defects, shallow traps, which tend to trap positrons, reflecting thereby properties very close to the bulk annihilation characteristics of the positrons [79,88,93]. Then, positrons trapped into shallow traps have a lifetime $\tau_{\text{st}} = 220 \text{ ps}$ (st denote shallow traps). The behavior of the lifetime as a function of the temperature can then be attributed to thermally assisted positron detrapping from these shallow traps. This is because the high detrapping rate of positron from shallow positron traps at elevated temperatures.

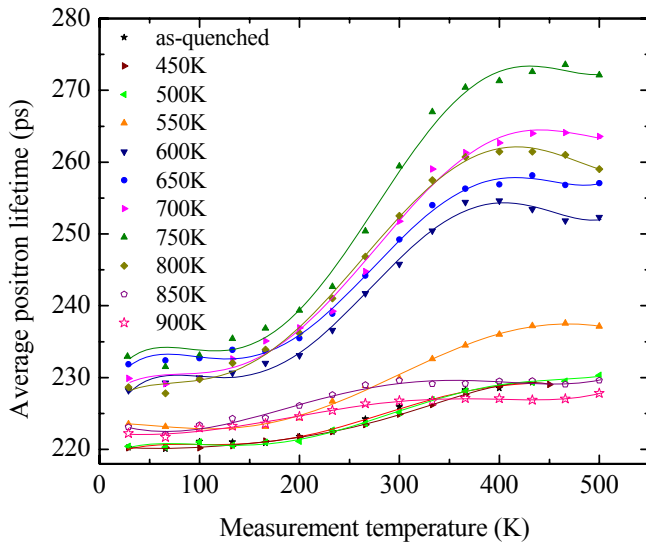


Fig. 6.1: Average positron lifetime as a function of measurement temperature in GaAs:Te. Prior to the experiment, about $6 \times 10^{18} \text{ cm}^{-3}$ Cu atoms were introduced by evaporating a layer of 35 nm Cu onto the sample surface and by subsequent annealing for 3h at 1100 °C under 10 bar of As vapor pressure (then quenched into RT water). The sample is isochronally annealed. The temperature-dependent lifetime experiment was performed after each annealing step as illustrated in the figure.

Figure 6.1 represents the average positron lifetime versus measurement temperature after different annealing steps performed after Cu in-diffusion under 10 bar of As vapor pressure. A distinct decrease in the average lifetime at low temperatures is clearly shown for all curves. All curves show similar temperature behavior. Almost no clear change was observed in the positron lifetime for the annealing steps up to 500 K. Here, after Cu in-diffusion, the shallow traps must be ionized Cu acceptors. Their concentration is up to $2.2 \times 10^{17} \text{ cm}^{-3}$ according to the Hall-effect measurements. It is observed that the samples are converted to *p*-type as shown by Hall-effect. This could be ascribed to the high solubility of Cu in GaAs at 1100 °C. During annealing up to 750 K, the average positron lifetime increases strongly up to the value of 275 ps, indicating the existence of vacancy-like defects. With a further increase in the annealing temperature, a huge decrease in the average positron lifetime was observed. With annealing at temperatures higher than 850 K the vacancy clusters grow and the distance between them becomes larger than the positron diffusion length. Thus, they become invisible for positrons [93,131]. The vacancy clusters may also be dissolved what would lead to a disappearance of the vacancy signal too. These two possibilities cannot be discriminated by the obtained data alone.

Figure 6.2 shows the average lifetime and lifetime components and their relative intensities as a function of the annealing temperature. The spectra were measured at 500 K to diminish the effect of shallow traps. It is shown that the open volume of the detected vacancy-type defect increases during annealing. The defect-related lifetime is much higher than that for monovacancies (250–260 ps) [79]. This can only be explained by trapping of positron at small vacancy clusters. The intensity of the second lifetime component (I_2) increases with increasing annealing temperature. Only the spectrum measured after annealing at 750K shows a three lifetime components decomposition. The defect-related lifetime τ_3 reaches the value of 550 ps corresponding to vacancy clusters with a larger number of vacancies ($N > 15$) but with low intensity I_3 . τ_1 is always less than the bulk lifetime. In presence of open-volume defects, positrons may get trapped and annihilate with more than one component, which are always longer than τ_b in case of open-volume defects.

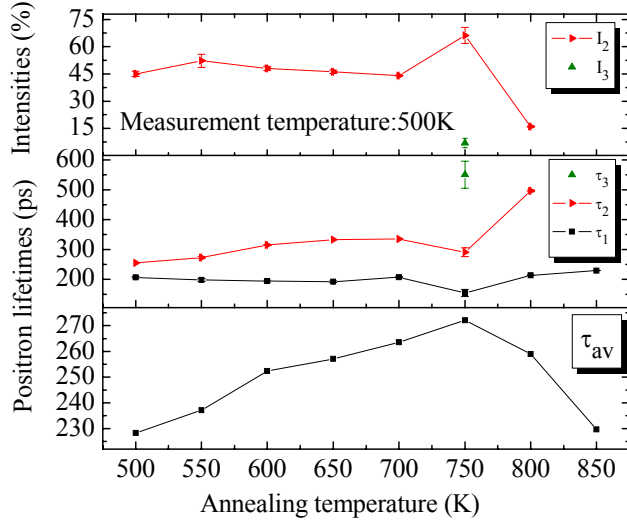


Fig. 6.2: Positron lifetime results of the isochronal annealing experiment of GaAs:Te after in-diffusion of $6 \times 10^{18} \text{ cm}^{-3}$ Cu atoms at $1100 \text{ }^\circ\text{C}$ under 10 bar of As pressure. The average lifetime is shown in the lower panel. The lifetimes and their relative intensities versus the annealing temperature are plotted in the two upper panels. The spectra were measured at a sample temperature of 500 K to avoid the influence of the shallow traps.

The positron trapping rate κ_d is proportional to the defect concentration C_d and is given by Eq. (3.9). For a two-component decomposition, i.e. only one dominating defect type, the trapping rate is given by Eq. (3.17).

In case of two non-interacting deep positron traps, the lifetime spectrum has three exponential decay components. The lifetimes and intensities are given by:

$$\tau_1 = 1/\lambda_1 = \frac{1}{\lambda_b + \kappa_{d1} + \kappa_{d2}}, \quad \tau_2 = 1/\lambda_2, \quad \tau_3 = 1/\lambda_3, \quad (6.3)$$

$$I_1 = 1 - I_2 - I_3, \quad I_2 = \frac{\kappa_{d1}}{\lambda_1 - \lambda_2}, \quad I_3 = \frac{\kappa_{d2}}{\lambda_1 - \lambda_3}. \quad (6.4)$$

It follows for the trapping rates:

$$\kappa_{d1} = I_2(\lambda_1 - \lambda_2), \quad \kappa_{d2} = I_3(\lambda_1 - \lambda_3), \quad (6.5)$$

or more often they are given in the form:

$$\kappa_{d1} = \frac{I_2(\lambda_b - \lambda_2) + I_2 I_3(\lambda_2 - \lambda_3)}{I_1}, \quad \kappa_{d2} = \frac{I_3(\lambda_b - \lambda_3) + I_2 I_3(\lambda_3 - \lambda_2)}{I_1}. \quad (6.6)$$

In that case, the trapping rate is the summation of the trapping rates of both defects as:

$$\kappa_d = \kappa_{d1} + \kappa_{d2}, \quad (6.7)$$

κ_{d1} is the positron trapping rate to the first defect and κ_{d2} is that to the second defect type.

The annihilation fractions (η_i) are also expressed as:

$$\eta_2 = \frac{\kappa_{d1} \tau_b}{1 + \tau_b(\kappa_{d1} + \kappa_{d2})} = \frac{\kappa_{d1}}{\lambda_b + \kappa_{d1} + \kappa_{d2}}, \quad (6.8)$$

$$\eta_3 = \frac{\kappa_{d2} \tau_b}{1 + \tau_b(\kappa_{d1} + \kappa_{d2})} = \frac{\kappa_{d2}}{\lambda_b + \kappa_{d1} + \kappa_{d2}}.$$

Considering that $\eta_1 + \eta_2 + \eta_3 = 1$. The average lifetime is expressed in terms of the annihilation fractions as:

$$\tau_{av} = \eta_1 \tau_b + \sum_{i=2}^k \eta_i \tau_i. \quad (6.9)$$

The solution for the simple case of only one defect type is given by substituting $\kappa_{d2} = 0$. This leads to $\eta_3 = 0$. The lifetimes are given by Eq. (3.12). Their relative intensities are expressed by:

$$I_1 = 1 - I_2, \quad I_2 = \frac{\kappa_{d1}}{\lambda_1 - \lambda_2}. \quad (6.10)$$

Eq. 6.10 is the same as Eq. (3.13), where $\lambda_1 - \lambda_2 = \lambda_b - \lambda_2 + \kappa_{d1}$.

The positron trapping rate is expressed by Eq. (3.15). The annihilation fraction is given by:

$$\eta_2 = \frac{\kappa_{d1} \tau_b}{1 + \tau_b \kappa_{d1}}. \quad (6.11)$$

Because the average lifetime can be experimentally determined with high accuracy, it is often to express the trapping rate in terms of τ_{av} by Eq. (3.17). μ is taken as 10^{15} s^{-1} at 300 K [96,130]. τ_b is the bulk lifetime (228 ps), τ_{av} is the average positron lifetime, calculated from the experimental lifetime components according to Eq. (3.16) and τ_d is the defect-related lifetime.

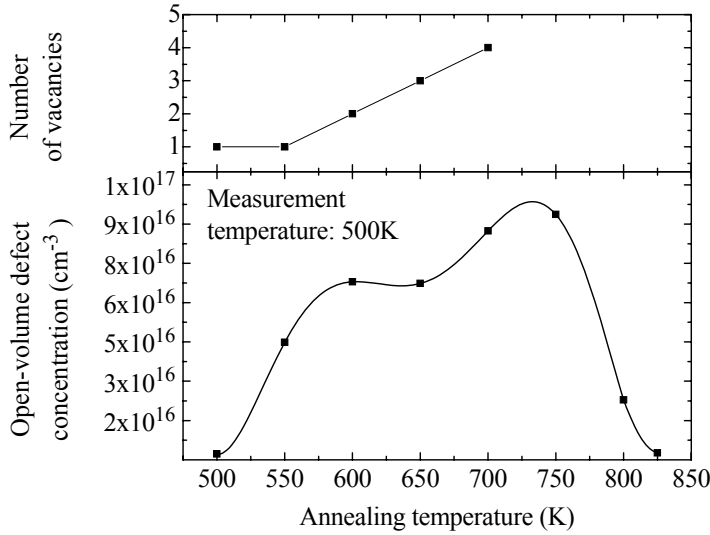


Fig. 6.3: Defect concentration and the number of vacancies (N) included in one cluster versus the annealing temperature in Cu diffused GaAs:Te. The defect concentration versus the annealing temperature is plotted in the lower panel. The number of vacancies in the observed clusters is shown in the upper panel. These data were calculated using the positron lifetime results presented in Fig. 6.2.

The trapping rates are determined using Eqs. (3.17, 6.5) for two and three lifetime components spectra respectively. The defect concentration is calculated by applying Eq. (3.9). The lower panel of Fig. 6.3 represents the defect concentration versus the annealing temperature where the defect concentration increases from $2.2 \times 10^{15} \text{ cm}^{-3}$ at 500 K up to $9.4 \times 10^{16} \text{ cm}^{-3}$ at 750 K. For further annealing temperatures, the defect density decreases due to the decrease of the average positron lifetime.

The number of vacancies in a cluster (N) is estimated from the defect-related lifetime according to the calculation in Ref. [133], which is based on the superimposed-atom model by Puska and Nieminen [80]. As shown in the upper panel of Fig. 6.3, the number of vacancies in a cluster increases from one at annealing temperature of 500 K to four vacancies at 700 K of the annealing temperature. At further annealing temperature, at 750 K the defect related lifetime is 550 ps what corresponds to a cluster of more than 15 vacancies. This value of lifetime is roughly theoretically estimated to a corresponding cluster of ~ 50 vacancies. The positron lifetime measurements for the sample annealed under 10 bar of P_{As} (Fig. 6.1) shows a maximum effect after annealing at 750 K. The lifetime decomposition is represented in Fig. 6.4. τ_1 is always less than τ_b . In the low temperature region ($T < 100 \text{ K}$), the 260-ps component is fixed to decrease the statistical uncertainties of the fitting. With increasing the measurement temperature the value of τ_2 increases

up to 300K. For a further temperature increase, three-component decomposition is predominant with $\tau_3 \approx 600 \pm 35$ ps (the lower panel of Fig. 6.4). This indicates the generation of vacancy cluster with $N > 50$ vacancy. The value of τ_2 oscillates around 290 ps (monovacancy) with an intensity I_2 of 66 %. I_3 increases with the temperature to 7 % (upper panel of Fig. 6.4).

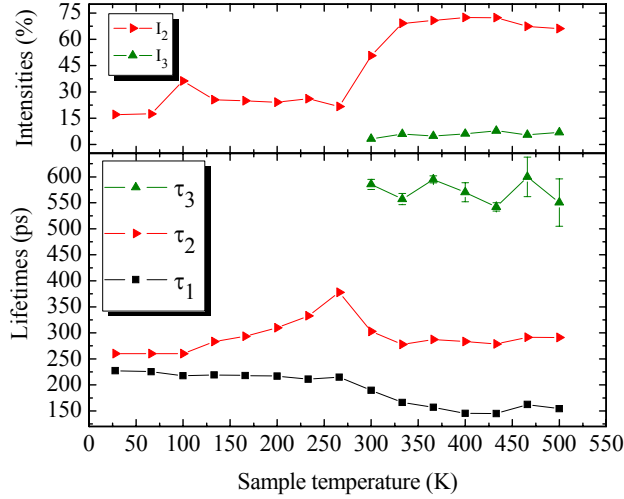


Fig. 6.4: Positron lifetime decomposition as a function of sample temperature in Cu diffused GaAs:Te at 1100 °C under 10 bar of As vapor pressure. The sample is isochronally annealed up to 750 K. Then, the temperature-dependent lifetime experiment was performed. The average lifetime is represented in Fig. 6.1.

The positron annihilation fraction (η_2, η_3) for the defect-related lifetimes is estimated using Eqs. (6.8, 6.11) and illustrated in Fig. 6.5. It is found that the annihilation fraction of the second component increases with the temperature and reaches 0.35 due to the increase in the trapping rate. η_3 increases to reach only 0.05 which indicates the low value of the trapped positrons fraction to the vacancy clusters.

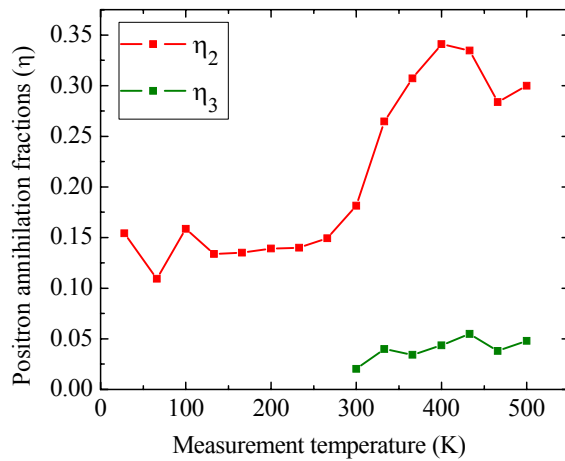


Fig. 6.5: Positron annihilation fraction versus the measurement temperature calculated using the lifetime decomposition presented in Fig. 6.4.

Conventional Doppler broadening spectroscopy was performed for the same sample to see the effect on the valence annihilation parameters, S . Commonly, it is accepted that the value of S for the positron annihilation in vacancy-type defects is larger than that in the bulk. Figure 6.6 shows the temperature dependence of S parameter in Cu diffused GaAs:Te sample annealed at 1100 °C under 10 bar of P_{As} . Then the samples are subject to isochronal annealing up to 750 K. S values are normalized to the corresponding bulk values, S_b measured in SI GaAs showing no positron trapping. The value of S was found to increase with the increase of the measurement temperature and that of W decreases. Thus, the observed increase in the value of S means an

increasing fraction of the annihilation of positrons in vacancy-type defects. This agrees with the lifetime measurements.

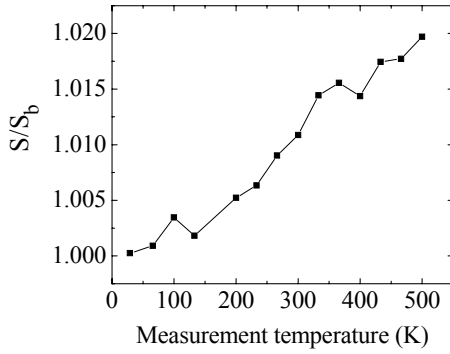


Fig. 6.6: The measured S parameter as a function of the sample temperature for Cu diffused GaAs:Te under 10 bar of P_{As} . The sample is annealed up to 750 K. Afterward, the temperature-dependent Doppler broadening experiment was carried out.

Due to the steep decrease in the positron lifetime after annealing the sample at 850 K (Fig. 6.1), another GaAs:Te sample was treated under the same conditions and annealed up to 825 K to see the effect on the longer lifetime component. Then, the temperature-dependent positron lifetime measurement is performed as shown in Fig. 6.7. The average lifetime increases from 224 ps in the low temperature region ($T < 100$ K) to 234 ps at $T > 300$ K. It was found that the value of τ_1 at $T > 300$ exceeds that of the bulk lifetime which reflects a complete trapping of positrons. It is important to note that the defect-related lifetime τ_2 reaches values as high as 750 ps but with low intensity $\sim 1\%$ (the upper two panels of Fig. 6.7). This supports the assumption that the vacancy clusters grow and their density decreases. During further annealing, the lifetime decreases and the vacancy signal disappears (Fig. 6.1). Thus, these results support the hypothesis that the distance between the clusters becomes distinctly larger than the diffusion length of positrons, and thus they are invisible for positrons. It was assumed that the small clusters combine to each other forming large voids with a distance between them being so large that they are not seen by positron any more [131].

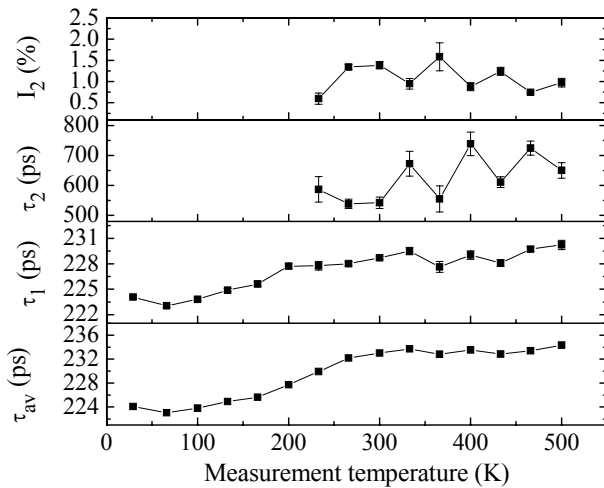


Fig. 6.7: Positron lifetime decomposition as a function of sample temperature in Cu-diffused GaAs:Te. Cu in-diffusion is performed at 1100 °C under 10 bar of As vapor pressure. The sample was isochronally annealed up to 825 K. Subsequently, the temperature-dependent lifetime experiment was performed.

The results above are compared to those obtained for a sample annealed under very similar conditions which was not treated with Cu in order to demonstrate the effect of Cu. As illustrated in Fig. 6.8, the as-quenched sample shows a higher value of the average lifetime (236 ps) which is very small compared to the Cu-diffused sample (275 ps after annealing at 750 K). This can be explained by trapping of positrons in vacancies. The decrease of the lifetime in the low temperature region is ascribed to the positron trapping into shallow traps. The shallow traps are attributed to intrinsic defects (e.g., Ga_{As}^{2-}) [95] or extrinsic defects [96].

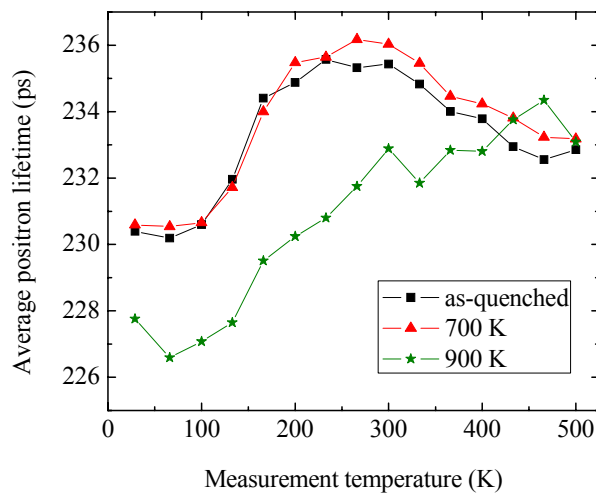


Fig. 6.8: Average positron lifetime as a function of sample temperature in GaAs:Te. The sample was annealed at 1100 °C under 10 bar of As pressure and quenched. The sample was not treated with copper and is thus a reference experiment to the results shown in Fig. 6.1. The samples were annealed up to 900 K. The temperature dependent lifetime experiment was performed for the sample in the as-quenched state and after annealing at 700 K and 900 K.

τ_{av} decreases slightly with increasing the annealing temperature in the temperature range up to 400 K. This is due to the fact that vacancies disappear during the annealing. At 500 K the average lifetime is almost the same which can be attributed to the diffusion of shallow traps, what leads to the decrease of τ_{av} only in the low temperature region. In contrast, in the case of the GaAs:Te after Cu in-diffusion (Fig. 6.1), almost no change in the average positron lifetime was detected in the as-quenched state. However, during the annealing steps until 750 K, the average positron lifetime increases strongly, and at annealing temperatures higher than 850 K the vacancy cluster signal almost disappears. This indicates that the observed vacancy-like defects in the cu-diffused sample are Cu-induced.

6.3.2 Sample annealed under 0.2 bar

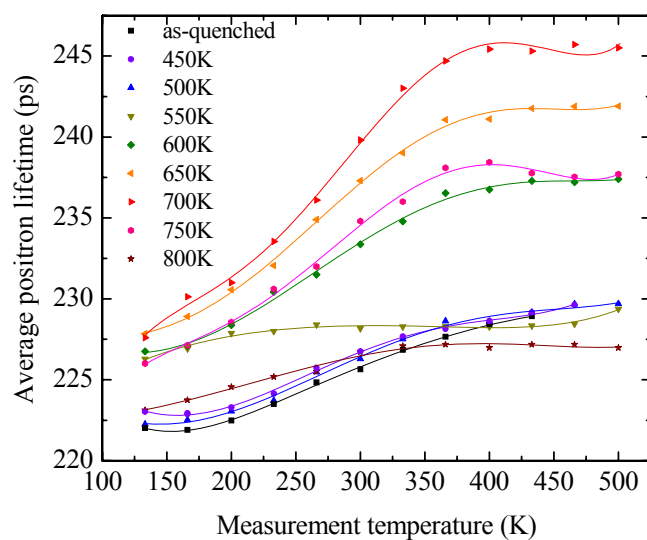


Fig. 6.9: Average positron lifetime as a function of sample temperature in GaAs:Te. Before the experiment, about $6 \times 10^{18} \text{ cm}^3$ Cu atoms were deposited onto the sample surface. Cu in-diffusion is performed for 3 h at 1100 °C under 0.2 bar of As vapor pressure. Therefore, the sample is quenched into water at RT. It is isochronally annealed. The temperature-dependent lifetime experiment was carried out after each annealing step.

To show the effect of the As vapor pressure, another sample is annealed at 1100 °C under 0.2 bar of P_{As} . Figure 6.9 presents the average lifetime as a function of the sample temperature after different annealing steps performed after Cu in-diffusion at 1100 °C under 0.2 bar of arsenic vapor pressure (As temperature is 550 °C). The lifetime measurement of the as-quenched sample shows no positron trapping to open-volume defects. The average lifetime in the high temperature region is

very close to the bulk lifetime in SI GaAs (228 ps). As the temperature decreases, the lifetime decreases which is a typical dependence for shallow traps. This is clearly shown for all curves. Almost no change was observed for the first annealing steps up to 500 K. As mentioned above, for Cu diffused sample, the shallow traps should be ionized Cu acceptor. In the course of annealing up to 700 K, the average positron lifetime increases and reaches 246 ps, indicating the detection of vacancy-like defects. This lifetime value is much lower than that in case of Cu diffused sample under 10 bar of P_{As} , 275 ps, (Fig. 6.1). With an additional increase in the annealing temperature, a rapid decrease in the average positron lifetime was observed. Figure 6.10 shows the positron lifetimes and the intensity of the defect-related lifetime (I_2) versus the annealing temperature for GaAs:Te after diffusion of $6 \times 10^{18} \text{ cm}^{-3}$ Cu atoms at 1100 °C under 0.2 bar of As pressure. The spectra were measured at 500 K to avoid the effect of shallow traps. The spectra measured after the first annealing steps up to 550 K show only one component lifetime of value very close to the bulk lifetime. At annealing temperatures higher than 550 K the spectra show two-component decomposition with $\tau_2 = 280 \pm 3$ ps which lies in the monovacancy region [133]. It is much lower than the divacancy value of 332 ps [79]. Thereafter, the number of vacancies in the annealing temperature range (600- 750 K) is estimated to be only one vacancy. The intensity of the second component is presented in the upper panel of Fig. 6.10. I_2 increases from 60 % at 600 K to 68 % at 700K then decreases for further annealing temperature. Because the intensity of the defect-related lifetime is proportional to the defect concentration, this high value of I_2 leads to higher values of defect concentrations although the lifetimes (τ_2) are not so high. Figure 6.11 illustrates the defect density against the annealing temperature. The defect concentration is calculated from the lifetime decomposition according to Eq. 3.9. It increases from $5.2 \times 10^{16} \text{ cm}^{-3}$ at 600 K to $9 \times 10^{16} \text{ cm}^{-3}$ at 700 K of annealing temperature. At an annealing temperature of 750 K, the defect concentration decreases to be $3.8 \times 10^{16} \text{ cm}^{-3}$.

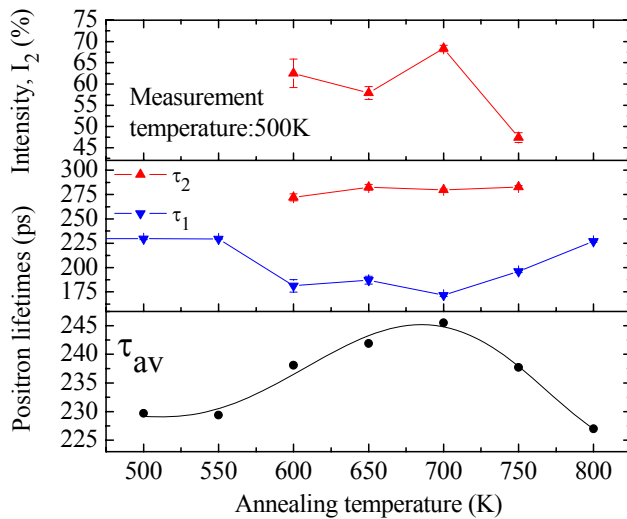


Fig. 6.10: Positron lifetime results of the isochronal annealing experiment of GaAs:Te. In-diffusion of $6 \times 10^{18} \text{ cm}^{-3}$ Cu atoms is performed at 1100 °C under 0.2 bar of P_{As} . The average lifetime is shown in the lower panel. The lifetimes and their relative intensities versus the annealing temperature are plotted in the two upper panels. The spectra were measured at a sample temperature of 500 K to diminish the influence of the shallow traps.

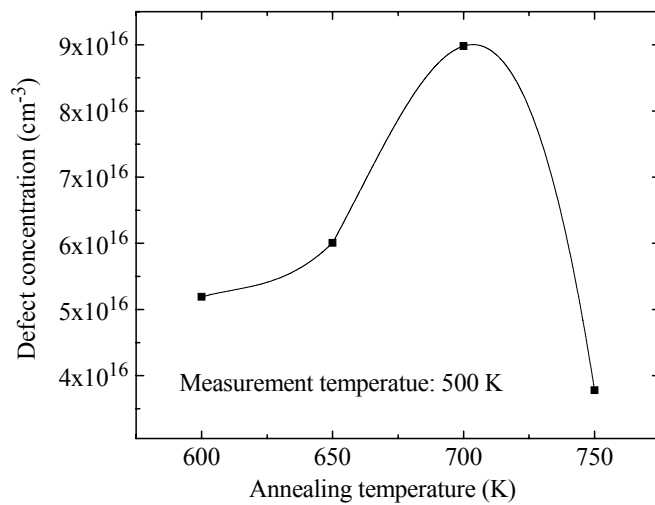


Fig. 6.11: Defect concentration versus the annealing temperature in Cu diffused GaAs:Te under 0.2 bar of As vapor pressure. These data were estimated using the positron lifetime results presented in Fig. 6.10.

The positron lifetime for different defects and for V_{Ga} surrounded with different numbers of Cu atoms for unrelaxed structure in GaAs is calculated using atomic superposition method [80,105] as tabulated in table 6.1. It is clearly shown that with increasing the number of Cu atoms surrounding V_{Ga} the lifetime increases. The experimentally observed lifetime (280 ps) is higher than the theoretically calculated lifetime value of the isolated V_{Ga} (267 ps) and also less than that of V_{Ga} decorated with 2 Cu atoms (283 ps). Thus, it is more probable that the detected defect is $V_{\text{Ga}}\text{-Cu}_{\text{Ga}}$ complex (276 ps). This is also supported with the calculated momentum distribution (Fig. 6.12).

Vacancy	Lifetime (ps)
GaAs bulk	232
$V_{\text{Ga}}\text{-}V_{\text{As}}$	332
V_{Ga}	267
$V_{\text{Ga}}\text{-}1\text{Cu}_{\text{Ga}}$	276
$V_{\text{Ga}}\text{-}2\text{Cu}_{\text{Ga}}$	283
$V_{\text{Ga}}\text{-}3\text{Cu}_{\text{Ga}}$	291
$V_{\text{Ga}}\text{-}4\text{Cu}_{\text{Ga}}$	298

Table 6.1: Theoretically calculated positron lifetime for different vacancies and vacancy complexes in GaAs for unrelaxed structure.

6.3.3 Stoichiometry effect

During the isochronal annealing, Cu_{Ga} atoms dissolve leaving their sites (Ga sublattices) and start the out-diffusion forming precipitates which are connected to the vacancy clusters. The formation of vacancy clusters can be understood taking into account that the atomic density of Cu ($8.48 \times 10^{22} \text{ cm}^{-3}$) is two times larger than that of GaAs ($4.43 \times 10^{22} \text{ cm}^{-3}$). Thus, when Cu atoms leave the Ga sublattice and form precipitates some open-volume defects must be generated. In the first place, these are V_{Ga} . But because of the observed large defect-related lifetime, vacancies in both sublattices should be comprised. Thereafter, As atoms must leave and go into interstitial sites. If it is so, this process should depend on the stoichiometry, i.e. depends on the amount of the excess As in GaAs. That is already observed for the samples annealed under different As vapor pressure (see Fig. 6.1 and Fig. 6.9). In case of the sample annealed under 10 bar of P_{As} , the average positron

lifetime reached 275 ps. The defect-related lifetime showed the formation of vacancy clusters. On the other hand, the sample annealed under 0.2 bar of P_{As} showed an average lifetime of 246 ps and the defect-related lifetime corresponds to monovacancies. Thus, the higher the As vapor pressure during Cu in-diffusion is, the easier the As atoms go into the interstitial region, and the more pronounced is the course of void formation.

6.4 Results of coincidence Doppler broadening measurements

Due to the high solubility and high diffusivity of copper in GaAs, it was assumed that these vacancy clusters are decorated by Cu precipitates [109,131]. To confirm whether the observed vacancy-like defects are surrounded by Cu atoms, CDBS measurement is carried out. The most important parameter is the shape of high momentum distribution. Core annihilation parameter (W parameter) is responsive to the chemical surroundings of the annihilation site.

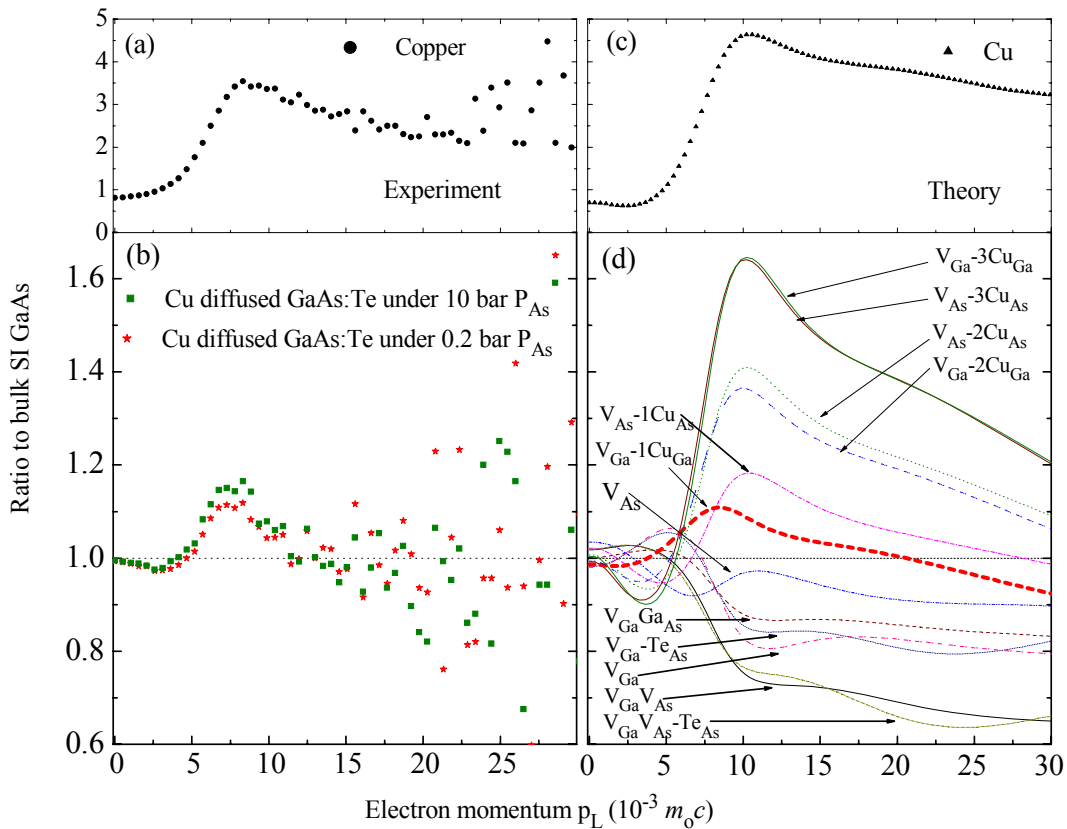


Fig. 6.12: High momentum part of the positron annihilation momentum distribution, normalized to SI undoped GaAs reference (left part). In the upper part (a) the spectrum for pure copper is shown, lower part (b) represents spectra of two GaAs:Te samples: In one of them, the Cu in-diffusion is performed under 0.2 bar of P_{As} and annealed subsequently up to 700 K. For the other, the Cu in-diffusion is carried out under 10 bar of P_{As} and the sample is subject to isochronal annealing up to 750K. The right part shows the ratio of high momentum distribution to the bulk GaAs for pure Cu (c) and different vacancies in GaAs (d) from theoretical calculations. The calculation was done using GGA. The curve of $V_{Ga}-Cu_{Ga}$ complex is highlighted to emphasize the agreement to the respective experimental data in GaAs:Te annealed samples.

The results of coincidence Doppler broadening measurements are shown in the left part of Fig. 6.12. The spectra measured at 466 K, normalized to an undoped SI GaAs reference sample showing no positron trapping. In panel (a) of Fig. 6.12, the ratio curve of annihilation momentum

distribution obtained in pure copper is shown. In panel (b), two samples are measured, GaAs:Te diffused with Cu under 0.2 bar then annealed up to 700 K and Cu diffused GaAs:Te under 10 bar annealed up to 750 K. If positrons annihilate with core electrons of copper the intensity in the high momentum distribution area of the Doppler peak at $(7-20) \times 10^{-3} m_0 c$ is higher than in bulk GaAs (ratio is larger than 1, panel (a) of Fig. 6.12). Thus, the existence of Cu atoms in the immediate neighborhood of a positron trap can be seen as such distinct increase of the intensity of the electron momentum distribution. Cu being incorporated on the Ga sublattice is an adjacent neighbor to vacancy-like defect and thus must be perfectly observed at the high momentum part of CDBS spectrum. The ratio curves of both annealed samples show a clear sign that Cu atoms are in the vicinity of the detected vacancies. This is because the shape of momentum distribution for both annealed GaAs:Te samples is very similar to the spectrum of pure Cu. Consequently, the results of the high momentum part of annihilation momentum distribution for the Cu-diffused GaAs:Te is determined by the annihilation of positrons with the core electrons of Cu atoms [131,138]. These results provide us with support for the hypothesis that the observed vacancy-like defects are decorated with copper. The presence of such cluster-Cu precipitate complexes was observed by Transmission Electron Microscopy (TEM) [131].

Theoretical calculations of the annihilation momentum distribution were performed to support the experimental findings. These calculations were carried out using the method introduced in Refs. [98,105]. This method is found to give momentum distribution and positron lifetime in GaAs in sufficient agreement with the experiment [105]. The momentum distribution is calculated via the free atomic wave functions within the model of the independent particles for each core electron state. The final momentum distribution is given by taking the summation of the contributions from each state weighted by the partial annihilation rates calculated within the generalized gradient approximation (GGA) of positron annihilation [168]. The lattice relaxation was not taken into account within the calculations. The momentum distribution of Cu is calculated and represented as a ratio to the bulk GaAs in Fig. 6.12, panel (c). It is clearly shown that theoretically calculated and measured momentum distributions are in a reasonable agreement. The theoretically calculated momentum distributions for V_{Ga} , V_{As} , the divacancy and for different possibilities of surrounding them by Cu atoms in GaAs (normalized to the bulk distribution) are shown in panel (d) of Fig. 6.12. A probable shift in the calculated curves is due to the approximation and unrelaxed coordinates. It is clearly shown in the calculated curves that with increasing the Cu atoms bound to the vacancy the ratio of the curves increases. This agrees with the assumption of the presence of Cu in the immediate vicinity of the observed vacancy-like defects. The momentum distribution curve for the V_{Ga} surrounded by one Cu atom incorporated into the Ga sublattice ($V_{Ga}-Cu_{Ga}$) is very close to the experimental curves of the annealed samples under 0.2 and 10 bar of P_{As} . Thus, the detected defect is supposed to be $V_{Ga}-Cu_{Ga}$ complex.

6.5 Determination of concentration of shallow traps and positron binding energy

The decrease of the average lifetime in the low temperature region is a direct evidence for the existence of shallow positron traps. Positron diffusion length experiments were used as a direct probe for shallow traps [88]. Positrons getting trapped to the shallow traps have a lifetime very close to those of the bulk, which results in difficulties for the determination of the detailed microscopic structure of the shallow traps. This is because these traps are not of vacancy type and do not involve open-volume. In the samples under investigation, after Cu diffusion, Cu double acceptors act as shallow trap centers [93]. To estimate the concentration of shallow traps, the one

and two defect type trapping models were used. At the first annealing steps up to 500 K, the decomposition of the lifetime spectra shows only one component in the whole temperature range. For these annealing steps, one defect type model is used to determine the trapping rate at 29 K. Where $\tau_d = \tau_{st} = 220$ ps is assumed. As mentioned above, this lifetime value is observed in the as-quenched sample. The trapping rate for shallow traps can then be calculated by applying Eq. (3.17). Using Eq. (3.9), the concentration of shallow traps can be determined. A trapping coefficient $\mu = 5 \times 10^{16} \text{ s}^{-1}$ is applied [79]. At annealing temperatures higher than 550 K the spectra consist of two lifetime components, especially in the high-temperature region, what indicates the detection of vacancy-like defect as well as shallow traps which are effective only at low temperature. Thus, the model of two defect types should be used. The positron trapping rate to vacancies is estimated in the high temperature region (where no effect of shallow traps is expected). Then the trapping rate to shallow traps at 29 K could be calculated. The estimated concentration of the shallow traps versus the annealing temperature is shown in Fig. 6.13. It is found that the value estimated at the annealing temperature of 450 K is very close to that measured using Hall measurement ($2.2 \times 10^{17} \text{ cm}^{-3}$). With increasing the annealing temperature the concentration of shallow traps decreases and saturates at 10^{16} cm^{-3} . After Cu in-diffusion, Cu is in an oversaturated state according to the solubility. With annealing, Cu atoms have the propensity to leave their lattice sites and start the out-diffusion, e.g., forming precipitates. This results in a decrease of the electrically active fraction of Cu, i.e. a decrease of the concentration of the acceptors and thus shallow traps.

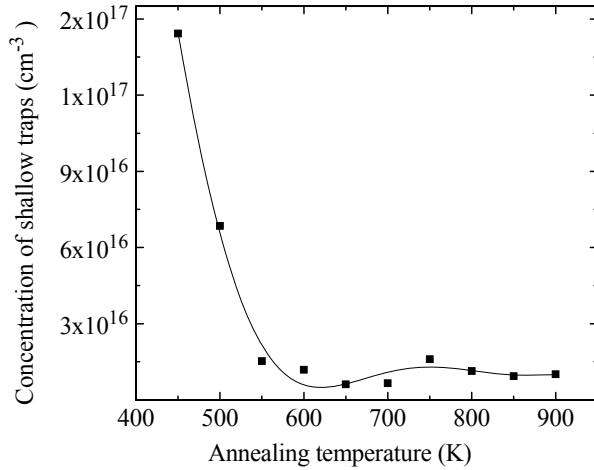


Fig. 6.13: The concentration of shallow positron traps determined at 29 K as a function of the annealing temperature in Cu diffused GaAs:Te annealed under 10 bar of P_{As} . The calculation was performed using the decomposition of positron lifetime results shown in Fig. 6.1.

The ratio of the detrapping (δ) and trapping rates is given by the thermodynamic approach to detrapping of positron from the defect [90] according to Eq. (5.6). Eq. (5.6) is fitted to the experimental data, after the corresponding trapping equations are solved to determine the transition rates δ and κ_{st} . The three-state trapping model, as described in section 5.3.4, is applied. An experimental formula for positron detrapping transition is given by the solution of the kinetic trapping equation [139] in accordance with Eq. (5.5). Taking into account that, here $\lambda_{st} = \tau_{st}^{-1} = (220 \text{ ps})^{-1}$ is assumed. In order to obtain the experimental detrapping rate using Eq. (5.5), information on the temperature dependencies of κ_v and κ_{st} is needed. The simultaneous determination of three parameters κ_v , κ_{st} , and δ from the experimental data is impossible. This was simplified by assuming that the trapping rates κ_v and κ_{st} do not depend on the temperature [88]. The value of κ_v is evaluated at high temperature, $T > 400$ K, (where no positron trapping to shallow traps and the lifetime is saturated). κ_{st} is estimated at very low temperature, close to 0 K, (no thermal detrapping).

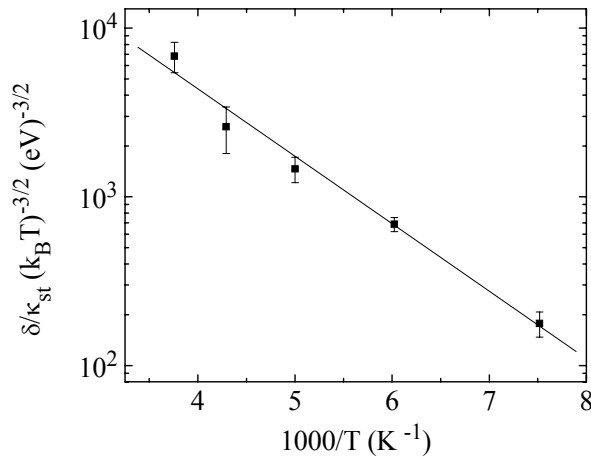


Fig. 6.14: The ratio of the detrapping and trapping rates in Cu diffused GaAs:Te annealed under 10 bar of P_{As} calculated from the decomposition of the lifetime spectra after annealing the sample at 650 K using Eq. (5.5). The solid line is the fit of Eq. (5.6) to the experimental data with $E_b = 79.4$ meV.

Figure 6.14 shows the Arrhenius plot of the measured detrapping rates from Eq. (5.5) in Cu diffused GaAs:Te annealed under 10 bar of P_{As} determined from the decomposition of positron annihilation lifetime spectra measured after annealing at 650 K. The solid line in Fig. 6.14 represents the fit of Eq. (5.6) to the experimental data. The slope yields a binding energy of (79.4 ± 6) meV. The detrapping rate is noticed to agree with the trapping rate ($\kappa_{st} = \delta$) at 166 K. All the lifetime spectra measured after annealing the sample at 650 K show two-component decomposition. But the decomposition below 100 K is not so reliable, thus a 255-ps component is fixed to reduce the statistical uncertainties of the fitting. The positron, as a positively charged particle, can get localized into the Rydberg states of a Coulomb field around these centers. The binding energy of the positron to these states can be estimated using a simple formula: [88,169]

$$E_b = \frac{13.6 \text{ eV}}{\epsilon^2} \left[\frac{m^*}{m_0} \right] \frac{1}{n^2}, \quad (6.12)$$

where ϵ is the dielectric constant of the material ($\epsilon = 12.9$ in GaAs) and n is the quantum number. In all solids, the effective mass of positron is very close to its free mass ($m^* = m_0$) [170]. A value of $E_b = 81.7$ meV is obtained using Eq. (6.12) for the binding energy in the first Rydberg state ($n=1$). It is worth mentioning that the experimentally determined value of binding energy is in excellent agreement with that value calculated by Eq. (6.12). E_b is determined for n -type GaAs as (43 ± 5) meV [88] and for GaAs:Te as (60 ± 20) meV [43]. These earlier results are explained by detrapping of positrons from the excited states, whereas the obtained results indicate that positrons are detrapped from the first state. The trapping coefficient of positrons to the Rydberg states can be estimated using the concentration $2.2 \times 10^{17} \text{ cm}^{-3}$ of ionized acceptor-like centers obtained from Hall measurement. When the detrapping possibility approaches zero ($T < 100$ K), κ_{st} has a value of $1.63 \times 10^{11} \text{ s}^{-1}$ (for the sample annealed at 450 K). Using Eq. (3.9), the specific trapping rate is estimated to be $3.2 \times 10^{16} \text{ s}^{-1}$. It is comparable to the large capture rate for positrons at negatively charged vacancies in GaAs [79,96]. This is not surprising because negatively charged vacancies are surrounded by very similar attractive Coulombic tails.

6.6 Conclusion

In this chapter positron annihilation in GaAs:Te ($3.5 \times 10^{17} \text{ cm}^{-3}$) after Cu diffusion at 1100 °C under two different As vapor pressures (0.2 and 10 bar) has been systematically studied. The following conclusions were made.

- 1) The as-quenched samples show only one positron lifetime component lower than the bulk lifetime at low temperature due to strong trapping to shallow traps. The behavior of the temperature dependent average positron lifetime can be attributed to thermally assisted positron detrapping from these shallow traps.
- 2) During a subsequent post-annealing up to 750 K after the diffusion under 10 bar of P_{As} , the average positron lifetime increases strongly indicating the creation of vacancy-type defects. With a further increase in the annealing temperature to 850 K, a steep decrease in the average positron lifetime was found. It can be ascribed to the fact that vacancy clusters grow and the distance between them becomes larger than the positron diffusion length. To show that the observed vacancy-like defects are induced by Cu diffusion, GaAs:Te samples were annealed under very similar conditions but not treated with Cu. The as-quenched sample gave a higher value of the average lifetime but it is much smaller compared to the measured value in Cu-diffused sample.
- 3) The annealing behavior of the average lifetime shows the increase of the open-volume of the observed vacancy-like defects. Vacancy clusters decorated with Cu atoms are generated in the sample annealed under high arsenic vapor pressure. They grow up to a size of more than 50 vacancies with increasing the annealing temperature. The sample annealed under low arsenic pressure shows vacancy-like defect decorated with Cu. But its value lies in the monovacancy region.
- 4) The defect concentration was found to increase with increasing annealing temperature up to 750 K. The number of vacancies incorporated in the observed clusters also increases with increasing annealing temperature in the sample annealed under high As pressure.
- 5) As far as the vacancies in both sublattices of GaAs must be involved, the creation of the open-volume defects should depend on the stoichiometry of the GaAs system. A larger quantity of excess arsenic should support the formation of vacancy clusters. This means that As atoms go into interstitial sites more easily.
- 6) Coincidence Doppler broadening measurements showed the presence of copper in the vicinity of the detected vacancy-like defects. Thus, the observed vacancy-type defects are assumed to be bound to Cu impurities or vice versa. This is supported by the theoretical calculation of the momentum distribution which predicted the trapping of positrons to $V_{Ga}-Cu_{Ga}$ complexes.
- 7) Vacancy-like defects as well as shallow positron traps (negatively charged non-open volume defects) were observed. The Cu content explained the observation of shallow traps. Cu ionized acceptors (Cu_{Ga}^{2-}) act as the observed shallow traps.
- 8) The shallow trap concentration was calculated using the positron trapping model. The calculated value agrees with that measured using Hall-effect.
- 9) A thermal detrapping from the annihilation state (shallow traps) was observed in the temperature range 100-400 K. An analysis of the lifetime in terms of detrapping from shallow traps gives a binding energy of $E_b = (79.4 \pm 6)$ meV for localized positrons which is compatible to the calculated value.
- 10) The trapping coefficient of positrons to shallow traps at 29 K was estimated to be $3.2 \times 10^{16} s^{-1}$. This is comparable to earlier published values.

7. Cu diffusion-induced vacancy-like defects in freestanding GaN

7.1 Introduction

For about two decades gallium nitride (GaN) has been attracting a great deal of attention due to its advantageous optical, thermal, and electrical properties that can be exploited to implement a variety of novel or superior electronic and optoelectronic devices [171]. Particularly, its wide and direct band gap of 3.4 eV enables the fabrication of unique devices such as blue laser diodes opening up new applications in optoelectronics, data storage, and biophotonics [172]. These diodes are typically made of high quality In-rich InGaN quantum wells grown on low dislocation density bulk or free-standing GaN (fs-GaN) substrates. Fs-GaN wafers needed for the fabrication of these emerging devices are currently produced by hydride vapor phase epitaxy (HVPE) at elevated temperatures as described in Ref. [173]. From a fundamental standpoint, exploring and elucidating the formation of defects and their behavior are of paramount importance to the understanding of the properties of GaN-based systems [174-184]. Theoretical calculations predict that Ga vacancies and related complexes are the most dominant point defects in *n*-type GaN [181-183]. These calculations show that both isolated and complexed Ga vacancies are plentifully generated in *n*-type GaN, whereas the dominating native defect in *p*-type GaN is the N vacancy. Moreover, it was demonstrated that Ga vacancies are electrically active behaving as acceptors, and involved in the optical transition causing the emission of yellow luminescence light [181,184]. Besides their influence on the basic properties of GaN, qualitative and quantitative investigations of defects formation in GaN are also crucial to understand and control the emerging fabrication processes of advanced hybrid substrates [185].

Also of fundamental as well as practical importance is the understanding of the behavior of impurities and their role in shaping the electrical and structural properties of GaN. Copper is among the impurities in GaN that has recently sparked a surge of interest because of the associated room-temperature ferromagnetism, which could create new opportunities in GaN-based spintronics [186-192]. The extent of this Cu-induced ferromagnetism is, however, still under debate [187]. A possible role of vacancy-like defects was postulated as a key factor that should be considered to address this intriguing effect [189,190]. In addition to this intentional doping, the presence of Cu is also encountered during semiconductor device growth and processing [164]. Recently, the thermal stability of Cu gate AlGaIn/GaN high electron mobility transistors was investigated [193,194]. These reports do not show any obvious degradation in the device performance upon thermal annealing up to 500 °C. Moreover, no Cu diffusion up to this temperature is observed at the Cu and AlGaIn interface as demonstrated by secondary ion mass spectroscopy [193,194]. This illustrates that the Cu diffusivity in GaN is very low as compared to other semiconductors such as GaAs [17,93]. It is worth pointing out that the majority of the available experimental reports deal with defects in GaN epilayers grown on foreign substrates. These layers contain much higher densities of growth defects and dislocations as compared to fs-GaN. Therefore, the extrapolation of the result of these studies to bulk GaN might be fraught with uncertainties.

The present work addresses the formation of vacancy-like defects and their thermal behavior upon diffusion of Cu in light emitting diode quality fs-GaN crystals. Unlike GaAs and Si (see, for example, Ref. [93] and references therein), the influence of Cu on defect formation has never been investigated in GaN heretofore in spite of the crucial information it could provide regarding the fundamental properties of GaN. Positron annihilation spectroscopy (PAS) is employed in this study. This tool is an established non-destructive technique for the investigation

of defects in semiconductors [79]. PAS can be used to detect vacancy-type defects, e.g. monovacancies and divacancies, with concentration above 10^{14} - 10^{15} cm⁻³. In this technique, positrons are trapped in an open-volume defect (e.g. vacancies) due to the missing positive ion core (nucleus) at that site. The trapping can be experimentally observed either as an increase in the positron lifetime or as a narrowing of the Doppler-broadened 511 keV γ -annihilation peak. Vacancy-type defects in group III-nitride were previously investigated using this technique [195-203]. Those studies have demonstrated that PAS can clearly distinguish between vacancies and vacancy-impurity complexes. Recent lifetime PAS studies of H-implanted and annealed fs-GaN under the ion-cut conditions have provided the evidence of the formation of the positronium besides the detection of monovacancies, divacancies, and vacancy clusters [204]. In this study, the positron lifetime spectroscopy probe of Cu-diffused GaN shows that annealing is associated with the appearance of a relatively long lifetime component attributed to vacancy clusters, whereas a small change in the average lifetime is detected. SIMS analysis showed the presence of Cu in the 600 nm-thick layer below the surface. To characterize the open-volume defects in this, variable energy Doppler broadening spectroscopy has been employed. The thermal behavior of the observed vacancy-like defects suggests that their formation is related to Cu out-diffusion.

7.2 Experimental details

The investigated samples were cut from nominally undoped 300 μ m-thick double side polished high purity 2 inch fs-GaN wafers grown by HVPE [205]. The as-grown samples show *n*-type conductivity with a free electron concentration of about $N_e = 2 \times 10^{18}$ cm⁻³ at 300 K. This doping is most probably caused by the residual oxygen. The resistivity of initial material was about 10^6 Ω cm. The samples were covered by 18 nm thick Cu layer evaporated under ultrahigh vacuum conditions. The deposited layer thickness was controlled by frequency shift of a crystal oscillator which was previously calibrated before by Atomic Force Microscopy. High purity Cu-free quartz ampoules were employed for annealing to induce the diffusion of Cu into fs-GaN samples. The samples were sealed in the quartz ampoules under argon. The annealing was performed for 96 hours at 873 K. As demonstrated below, Cu diffuses into GaN lattice (in-diffusion) during this process. After annealing, the ampoules were quenched into water at room temperature. Cu introduced into the crystal is now at this low temperature expected to be oversaturated. Thus, the Cu atoms have the propensity to leave the lattice (for instance forming precipitations) and, hence, start the out-diffusion. To study this process, the samples were isochronally annealed at different temperatures up to 850 K and slowly cooled down after each annealing step. Between the annealing steps, positron annihilation lifetime spectroscopy (PALS) measurements were carried out in the temperature range of 30-500 K using a conventional fast-fast coincidence system with a time resolution (FWHM) of 220 ps. The lifetime spectra were analyzed by the program LT [86] as a sum of exponential decay components convoluted with the Gaussian resolution function of the spectrometer after source and background correction. The positron in the state *i* annihilates with a lifetime τ_i with an intensity I_i . The state in question can be either a delocalized state in the lattice or a localized state at a vacancy-type defect. An average lifetime above the defect-free bulk lifetime is indicative of the presence of vacancy-like defects in the material. This parameter can be experimentally determined with high accuracy and even a small change as 1 ps in its value can be reliably measured. The analysis is insensitive to the used decomposition procedure. The trapping of positron in an open-volume defect is observed as an increase in the τ_{av} . A vacancy-like defect can be identified by the characteristic lifetime component in the lifetime spectrum.

Depth-profiled Doppler broadening measurements of the as-grown and Cu-diffused GaN (GaN:Cu) samples were performed using a variable energy positron beam to study the near-surface region. Monoenergetic positrons were produced by a 10 mCi ^{22}Na source assembled in transmission with a 1 μm monocrystalline tungsten moderator and transported in a magnetic guidance system to the sample. The beam spot is characterized with a diameter of 4 mm and an intensity of $10^2 \text{ e}^+/\text{s}$. The samples were measured at RT under UHV. A high purity Ge detector with an energy resolution of $(1.09 \pm 0.01) \text{ keV}$ at 511 keV was used to record the γ -annihilation spectra. The data were processed with a digital peak-stabilizing system integrated in the multi channel analyzer. A spectrum of about 5×10^5 counts in the 511 keV peak is accumulated at each energy E . The Doppler broadening spectrum of the 511 keV annihilation line is characterized by two parameters S and W . The trapping of positrons at open-volume defects is detected as an increase in S parameter and a decrease in W parameter. Using positron energies in the range of 0.03-35 keV it is possible to scan the GaN sample to a mean penetration depth of $\sim 2 \mu\text{m}$ below the surface. At a fixed positron energy E , the S parameter is described as $S(E) = \eta_s(E)S_s + \eta_b(E)S_b + \sum_i \eta_{d_i}(E)S_{d_i}$, where S_s and S_b are the characteristic values of S parameter for positron annihilation at the surface and in defect-free bulk GaN lattice, respectively. η stands for the fraction of positrons annihilating at each state. In the case of a sample containing defects that can trap positrons, the third term in the equation above should be taken into account. Here S_{d_i} characterizes the positron annihilations in a defect i .

Elemental depth profiles were performed using Time-of-Flight SIMS (ToF-SIMS) using an Iontof TOF.SIMS 5 apparatus. The Cu depth profiles in GaN were acquired in positive ion polarity with the O_2^+ sputter source (energy of 2 keV) with a measuring area of $150 \times 150 \mu\text{m}^2$ and a sputter area of $250 \times 250 \mu\text{m}^2$ each time. An electron flood gun was used for charge compensation. Furthermore, the investigations were carried out in the non interlaced mode for a better peak separation and smaller charging of the sample surface. In this operation mode the pulses of sputter and analysis gun are used separately. The measured intensity (in counts/s) is a qualitative concentration value due to the different ionization probabilities of a certain element in the investigated matrix system (matrix effect). The ToF-SIMS time scale corresponds to the depth in dependence of the abrasion rate. The calibration of the depth scale was performed by using a profilometer.

7.3 Results and discussion

SIMS is carried out on the as-quenched Cu-diffused sample. The results are displayed in figure 7.1. As it is clearly seen in the figure, a considerable amount of Cu is detected in the region extending to $\sim 600 \text{ nm}$ below the surface.

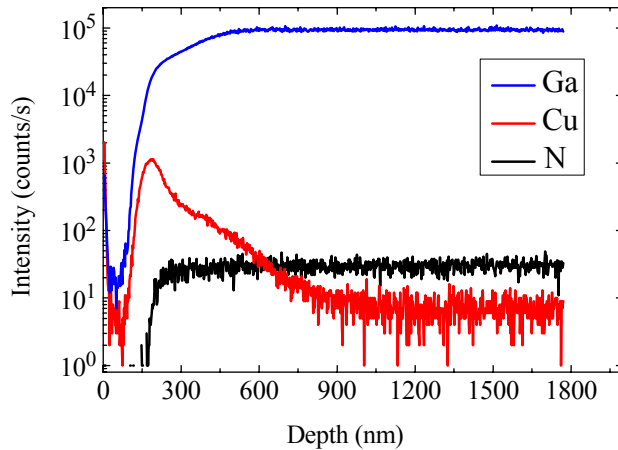


Fig. 7.1: SIMS depth profiles of GaN sample after Cu diffusion induced by annealing for 96 h at 873 K. Note that surface peaks are artifact of the SIMS measurements.

Figure 7.2 displays the positron lifetime spectra recorded for virgin fs-GaN and Cu-diffused fs-GaN and annealed at 550 K. In a positron lifetime experiment, positrons injected into the sample are thermalized at time $t = 0$. The vertical axis represents the number of positron-electron annihilation events at a time channel of 26 ps. In the reference sample, only a single exponential decay component with a lifetime of 154 ps is detected. This corresponds to the annihilation of positrons in the delocalized state of a nearly defect-free GaN lattice. This value is in a good agreement with earlier experimental and theoretical studies [206,207]. The annealing at 550 K of the Cu-diffused GaN sample induces an increase in the average positron lifetime by 4 ps. This increase is a direct evidence of open-volume defects introduced in the sample presumably during the out-diffusion of Cu. Note that this increase is comparable to earlier observations of 2 and 5 ps increase in the average lifetime in GaN after electron irradiation at fluences of $3 \times 10^{17} \text{ cm}^{-2}$ and $1 \times 10^{18} \text{ cm}^{-2}$, respectively [195].

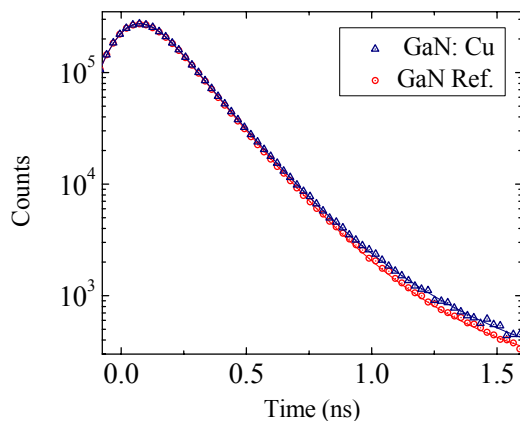


Fig. 7.2: Positron lifetime spectrum recorded for Cu-diffused fs-GaN after annealing at 550 K. For the sake of comparison, data of virgin fs-GaN are also displayed. The spectra were measured at 300 K.

After Cu in-diffusion, the as-quenched sample showed an average lifetime very close to that of the as-grown one. The average positron lifetime as a function of the measurement temperature carried out after annealing of Cu-diffused GaN is shown in figure 7.3. The average lifetime was found to increase slightly by increasing the annealing temperature up to 550 K, indicating the creation of vacancy-type defects. With a further increase in the annealing temperature, a decrease in the average positron lifetime was observed. A plausible reason for this decrease would be that at high temperatures vacancies migrate to the surface and anneal out, which decreases their concentration and hence the available positron traps. Additionally, the observed decrease can also be attributed to the agglomeration of vacancies to form clusters and the distance between them

becomes larger than the positron diffusion length. Thus, they become invisible for positrons [93]. The same behavior was observed during Cu diffusion in the semi-insulating GaAs [93]. But the increase in the average lifetime, $\Delta\tau = \tau_{av} - \tau_b$, was found to be very large in GaAs, 61 ps [93].

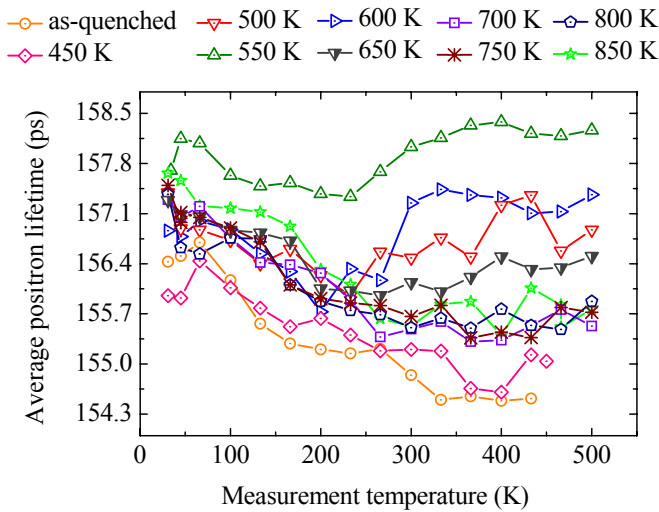


Fig. 7.3: Average positron lifetime measured for fs-GaN samples at different temperatures. The samples are isochronally annealed. The temperature-dependent lifetime experiment was carried out after each annealing step as indicated in the figure.

Figure 7.4 represents the behavior of the average lifetime measured after different annealing temperatures. It is found that the τ_{av} measured at 333 K increases by increasing the annealing temperature up to 550 K and then decreases upon annealing at higher temperatures. A defect-related lifetime (τ_d) of 298 ps with an intensity of 1.9 ± 0.1 % is observed at 450 K. This implies that positrons annihilate from a localized state at a vacancy-like defect. The open-volume of the N vacancy (V_N) is much too small to explain the observed long lifetime of 298 ps, where the theoretically calculated lifetime associated with V_N is 169 ps [184]. The observed lifetime of 298 ps is also higher than that corresponding to the Ga vacancy (V_{Ga}), 235 ps [184,195]. It can be inferred that the detected defects are possibly divacancies ($V_{Ga}-V_N$), which is consisted with earlier assignment of 260-282 ps to this complex [204]. τ_d increases by increasing the annealing temperature to reach 433 ps at 550 K and then decreases above this temperature. Its intensity is also small, 1.5 ± 0.04 %.

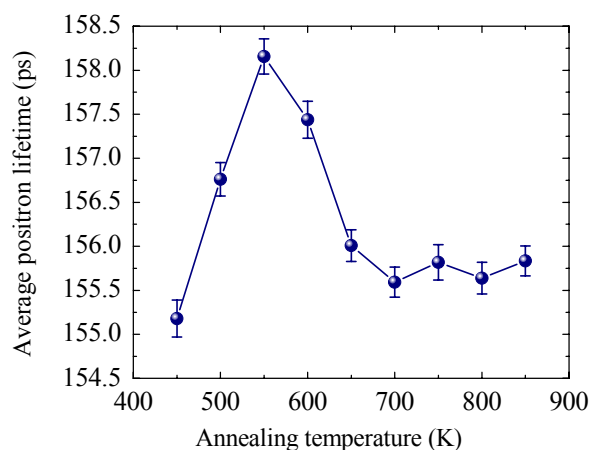


Fig. 7.4: Average positron lifetime of Cu-diffused fs-GaN samples after the isochronal annealing. The spectra were measured at a sample temperature of 333 K.

Note that this value of τ_d is much larger than that of the divacancy mentioned above. Thus, it can be associated with the formation of larger vacancy clusters at this temperature. In fact, the lifetime of 433 ps corresponds to a cluster of roughly 60 vacancies (30 GaN molecules are missing) according to calculations based on local density approximation for electron-positron correlation

effects and the atomic superposition method [207]. τ_1 is, however, found to be around the bulk lifetime.

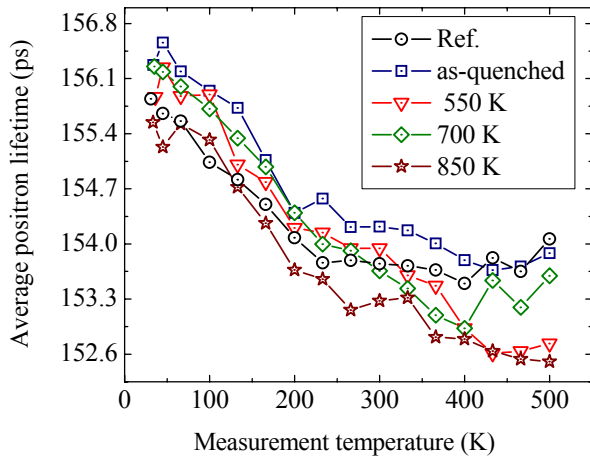


Fig. 7.5: Average positron lifetime of virgin fs-GaN sample as a function of the measurement temperature. The sample was annealed for 96 h at 873 K without deposition of Cu-cap layer. The sample is isochronally annealed at different temperatures. A reference sample before the annealing is also shown for comparison.

To demonstrate that the observed vacancy-like defects are Cu-related, a fs-GaN sample was annealed under similar conditions but without Cu treatment. The obtained lifetime results of this sample are exhibited in figure 7.5. As illustrated in the figure and independently of annealing, the as-quenched sample shows an average lifetime very close to that of the reference sample, which is 154.5 ps at RT. This behavior stands in sharp contrast to data of Cu-diffused GaN samples (figure 7.3). In Cu-free samples, the average lifetime decreases by increasing temperature (figure 7.5), but the change in the average lifetime remains below 1 ps over the entire temperature range. This indicates the presence of very low density of defects.

The formation of vacancies can be reasonably associated with the out-diffusion of Cu during the isochronal annealing of the sample. The out-diffusion process means the annealing of the Cu pre-introduced GaN samples in conditions without a Cu source, where the sample surface is not covered by any capping material. The diffusion mechanism is most likely the interstitial-substitutional (kick-out mechanism)[9]. In the case of Frank-Turnbull mechanism [11], the diffusing atom does not replace a lattice atom at its site, but gets trapped in a vacancy. Thus, for the Frank-Turnbull mechanism the material must contain a large number of vacancies, as large as the number of Cu atoms to be placed into the lattice. The positron lifetime investigations performed on initial (virgin) GaN material and Cu-diffused GaN in the as-quenched state did not show the presence of vacancies. This supports the suggestion of the occurrence of the kick-out mechanism. Nevertheless, more detailed studies are required to confirm the diffusion mechanism governing this process. In the kick-out mechanism, the interstitial-substitutional exchange can be described as $i_{\text{Cu}} \leftrightarrow \text{Cu}_{\text{Ga}} + \text{I}_{\text{Ga}}$, where i_{Cu} stands for Cu atoms on interstitial sites, Cu_{Ga} for Cu on Ga sublattices, and I_{Ga} for Ga self-interstitials. During the out-diffusion process upon thermal annealing, Cu atoms are likely to diffuse to possible sinks (surfaces, loops, or dislocations) leaving behind Ga vacancies in the matrix, $\text{Cu}_{\text{Ga}} \leftrightarrow \text{V}_{\text{Ga}} + \text{Cu}_{\text{sink}}$. These are most likely negatively charged vacancies.

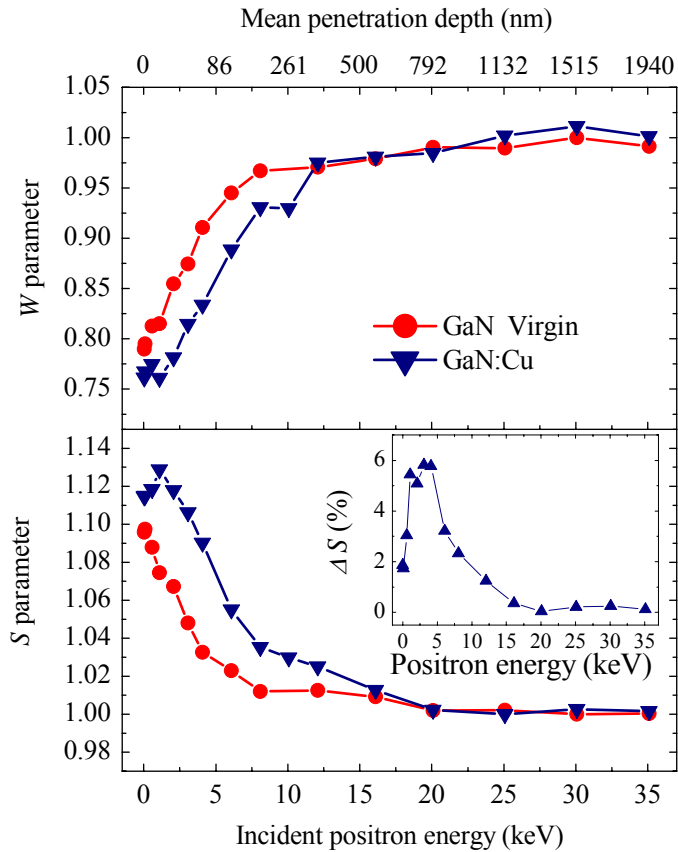


Fig. 7.6: Normalized Doppler broadening parameters as a function of the incident positron energy measured for the virgin and Cu-diffused GaN annealed up to 550 K samples. The low momentum parameter S is shown in the lower panel and W in the upper panel. The positron mean penetration depth is shown in the top axis. The inset in the lower panel displays the difference of S parameter between the Cu-diffused and virgin samples.

Doppler broadening measurements are described next. Figure 7.6 illustrates both S and W parameters measured as a function of the incident positron energy at RT in the virgin substrate and Cu-diffused GaN annealed up to 550 K samples, which shows the highest variation in lifetime data. S and W parameters are normalized to the corresponding values in bulk defect-free GaN S_b and W_b , respectively. As the positron energy increases, the S parameter in the virgin sample decreases from the surface specific value towards a constant value ($S/S_b \approx 1$) in the energy range 20-35 keV characteristic to bulk GaN. Conversely, the W parameter increases from the surface state to the bulk state. As mentioned above, the positron lifetime data for the virgin sample yield a single component lifetime of 154 ps. Thus, the Doppler broadening parameters recorded for this sample characterize the positron annihilation in defect-free GaN lattice. It is clearly shown that the annealed Cu-diffused GaN sample exhibits higher $S(E)$ and lower $W(E)$ curves than that of the reference in the positron energy range up to 16 keV (mean depth ~ 560 nm). This behavior can be explained by the presence of open-volume defects in this layer. An increase of 6 % in S at positron energy of 3 keV is observed. This can be ascribed to the appearance of vacancy clusters [208,209]. At positron energies higher than 16 keV both S and W are almost the same as in the virgin sample. The inset figure in the lower panel of figure 7.6 represents the difference between the S parameter of the Cu-diffused sample annealed at 550 K and that of virgin sample. It is evidently shown that there is a correlation between the behavior of ΔS and that of Cu profile measured by SIMS (figure 7.1).

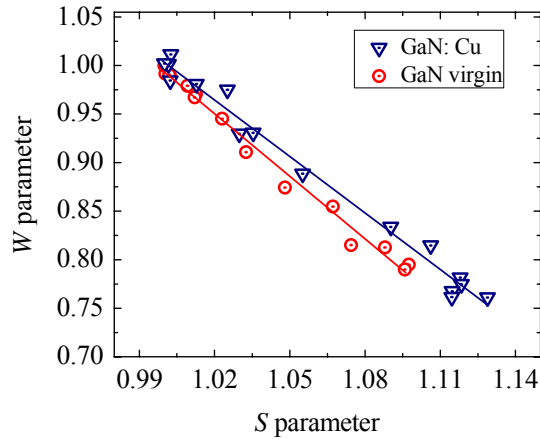


Fig. 7.7: W versus S plot for the slow positron beam measurement of the virgin and Cu-diffused GaN samples. The data are obtained from figure 7.6.

The number of different vacancy-type positron traps in the material can be studied by investigating the scaling relationship between S and W parameters. This is based on the fact that both S and W are sensitive to the defect concentration and defect types. If only a single type of vacancy is present, these parameters should vary linearly as a function of each other. Thus, the S - W linearity predominates only when the defect concentration (i.e., the fraction of positrons annihilating in the defect) changes [103,104]. For instance, V_{Ga} was observed in GaN [184,210], where all the (S,W) points were found to be on the same line in the S - W plane. If more than one defect type is responsible for positron trapping, a deviation from the S - W linear behavior would take place. The defect-free virgin sample shows only two positron annihilation states in the S - W plot, one at the surface and the other in the bulk. This means that a straight line is obtained between the surface and the bulk. In the case of Cu-diffused GaN, there are three distinct contributions to the annihilation process: annihilation in the Cu-treated region, annihilation at the surface, and annihilation in the bulk beyond Cu-treated region. S parameter is plotted versus W parameter in figure 7.7. It emerges from this plot that the observed $S(E)$ and $W(E)$ curves in Cu-diffused GaN are due to the appearance of a defect-type with larger open-volume, since two different straight lines are found. The positron lifetime experiments on this sample demonstrate a relatively large component of 433 ps. Thus, one can conclude that the increase of S and decrease of W correspond to vacancy clusters. Combining the results of SIMS and positron beam experiments, one can deduce that the defects are observed in the same layer where Cu is present. Therefore, it is reasonable to assume that Cu is responsible for the detected defects perhaps during its out-diffusion as suggested above. The observation of Cu in a depth of 600 nm after annealing for 96 h at 873 K projects a very low diffusion coefficient of Cu in GaN in contrast to other semiconductors, e.g. Si, Ge and GaAs. However, the mean penetration depth of positrons in GaN is $\sim 40 \mu\text{m}$ [79], which is much larger than the 600 nm thick Cu-diffused layer that contains the formed vacancy-like defects. This may explain the small intensity of the observed defect-related lifetime component, as mentioned above. Thus, the small effect observed in the lifetime is more likely due to the fact that the positrons penetrate much deeper than 600 nm, where only 1.5 % of positrons are stopped. It is reasonable that the value of τ_1 is almost τ_b , where most of positrons, 98.5 %, are annihilating beyond the Cu-diffused layer, i.e. in the defect-free region. The defect concentration is roughly estimated to be higher than 10^{18} cm^{-3} .

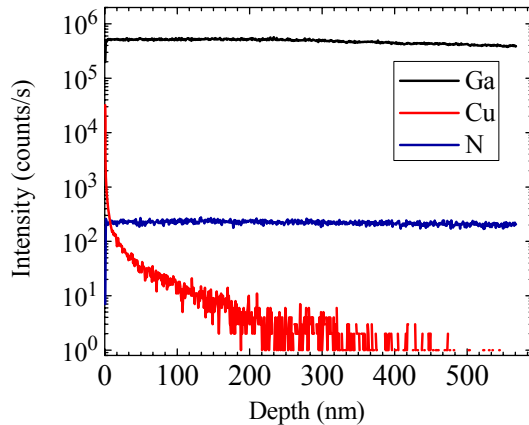


Fig. 7.8: SIMS depth profiles of Cu-diffused GaN sample after annealing at 850 K. Note that surface peaks are artifact of the SIMS measurements.

Note that no significant amount of Cu is observed after annealing at the highest temperature as shown in figure 7.8 displaying the SIMS profiles of Cu-diffused GaN sample after annealing at 850 K, which is in apparent contrast to the as-quenched sample showing the existence of Cu up to 600 nm (figure 1). This difference between the Cu profiles measured by SIMS in the as-quenched sample and that isochronally annealed at 850 K provides clear evidence of Cu out-diffusion. This measurement supports the suggestion that Cu out-diffusion may create vacancy-like defects observed by positron annihilation spectroscopy.

7.4 Conclusion

In summary, a first-of-a-kind study of Cu diffusion-induced vacancy-like defects in bulk GaN is represented in this work. Positron annihilation spectroscopy and secondary ion mass spectrometry were applied to investigate defects generated during thermal treatments of Cu-diffused fs-GaN samples. The average lifetime increases slowly during the subsequent post-annealing up to 550 K suggestive of the creation of vacancy-type defects. At this annealing temperature, a long lifetime component of 433 ps, attributed to vacancy clusters, with low intensity was observed. With a further increase in the annealing temperature, a decrease in the average positron lifetime was detected. It can be ascribed to defect healing or to larger vacancy clusters separated from each other by a distance larger than the positron diffusion length. The effect of Cu was evidenced by probing GaN samples annealed under very similar conditions but without Cu treatment. In the absence of Cu, the average lifetime is found to decrease slightly (≤ 1 ps) by increasing annealing temperature. The slow positron beam measurements showed that the vacancy clusters extend over a depth of 600 nm, which coincides with Cu profile as shown by SIMS, which support the claim that these defects are related to Cu out-diffusion. Unveiling the exact mechanistic picture of this phenomenon would, however, require extensive calculations to elucidate the atomic processes underlying the formation of vacancy and vacancy cluster upon thermal treatment of Cu-treated GaN.

8. Observation of As Vacancies during Zn diffusion in GaAs

The Zn diffusion from the vapor phase into n -doped GaAs is used to fabricate p - n junctions and heterojunctions [211]. Diffusion of zinc or other dopants in GaAs can be used in order to produce the disordering of the heterostructure and consequently the structure of the quantum well devices based on GaAs heterostructures [44]. From technological point of view, Zn is one of the most generally used p -type dopants for device fabrication in GaAs substrates and for disordering GaAs/AlGaAs superlattice layers. Zn is a very fast diffuser in GaAs, and it is commonly accepted that it diffuses by means of the kick-out mechanism [51,212].



Zn_i , Zn_{Ga} and I_{Ga} stand for interstitial Zn, substitutional Zn and Ga self-interstitials, respectively. The charge state is indicated by the corresponding superscripts. Eq. 8.1 indicates that a positively charged Ga interstitial species is assumed to be the point defect governing Ga self-diffusion. Ga self-interstitial contributing in the reaction 8.1 was previously suggested to be neutral [13]. A contribution of $\text{I}_{\text{Ga}}^{3+}$ in addition to $\text{I}_{\text{Ga}}^{2+}$ was proposed by Bösker et al. [213]. It is well recognized that Zn is an interstitial-substitutional species. Interstitial Zn atoms are not strongly bonded to the GaAs lattice and can hence leave their sites quick. Substitutional Zn atoms, as group II elements, are shallow acceptors occupying the Ga sublattice sites. The concentration change of the substitutional Zn is achieved by the fast migration of the interstitial Zn atoms and their subsequent exchange to occupy Ga sites. One native point defect, at least, is needed for this changeover. The Ga self-interstitial plays this role in accordance with the kick-out mechanism, as indicated in Eq. 8.1. It was early assumed that Zn diffuses via Longini mechanism [214], which can be described as:



In the latter mechanism, Ga vacancy V_{Ga} is the native point defect which is responsible for the changeover process. Zn solubility or thermal equilibrium concentration depends on Fermi level position, As vapor pressure P_{As_4} , Zn vapor pressure P_{Zn} in addition to the temperature. Zn atoms are provided to the GaAs material from the vapor phase Zn_v through the reaction:



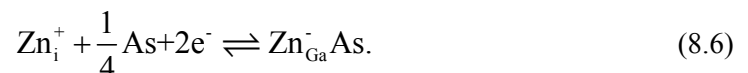
The thermal concentration of Zn_i^+ is given as:

$$C_i^{\text{eq}} = \left(\frac{P_{\text{Zn}_v}}{B_{\text{Zn}_v}} \right) \left(\frac{p}{\sqrt{N_c N_v}} \right) \exp \left(- \frac{g_i^f}{k_B T} \right), \quad (8.4)$$

where N_c and N_v denote the effective density of states in conduction and valence bands, respectively. g_i^f is the Zn_i^+ free energy of formation in GaAs. B_{Zn_v} is the Zn vapor phase ideal gas pressure constant expressed as:

$$B_{\text{Zn}_v} = \left(\frac{2\pi m}{h^2} \right)^{3/2} (k_B T)^{5/2}. \quad (8.5)$$

m stands for the Zn atom mass. The following reaction holds for the solubility of Zn_{Ga}^- ,



The thermal equilibrium concentration of Zn_{Ga}^- is then expressed by

$$C_s^{eq} = \left(\frac{P_{Zn_v}}{B_{Zn_v}} \right) \left(\frac{P_{As_4}}{B_{As_v}} \right)^{1/4} \left(\frac{\sqrt{N_c N_v}}{p} \right) \exp \left(- \frac{g_s^f - g_{As}^b}{k_B T} \right), \quad (8.7)$$

where B_{As_4} is the ideal gas pressure constant of As_4 . g_s^f represents the Zn_s^- free energy of formation. g_{As}^b is the free energy difference of one As atom in GaAs and in As_4 and given by $g_{As}^b = g_{As}^b(GaAs) - g_{As}^b(As_4)$.

Assuming that local equilibrium between the species involved in reaction (8.1) holds, it can be described by:

$$\frac{C_i}{C_s C_1} = \frac{C_i^{eq}(S)}{C_s^{eq}(S) C_1^{eq}(S)} = K \quad (8.8)$$

K is the reaction constant. $C_1^{eq}(S)$ is C_1^{eq} estimated at the sample surface with C_1^{eq} being the thermal equilibrium concentration of I_{Ga}^{2+} as determined by the local p value by the Fermi-level effect [51]. The diffusion equations for the two mobile species are:

$$\frac{\partial C_i}{\partial t} = \frac{\partial}{\partial x} \left(D_i \frac{\partial C_i}{\partial x} - D_i \frac{C_i}{p} \frac{\partial p}{\partial x} \right) - \frac{\partial C_s}{\partial t}, \quad (8.9)$$

and

$$\frac{\partial C_1}{\partial t} = \frac{\partial}{\partial x} \left(D_1 \frac{\partial C_1}{\partial x} - D_1 \frac{C_1}{p} \frac{\partial p}{\partial x} \right) - \frac{\partial C_s}{\partial t}. \quad (8.10)$$

The electric field produced by the charge distribution is taken into account through the second terms in the parentheses of Eqs. 8.9 and 8.10. C_1 denotes the concentration of I_{Ga}^{2+} , C_i is the concentration of Zn_i^+ and C_s is the concentration of Zn_{Ga}^- . D_i and D_1 stand for the diffusion coefficients of Zn_i^+ and I_{Ga}^{2+} .

For Zn in-diffusion experiments, an external source material is used to produce suitable vapor phases, which consecutively diffuse Zn into the samples under consideration. In case of out-diffusion, the samples with Zn pre-introduced are annealed in an ambient containing no Zn source material.

The observed Zn in-diffusion profiles [51,212] do not follow the complementary error function shape. Some of these profiles showed a kink-and-tail structure, this profile could be only simulated by modification the diffusion equations of the mobile species taking into account the effect of extended defect formation concomitant with the development of these profiles. Associated with this profile type, the formation of voids and interstitial-type dislocation loops has been identified [215]. These defects are formed principally in the very high Zn concentration region, from the GaAs surface down to the kink position.

Zn diffusion in GaAs, unlike Zn diffusion in Si which follows kick-out mechanism, commonly creates dislocations, precipitates and voids in high density [213]. Transmission electron microscopy (TEM) investigations indicated that the formation of these extended defects is initiated by the I_{Ga}^{2+} supersaturation [56,215] owing to Eq. (8.1).

It was suggested that this is caused by the high C_1 supersaturation produced by the extremely high Zn_{Ga}^- incorporation rate which leads to dislocation formation, which leads consequently to void formation [40]. As a result of these voids, the local values of C_1 will be

reduced reaching that of C_1^{eq} . It is reported that this profile type can be formed when C_s exceeds $\sim 5 \times 10^{19} \text{ cm}^{-3}$ with a diffusion depth exceeding $\sim 15 \mu\text{m}$ [216].

Zn has a much higher diffusion coefficient under in-diffusion conditions than under out-diffusion conditions [51]. For in-diffusion, Zn_i^+ rapidly migrates into GaAs and changes over to become Zn_{Ga}^- and thus creates an $\text{I}_{\text{Ga}}^{2+}$. The relative magnitude of Zn_i^+ in-diffusing and $\text{I}_{\text{Ga}}^{2+}$ out-diffusing rates play a major role for building up $\text{I}_{\text{Ga}}^{2+}$ supersaturation. The Zn_{Ga}^- diffusivity increases by the presence of high $\text{I}_{\text{Ga}}^{2+}$ supersaturation. Under out-diffusion conditions, the rapid diffusion of Zn_i^+ from the sample interior to the surface quickly reduces its concentration in the sample interior where the C_s value of the pre-introduced Zn_{Ga}^- has not approximately changed. Since Eq. (8.8) is still holding, a large $\text{I}_{\text{Ga}}^{2+}$ undersaturation is yielded, which prevent the occurrence of $\text{Zn}_{\text{Ga}}^- \rightarrow \text{Zn}_i^+$ changeover with high efficiency in the sample inside. This leads to a tremendously decreasing of the Zn_{Ga}^- diffusivity.

8.1 Experimental

Rectangular samples, $5 \times 7 \text{ mm}^2$ in size, were cut from semi-insulating undoped LEC grown GaAs wafer of $465 \mu\text{m}$ thickness, cleaned and enclosed in an evacuated quartz ampoules of 9 cm^3 volume. 10 mg As was added to build up an As_4 partial vapor pressure. 3 mg elemental Zn is added as a diffusion source. Diffusion annealing was performed at $950 \text{ }^\circ\text{C}$ for 2 hours. The temperature was monitored with an accuracy of $\pm 1 \text{ K}$. The diffusion process was terminated by plunging the ampoule into water at room temperature. An ion image was detected with TOF secondary ion mass spectrometry in positive ion polarity using a O_2^+ sputter source (2 keV) with a measuring area of $500 \times 500 \mu\text{m}^2$ and a sputter area of $700 \times 700 \mu\text{m}^2$ each time. The conventional positron lifetime and Doppler broadening using a slow positron beam were applied. The as-quenched samples were measured then by stepwise etching in steps of $7 \mu\text{m}$. After each etching step the samples were measured by both Doppler broadening and lifetime spectroscopy.

8.2 Results and discussion

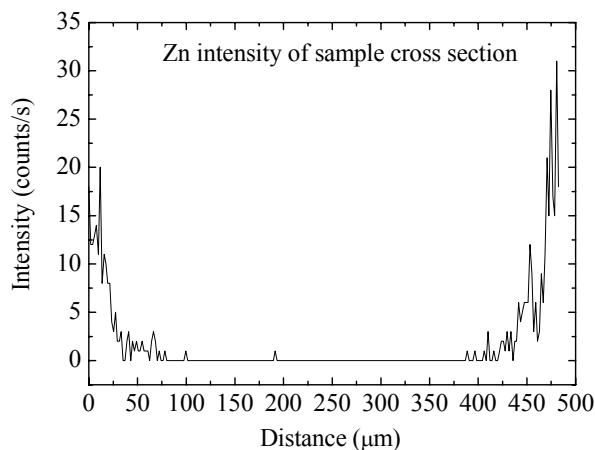


Fig. 8.1: Ion image for the as-quenched Zn-diffused SI GaAs measured by TOF-SIMS. Zn diffusion was performed from both surfaces of the sample for 2h at $950 \text{ }^\circ\text{C}$. The diffusion is terminated by quenching the sample in RT water. The SIMS measurement was performed on the cleaved sample with a measuring area of $500 \times 500 \mu\text{m}^2$.

The ion image measured by SIMS for the Zn diffused GaAs shows the presence of Zn in a considerable amount up to 45 μm approximately, as shown in Fig. 8.1. It is shown also that the Zn concentration decreases in the GaAs matrix with increasing the depth below the surface. The Zn diffusion has taken place from both surfaces of the sample.

SIMS measurement was carried out along the cleavage plane. This is the reason for the observation of Zn on both sides of the sample. It should be noted that these measurements were not calibrated. $S(E)$ positron depth scans were performed for the reference material and the Zn-diffused sample after each etching step. The maximum positron energy is 28 keV, which corresponds to a mean depth of 1.75 μm . Thus, the information depth of positrons in the beam system is much too small to investigate the Zn diffused layer at once. Therefore, the sample surface was stepwise ($7\pm 1\mu\text{m}$) detached by chemical etching. A positron depth scan was performed after each etching step. Thereafter, the whole defect depth profile generated by Zn diffusion down to the surface was restructured from the individual slow positron measurements.

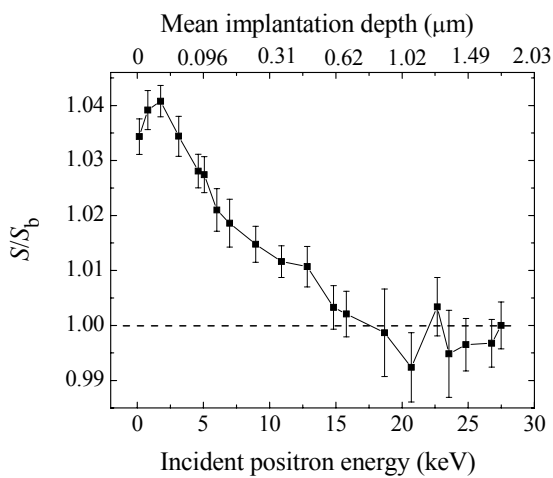


Fig. 8.2: Low momentum (S) parameter as a function of the incident positron energy in SI GaAs reference sample.

Figure 8.2 shows the $S(E)$ curve for the reference sample. The sample shows a weak structure for low energies. This can be attributed to the surface damage during the wafers cutting [217]. The increase of the curve in the energy range up to about 2 keV is owing to the surface S parameter. Positrons implanted into a small depth may diffuse back to the surface. The resulting S parameter is a superposition of positron annihilation in the surface state, defects and possibly of the bulk. At positron energies higher than 20 keV, the S parameter is almost constant, it thus was used as the defect-free reference value S_b for the normalization of all other measurements. The positron diffusion length becomes smaller if the defect concentration is higher. This leads to a steep increase of the $S(E)$.

Figure 8.3 shows the individual depth scans of the Zn-diffused GaAs sample after each etching step. The as-quenched sample (0 μm etching) shows lower values of S parameter at lower positron energies due to the surface defects present in the initial samples (before Zn diffusion). In contrast to the reference sample (Fig. 8.2), S parameter increases with increasing the incident positron energy. This high S parameter is due to the existence of open-volume defects. $S(E)$ curves were measured again after seven etching steps as shown in Fig. 8.3. With increasing the etch depth S value increases and then saturates at a depth of 28 μm and then slightly decreases. A steep decrease of S parameter is observed at 41 μm reaching the bulk value. This indicates the presence high defect concentration up to 41 μm below the sample surface. The bulk value of both the S parameter and the diffusion depth is reached after 41 μm etching. This means that no positron traps

are detected beyond 42 μm , where S parameter is still higher than that of the bulk up to 10 keV of the positron beam energy after this etching step.

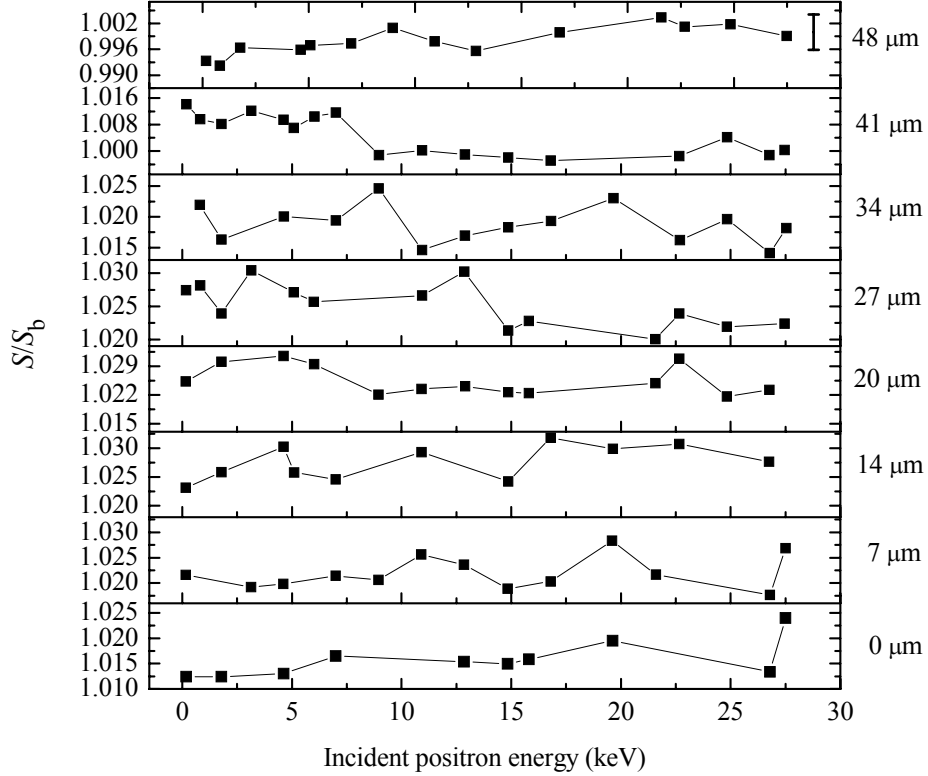


Fig. 8.3: Investigation of defects generated by Zn diffusion in SI GaAs. The S parameter is presented as a function of the incident positron energy for the as-quenched sample and after stepwise etching for the same sample. The thickness of the layer removed by etching is shown on the right side of the figure.

The reconstruction of the overall defect profile is carried out as displayed in Fig. 8.4. The S parameter is plotted as a function of the depth, which is calculated from the incident positron energy (E) according to Eq. 4.3. The values of the empirical parameters, A and r , for GaAs are $3.32 \mu\text{g cm}^{-2} \text{keV}^{-r}$ and 1.7, respectively [217]. $\rho = 5.316 \text{ g cm}^{-3}$ for GaAs is used. The whole S parameter profile in Fig. 8.4 was assembled from all $S(E)$ curves of Fig. 8.3 obtained in the as-quenched state and after each etching step. S parameter at the maximum energy is considered in this plot. The etch depths were taken into consideration for the assembling of the curve, i.e. the complete positron depth profile, e.g. after the first etching step, was shifted 6 μm to the right. As mentioned above, the lower values of S parameter in the first μm is due to the presence of the defects in this layer before the diffusion experiment. The low-energy parts of the separate $S(E)$ curves are influenced by the low surface S parameter. These parts of the curves must be ignored when constructing the whole $S(E)$ depth profile. The defect depth is determined as the depth of the intersection point of the solid line with the defect-free reference level (dashed line in Fig. 8.4). The S parameter profile (Fig. 8.4) can be used to estimate the defect concentration as a function of depth, i.e., the open-volume defect profile. The defect concentration is calculated using the relation ($C_d = \kappa_d / \mu = (S - S_b) / ((S_{\text{def}} - S)(\mu \cdot \tau_b))$). Where τ_b is the bulk lifetime, 228 ps for GaAs. S_{def} denotes the S parameter in case of saturated positron trapping in the defect. μ is taken as 10^{15} s^{-1} at 300 K in these calculations [130].

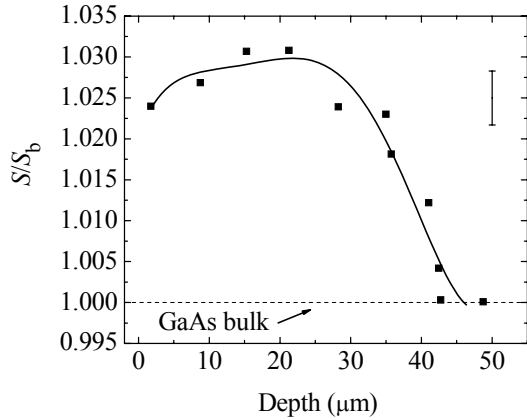


Fig. 8.4: S parameter plotted as a function of the depth from the sample surface. The curve was compiled from the individual $S(E)$ curves measured for the as-quenched sample and after each etching step for the same sample (Fig. 8.3). The etch depths were considered as appropriate rightward shifts. The S parameter approaches the reference level at a depth of 41 μm . Therefore, this value represents the defect layer. The solid line is plotted as a smoothed curve to guide the eye.

The calculated defect profile is shown as a plot of the trapping rate and defect concentration versus depth in Fig. 8.5. The defect-related S parameter was supposed to be $S_{\text{def}} = 1.0318$, which represents the maximum value in the $S(E)$ plot (Fig. 8.3). As always when saturated positron trapping is observed, only a lower limit of the trapping rate can be obtained.

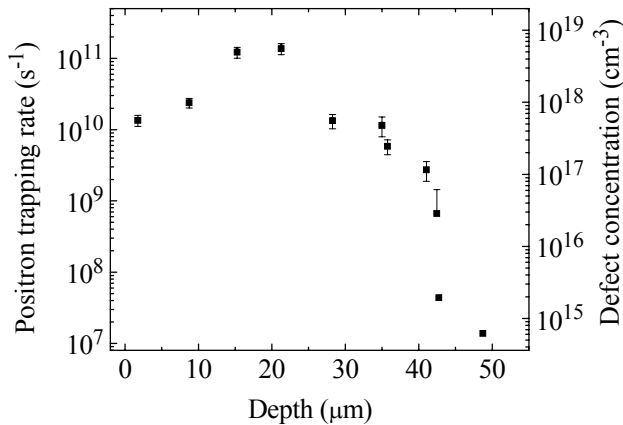


Fig. 8.5: Defect profile as obtained by positron annihilation in Zn-diffused SI GaAs. The positron trapping rate is plotted as a quantity proportional to the defect concentration as a function of the depth.

The positron lifetime measurements were performed on the as-quenched Zn-diffused GaAs after each etching step. The results are shown in Fig. 8.6. The as-quenched sample showed the maximum average positron lifetime. τ_{av} decreases with decreasing the sample temperature which is a typical dependence of the shallow positron traps. Here after Zn diffusion, Zn acts as shallow acceptors. All curves show the same behavior. With increasing the etching depth the average lifetime decreases which indicates the decrease of the defect layer thickness.

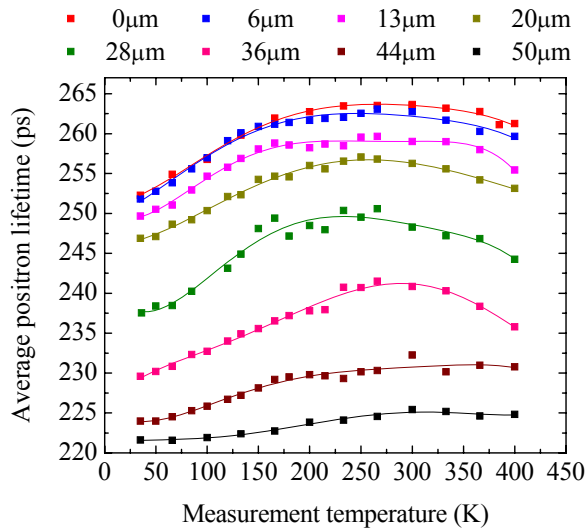


Fig. 8.6: Temperature dependence of the average positron lifetime in Zn-diffused GaAs. The measurement is repeated after each etching step for the same sample as shown in the figure.

The overall average lifetime depth profile was derived from data in Fig 8.6 at 300 K. It is shown in the lower panel of Fig. 8.7. It is clearly shown that τ_{av} decreases as the etch depth increases. The thickness of the defect layer is determined to be $\sim 45 \mu\text{m}$.

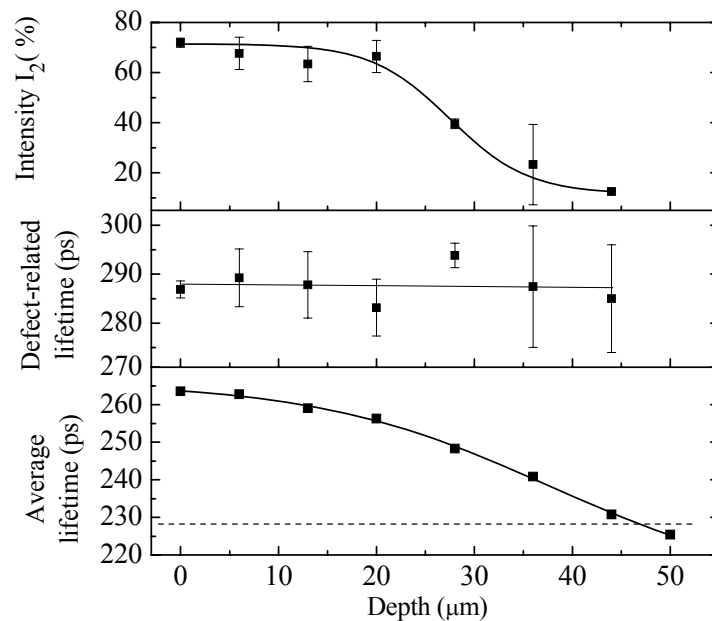


Fig. 8.7: Average and defect-related positron lifetimes and its relative intensity in Zn diffused GaAs as a function of the depth below the surface. The profile was assembled from the individual measurements for the as-quenched sample and after each etching step for the same sample measured at 300 K. The etch depths were taken into account as appropriate rightward shifts. τ_{av} approaches the reference level at a depth of $45 \mu\text{m}$.

Both positron beam and lifetime measurements indicate the existence of defects in a layer of about $42 \mu\text{m}$. Combining positron annihilation spectroscopy and SIMS measurement, one can observe that the open-volume defects are detected where Zn is present in the sample. The decrease of τ_{av} is due to the decrease of fraction of positrons annihilating in the defect layer, since the defect layer decreases with increasing the etch depth. The fraction of positrons which stops in the defect layer can be estimated from the relation $P(x) = 1 - e^{-\alpha x}$ [218]. The stopped fraction P is an

exponential function of the depth x . $\alpha(\text{cm}^{-1}) = 17 \cdot \rho(\text{g/cm}^3) / E_{\text{max}}^{1.43}(\text{MeV})$. It is clearly shown that the fraction of positrons annihilating in the defect layer decreases as the etching depth increases. This leads to the decrease of the average lifetime because the positrons fraction annihilating in the defect-free layer increases. This can be shown from the decrease of the intensity of the defect-related lifetime in the upper panel of Fig. 8.7. Once the defect layer is removed by etching at a depth of $\sim 45 \mu\text{m}$ positrons annihilate reflecting thereby the defect-free lifetime of GaAs bulk material.

The value of the first lifetime component is always less than that of the bulk defect-free sample. The defect-related lifetime is 287 ± 3 ps according to the fitting of the data as shown in the middle panel of Fig. 8.7. It is higher than that of V_{Ga} (267 ps) [101] but it is still much lower than that of $V_{\text{Ga}}-V_{\text{As}}$ (332 ps) [101]. It cannot be the isolated V_{As} too, since V_{As} is positively charged and thus not detectable by positrons in SI or p -type GaAs [93]. It is also reported theoretically that the arsenic vacancy is always positive in SI or p -type GaAs and thus it should be invisible for positrons [79]. The observed experimental defect-related lifetime (287 ± 3 ps) is higher than that of the isolated V_{As} (266 ps) [101]. This reflects that the detected lifetime values correspond most probably to V_{As} defect complex. $V_{\text{As}}-\text{Si}_{\text{Ga}}$ complexes were identified in Si-doped GaAs with corresponding defect-related lifetime of 283 ± 8 ps [219]. The observed defect can be expected to be the $V_{\text{As}}-\text{Zn}_{\text{Ga}}$ complex.

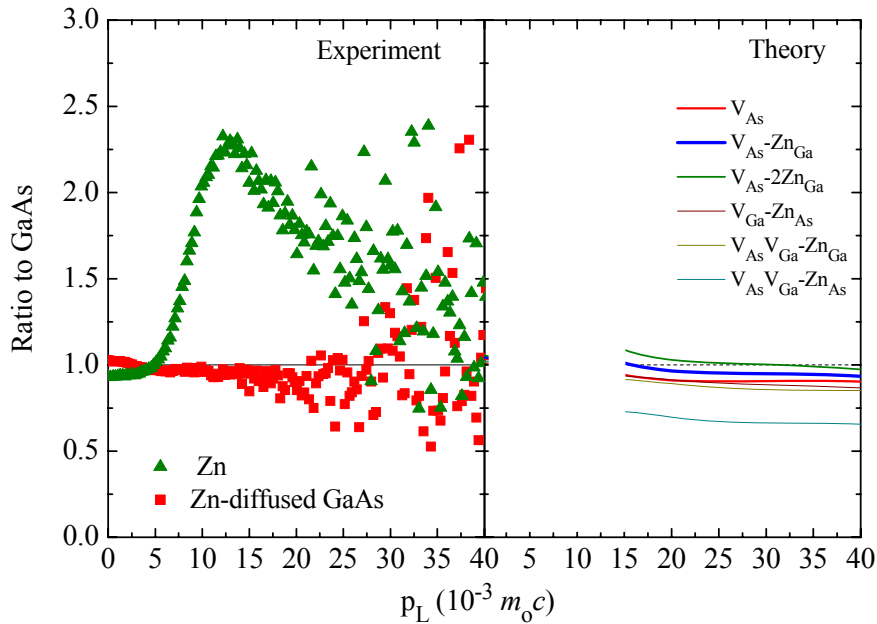


Fig. 8.8: Results of Doppler broadening spectroscopy of Zn-diffused SI GaAs (as-quenched) and pure Zn samples. All ratio plots are normalized to SI GaAs reference sample (left part). Ratio of the momentum density to bulk GaAs for different vacancies and vacancy complex in GaAs are theoretically calculated (right part). The curve for $V_{\text{As}}-\text{Zn}_{\text{Ga}}$ is in agreement with that measured in Zn-diffused GaAs. The theoretical curves are not accurate for $p_L < 15 \times 10^{-3} m_0 c$ Ref. [105] and hence are omitted.

To get more detailed information about the monovacancy under investigation, Zn-diffused GaAs as-quenched sample as well as SI GaAs and Zn reference materials were measured by the CDBS technique. The results are shown in the left panel of Fig. 8.8. The curve of Zn-diffused GaAs is surprisingly similar to that of the GaAs reference sample, although most of positrons are trapped in a vacancy-type defect. The same situation was observed in case of Zn diffusion in GaP, in which a $V_{\text{P}}-\text{Zn}_{\text{Ga}}$ complex was detected [220]. It should be taken into account that in GaAs which is

profoundly in the degenerated state after doping with about 10^{19} cm^{-3} Zn acceptors, the isolated As vacancy can only be in the positive charge state. The scattering of the Zn-diffused GaAs curve in the high momentum region, as shown in Fig. 8.8 (left panel), is indicative of the presence of Zn in the vicinity of the observed open-volume defects. Most likely the positron trapping center is the $V_{\text{As}}\text{-Zn}_{\text{Ga}}$ defect, which can be neutral or negatively charged and thus observable by positrons. The momentum density for vacancies and vacancy complexes in GaAs is calculated using the method described above (Sect. 6.4). The results are plotted in the right panel of Fig 8.8. The theoretically calculated curves for p_L below $15 \times 10^{-3} m_0 c$ are not precise and therefore are neglected. The isolated V_{As} curve is lower than the Zn-diffused measured one, whereas the curves of V_{As} surrounded with Zn atoms is very close to it. However, this indicates the existence of Zn in the near vicinity of V_{As} forming complexes. The curve of V_{As} surrounded with one Zn atom is very close to that of Zn-diffused GaAs. Thus, the detected defect is most likely $V_{\text{As}}\text{-Zn}_{\text{Ga}}$. Moreover, the calculated defect-related lifetime for that complex in unrelaxed structure is 274 ps. It is 13 ps smaller than the measured value (287 ps). The difference could be attributed to the occurrence of relaxation, which was not taken into account in the calculation.

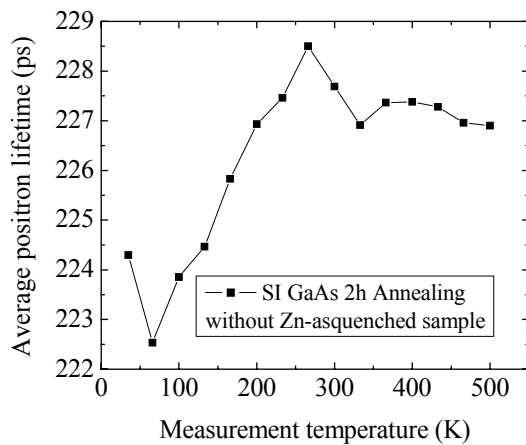


Fig. 8.9: Average positron lifetime as a function of sample temperature in SI GaAs. The sample was annealed without Zn addition for 2h at 950 °C. Only 10 mg As was added. The annealing is terminated with quenching the sample in water. The sample is thus a reference experiment to the results shown in Fig. 8.6.

To show that the observed defect is Zn diffusion-related, SI GaAs samples were annealed under the same condition but without Zn then quenched into RT water. Temperature-dependent positron lifetime measurements were carried out on the as-quenched sample. The results are plotted in Fig. 8.9. As illustrated in the figure, the sample shows just the defect-free bulk lifetime value, 228 ps. The decrease of the lifetime in the low temperature region is due to the positron trapping into shallow traps. It was suggested that residual impurities (e.g. C_{As}^-) and native defects such as the gallium antisite defect, Ga_{As}^- , are responsible for the formation of negative centers acting as shallow traps for positrons in undoped GaAs [88,89]. In contrast, an average lifetime value of 264 ps is detected in the as-quenched Zn-diffused GaAs sample (Fig. 8.6). In fact, the absence of the vacancy signal in the sample treated without Zn indicates clearly that the observed defects are accompanied to Zn diffusion.

8.3 Conclusion

Positron annihilation spectroscopy as well as SIMS was applied to study the defect depth profile and to identify the generated defects in Zn-diffused SI GaAs samples, where the diffusion is done by annealing the samples for 2h at 950 °C. The samples were etched in steps of 7 μm . Both lifetime and Doppler broadening using slow positron beam spectroscopy studies were performed after each

etching step. Both techniques showed the existence of vacancy-type defects in a layer of about 45 μm . SIMS measurements illustrate the presence of Zn at high level in the sample almost up to the same depth. Vacancy-like defects as well as shallow positron traps (negatively charged non-open volume defects) were observed by lifetime measurements. Zn acceptors in addition to the impurities explained the observation of shallow traps. The behavior of the temperature-dependent average positron lifetime can be ascribed to thermally assisted positron detrapping from these shallow traps. The average lifetime was found to decrease with increasing etching depth. This is because the decrease of the thickness of defect layer, which decreases the fraction of positrons annihilating in the open-volume defects. The effect of Zn for the defect generation was proved by annealing SI GaAs samples under very similar conditions but not treated with Zn. A defect-free bulk lifetime value is detected in this sample. The observed defect is more probably an As vacancy bound to a Zn acceptor, which is not positively charged and thus visible by positrons.

9. Summary

The defect properties in III-V compound semiconductors, GaAs and GaN, introduced during Cu and Zn diffusion were studied in this thesis. These materials are used in optoelectronic devices, such as light emitting diodes and semiconductor laser structures. GaAs is also utilized in the fabrication of high-frequency electronic devices and solar cells. These compounds have superior features relative to conventional semiconductors, e.g. silicon, considering that they have a direct band gap whereas silicon has an indirect band gap. The formation of equilibrium vacancy-type defects was investigated by positron annihilation lifetime spectroscopy (PALS) and coincidence Doppler broadening spectroscopy (CDBS). The defect profile was determined by means of variable energy positron annihilation spectroscopy (VEPAS). Generally, no method is currently available that would allow the independent identification of vacancies. The combined analysis of data from positron lifetime and coincidence Doppler spectroscopy in comparison with calculated annihilation parameters is utilized for the identification of the vacancy-type defects.

Results from this research pointed out the following conclusions:

- 1) Vacancy-like defects and shallow positron traps (negatively charged non-open volume defects) were observed; observed shallow traps in Cu-diffused GaAs samples were attributed to copper acceptors, which is confirmed by temperature-dependent Hall-effect measurements. Zn acceptors play the same role in case of Zn-diffused GaAs.
- 2) V_{As} -like defects were observed in semi-insulating GaAs after Cu in-diffusion on the basis of PALS and thermodynamic consideration. These defects are not bound to Cu atoms according to the CDBS findings. This defect complex is assumed to be a native defect complex, of which structure could not be exactly determined based solely on the positron annihilation parameters. Arsenic vacancy complexes were detected previously in Si-doped GaAs [219], where $V_{As}-Si_{Ga}$ complexes were found to be responsible for positron trapping.
- 3) $V_{As}-Cu_{Ga}$ complexes were hypothesized to be responsible for the observed defects in Zn-doped GaAs after Cu in-diffusion, where CDBS showed the existence of Cu in the near vicinity of V_{As} -like defects.
- 4) PALS has detected vacancy-like defects in Cu-diffused Te-doped GaAs samples. These defects were found to be bound to Cu impurities. $V_{Ga}-Cu_{Ga}$ complexes were predicted theoretically to account for these results. Cu out-diffusion was assumed to be responsible for the observed vacancy-type defects. The observation of V_{Ga} complex is in agreement with previous experimental studies where Ga vacancies during Cu out-diffusion in GaAs [70] were observed forming complexes.
- 5) The different complexes observed in Cu-diffused semi-insulating, Zn- and Te- doped GaAs are most likely due to the metallurgical effect of dopants in interaction with Cu and Vacancies forming the complexes.
- 6) The positron trapping model was used to calculate the concentration of shallow traps. The calculated value was found to be in good agreement with that measured using Hall-effect.
- 7) A binding energy of $E_b = (79.4 \pm 6)$ meV for localized positrons in shallow traps in Cu-diffused Te-doped GaAs was determined from the analysis of the lifetime in terms of detrapping from shallow traps with a value comparable to calculated one. The trapping coefficient of positrons to shallow traps at 29 K in these samples was estimated to be

$3.2 \times 10^{16} \text{ s}^{-1}$. These values are in agreement with those determined in Si-doped GaAs using positron annihilation spectroscopy and scanning tunneling microscopy [96].

- 8) The formation of the open-volume defects in GaAs was found to depend on the stoichiometry of the GaAs system, for instance, a larger amount of excess arsenic was found to support the creation of vacancy clusters in *n*-type GaAs. This is consistent with the dependence of vacancy concentration on arsenic vapor pressure observed in semi-insulating undoped and Si-doped GaAs [93,134].
- 9) A lifetime component corresponding to vacancy clusters with a low intensity was observed by PALS in Cu-diffused free-standing GaN samples. Slow positron beam measurements demonstrated that the vacancy clusters extend over a depth of 600 nm, coinciding with a Cu profile as measured by secondary ion mass spectroscopy, and which supports the assumption that these defects are related to Cu out-diffusion. The small diffusion depth (i.e. small defect layer) accounts for the small intensity of the longer lifetime component. The first study of Cu diffusion in GaN is presented in this work with results pointing to a low diffusion coefficient of Cu in this compound relative to other semiconductors.
- 10) The defect depth profile in Zn-diffused semi-insulating GaAs was obtained by Doppler broadening using slow positron beam spectroscopy and PALS. Both techniques illustrated the existence of vacancy-type defects in a layer of about 45 μm . SIMS measurements showed the presence of Zn in the sample almost up to the same depth. The observed defect was assumed to be $V_{\text{As}}\text{-Zn}_{\text{Ga}}$ in accordance with the lifetime and CDBS results. These results are in comply with previous studies which indicated the occurrence of supersaturation of arsenic vacancies during Zn diffusion in GaAs [215]. The higher defect density ($\sim 10^{19} \text{ cm}^{-3}$) determined by slow positron measurements confirms the occurrence of such defect supersaturation.
- 11) The effect of either Cu or Zn was evidenced by probing reference samples. They were annealed under very similar conditions but not treated with Cu or Zn, respectively. The behavior of PALS results were found to be in clear contrast to the data of Cu- or Zn-diffused samples.
- 12) The lateral resolution of the slow positron beam was determined at the sample position to be 4 mm.
- 13) It can be concluded that the obtained results of positron annihilation spectroscopy showed no vacancies after Cu in-diffusion in GaAs which agree well with kick-out diffusion mechanism, whereas during Cu out-diffusion, vacancies were observed which are not compatible to any of the equilibrium diffusion mechanisms. The results in Zn-diffused GaAs are in good agreement with kick-out mechanism although vacancies were detected since they are arsenic vacancies which are created to keep the crystal stoichiometry.
- 14) An attempt was made to understand the structure, occurrence and properties of vacancies during Cu diffusion in GaN. It would be of benefit to perform more detailed studies for determining Cu diffusion coefficient and confirming the mechanism which governs the process.
- 15) In the future, diffusion studies conducted in this work could be applied for other impurity atoms and compound semiconductors. It would also be of interest to study diffusion processes in ternary semiconductor compounds such as AlGa₃N and InGaP, which are currently hot research topics, taking into account developing some computer programs for diffusion simulation.

References

- [1] *Dictionary of Physics*, 3rd ed., edited by H. J. Grey and A. Isaacs (Longman, Singapore, 1991).
- [2] A. Einstein, *Annalen der Physik* **17**, 549 (1905).
- [3] A. Einstein, *Annalen der Physik* **19**, 371 (1906).
- [4] S. Yu, U. Gösele and T.Y. Tan, *J. Appl. Phys.* **66**, 2952 (1989).
- [5] R.S. Bhattacharya and P.P. Pronco, *Appl. Phys. Lett* **40**, 890 (1982).
- [6] W. Hayes and A. M. Stoneham, *Defects and Defect Processes in Nonmetallic Solids* (Wiley, New York, 1985).
- [7] B. Tuck, *Introduction to Diffusion in Semiconductor*, (Peter. Peregrinus Ltd., England, 1974).
- [8] J. Crank, *The Mathematics of Diffusion*, 2nd edn (Clarendon, Oxford 1975).
- [9] T.Y. Tan and U. Gösele, *Handbook of Semiconductor Technology*, Edited by K.A. Jackson and W. Schröter, Volume 1 (2000).
- [10] H.J. Wollenberger. In: *Physical Metallurgy*, part 2, ed by R.W. Cahn, P. Haasen (North Holland, Amsterdam 1996).
- [11] F.C. Frank and D. Turnbull, *Phys. Rev.* **104**, 617 (1956).
- [12] U. Gösele, W. Frank and A. Seeger, *Appl. Phys.* **23**, 361 (1980).
- [13] U. Gösele and F. Morehead, *J. Appl. Phys.* **52**, 4617 (1981).
- [14] U. Gösele, *Ann. Rev. Mat. Science* **18**, 257 (1988).
- [15] N.A. Stolwijk, W. Frank, J. Hölzl, S.J. Pearton and E.E. Haller, *J. Appl. Phys.* **57**, 5211 (1985).
- [16] G. Watkins, in: *lattice defects in semiconductors 1974*: Huntley, I. A. (Ed.). London: Inst. Phys. (Conf. Ser. 23), (1975).
- [17] R.N. Hall and J.H. Racette, *J. Appl. Phys.* **35** 379 (1964).
- [18] T.Y. Tan and U. Gösele, *Mater. Sci. Eng. B* **1**, 47 (1988).
- [19] W. Frank, U. Gösele, H. Mehrer and A. Seeger. In: *Diffusion in Crystalline Solids*, ed by G.E. Murch, A.S. Nowick, (Academic Press, New York 1984).
- [20] H. Bracht, N.A. Stolwijk and H. Mehrer, *Phys. Rev. B* **52**, 16542 (1995).
- [21] J.D. Weeks, J.C. Tully and L. C. Kimerling, *Phys. Rev. B* **12**, 3286 (1975).
- [22] L.C. Kimerling, *Solid-State Electron.* **21**, 1391 (1978).
- [23] G.D. Watkins, *Handbook of semiconductor technology*, Volume 1 (2000).
- [24] C.H. Chen, D.G. Yu, E.L. Hu and P.M. Petroff, *J. Vac. Sci. Technol. B* **14**, 3684 (1996)
- [25] M. Uematsu and K. Wada, *Appl. Phys. Lett.* **60**, 1612 (1992).
- [26] G. Lengel, M. Weimer, J. Gryko and R.E. Allen, *J. Vac. Sci. Technol. B* **13**, 1144 (1995).
- [27] P. Heitjans and J. Kärger, *Diffusion in condensed mater* (2005).
- [28] M.R. Brozel and G.E. Stillman, *Properties of GaAs*, third edition. London, INSPEC, The institution of Electrical Engineers (1996).
- [29] H. Wenzl, A. Dahlen, A. Fattah, S. Petersen, K. Mika and D. Henkel, *J. Cryst. Growth* **109**, 191 (1991).
- [30] H. Wenzl, W.A. Oates and K. Mika. *Handbook of Crystal Growth*. D.T.J. Hurler. Amsterdam, North Holland.(1994).
- [31] M. Jurisch and H. Wenzl. Thermochemische Modellierung der Abhängigkeit des spezifischen elektrischen Widerstandes von GaAs vom Kohlenstoff-Gehalt. DGKK Arbeitskreis "Angewandte Simulation in der Kristallzüchtung"- 2. Workshop, Memmelsdorf, Germany (2002).
- [32] J.R. Arthur, *J. Phys. Chem. Solids* **28**, 2257 (1967).

- [33] F. Kiessling (2003). Private communication.
- [34] D.T.J. Hurle, *J. Appl. Phys.* **85**, 6957 (1999).
- [35] F.A. Kröger, *The chemistry of imperfect crystals*. Amsterdam. North Holland Publishing Company (1964).
- [36] B. Tuck, *Atomic Diffusion in III-V Semiconductors* (Hilger, Bristol, 1988).
- [37] T.Y. Tan, H. M. You and U. M. Gösele, *Appl. Phys. A* **56**, 249 (1993).
- [38] T.Y. Tan, *J. Phys. Chem. Solids* **55**, 917 (1994).
- [39] V. Bondarenko (2003). Positron annihilation study of equilibrium point defects in GaAs. Halle (Saale), Martin Luther Universität.
- [40] T.Y. Tan, U. Gösele and S. Yu, *Crit. Rev. Sol. State Mater. Sci.* **17**, 47 (1991).
- [41] J.A. Van Vechten, *J. Electrochem. Soc.* **122**, 423 (1975).
- [42] G.A. Baraff and M. Schlüter, *Phys. Rev. Lett.* **55**, 1327 (1985).
- [43] J. Gebauer, M. Lausmann, F. Redmann, R. Krause-Rehberg, H. Leipner, E. Weber and P. Ebert, *Phys. Rev. B* **67**, 235207 (2003).
- [44] W.D. Laidig, H. Holonyak, Jr., M.D. Camras, K. Hess, J.J. Coleman, P.D. Dapkus and J. Bardeen, *Appl. Phys. Lett.* **38**, 776 (1981).
- [45] B. Goldstein, *Phys. Rev* **121**, 1305 (1961).
- [46] H.D. Palfrey, M. Brown and A.F.W. Willoughby, *J. Electrochem. Soc.* **128**, 2224 (1981).
- [47] T.E. Schlesinger and T. Kuech, *App. Phys. Lett.* **49**, 519 (1986).
- [48] T.Y. Tan and U. Gösele, *Appl. Phys. Lett.* **52**, 1240 (1988).
- [49] A. Furuya, O. Wada, A. Takamori and H. Hashimoto, *Jpn. J. Appl. Phys.* **26**, L926 (1987).
- [50] K.Y. Hsieh, Y.C. Lo, J.H. Lee and R.M. Kolbas, *Inst. Phys. Conf. Ser.* **96** 393 (1988).
- [51] S. Yu, T.Y. Tan and U. Gösele, *J. Appl. Phys.* **69**, 3547 (1991).
- [52] S. Yu, T.Y. Tan and U. Gösele, *J. Appl. Phys.* **70**, 4827 (1991).
- [53] T.Y. Tan, S. Yu and U. Gösele, *J. Appl. Phys.* **70**, 4823 (1991).
- [54] T.Y. Tan, H.M. You, S. Yu, U. Gösele, W. Jäger, D.W. Böringer, F. Zypman, R.Tsu and S.T. Lee, *J. Appl. Phys.* **72**, 5206 (1992).
- [55] L. Wang L. Hsu, E.E. Haller, J. W. Erickson, A. Fischer, K. Eberl and M. Cardona, *Phys. Rev. Lett.* **76**, 2342 (1996).
- [56] W. Jäger, A. Rucki, K. Urban, H.G. Hettwer, N.A. Stolwijk H. Mehrer and T.Y. Tan, *J. Appl. Phys.* **74**, 4409 (1993).
- [57] T.Y. Tan and U. Gösele, *Mater. Chem. Phys.* **44**, 45 (1995).
- [58] P. Mei, H.W. Yoon, T. Venkatesan, S.A. Schwarz and J.B. Harbison, *App. Phys. Lett.* **50**, 1823 (1987).
- [59] D.G. Deppe and N. Holonyak, *J. Appl. Phys.* **64**, R93 (1988).
- [60] P. Mei, S.A. Schwartz, T. Venkatesan, C.L. Schwartz and E. Colas, *J. App. Phys.* **65**, 2165 (1989).
- [61] T.Y. Tan and U. Gösele in; *Advances in Materials, Processing and Devices in III-V Compound Semiconductors*: D. K. Sadana, L. Eastman, R. Dupuis,(Eds.). Pittsburgh: Mater. Res. Soc. (Proc. 144), (1989).
- [62] D.G. Deppe, N. Holonyak and J.E. Baker, *Appl. Phys. Lett.* **52**, 129 (1987).
- [63] H. Palfrey, M. Brown and A. Willoughby, *J. Electr. Mater.* **12**, 863 (1983).
- [64] U. Egger, M. schultz, P. Werner, O. Breitenstein, T.Y. Tan, U. Gösele, R. Franzheld, M. Uematsu and H. Ito, *J. Appl. Phys.* **81**, 6056(1997).
- [65] M. schultz, U. Egger, R. Scholz, O. Breitenstein, T.Y. Tan and U. Gösele, *J. Appl. Phys.* **83**, 5295 (1998).
- [66] R. Scholz, U. Gösele, J. Y. Huh and T.Y. Tan, *Appl. Phys. Lett.* **72**, 200 (1998).

- [67] J. Bösker, N.A. Stolwijk, H. Mehrer, U. Södervall, J.V. Thordson, T.G. Anderson and A. Buchard in: Diffusion mechanisms in crystalline materials, Y. Mishin, G. Vogl, N. Cowern, R. Catlow and D. Farkas (Eds.) , Pittsburgh: Mat. Res. Soc. (Proc. 527), (1998).
- [68] M. Uematsu, P. Werner, M. Schultz, T.Y. Tan and U. Gösele, Appl. Phys. Lett. **67**, 2863 (1995).
- [69] H.M. You, U.M. Gösele and T.Y. Tan, J. Appl. Phys. **73**, 7207 (1993).
- [70] H.S. Leipner, R. Scholz, F. Syrowatka, H. Uniewski and J. Schreiber, J. Phys. III France **7** 1495 (1997).
- [71] S.A. MsQuaid, R.C. Newman, M. Missous and S. O'Hagan, Appl. Phys. Lett. **61** 3008 (1992).
- [72] C. Domke, P. Ebert, M. Heinrich und K. Urban, Phys. Rev. B **54** 10288 (1996).
- [73] R.F. Scholz, P. Werner, U. Gösele, N. Engler and H.S. Leipner; J. Appl. Phys. **88**, 7045 (2000).
- [74] C.D. Anderson, Science **76**, 238 (1932).
- [75] P.A.M. Dirac, Proc. Roy. Soc. **117**, 610 (1928).
- [76] M.J. Puska and R.M. Nieminen, Rev. Mod. Phys. **66**, 841 (1994).
- [77] E. Soininen, J. Mäkinen, P. Hautojärvi, C. Corbel, A. Freundlich and J.C. Grenet, Phys. Rev. B **46**, 12394 (1992).
- [78] Y.Y. Shan, K.G. Lynn, P. Asoka-Kumar, S. Fung and C.D. Beling, Phys. Rev. B **55**, 9897 (1997).
- [79] R. Krause-Rehberg and H.S. Leipner (1999). *Positron annihilation in semiconductors*. Berlin, Springer-Verlag.
- [80] M.J. Puska and R.M. Nieminen, J. Phys. F. **13**, 333 (1983).
- [81] W. Brandt and R. Paulin, Phys. Rev. B **5**, 2430 (1972).
- [82] W. Frank and A. Seeger, Appl. Phys. **3**, 61 (1974).
- [83] M. Puska, Elinaikaspektrin sovitushohjelman LIFSPECFIT kehittaaminen. Teknillinen Korkeakoulu, Qtaniemi (1978).
- [84] P. Kirkegaard, N.J. Pedersen and M. Eldrup, in *positron annihilation*. Eds by L. Dorikens-Vanpret, M. Dorikens and D. Segers, World scientific, Singapore (1989).
- [85] A. Shukla, M. Peter, L. Hoffmann, Nucl. Instrum. Meth. A **335**, 310 (1993).
- [86] J. Kansy, Nucl. Instr. Meth. A, **374**, 235 (1996).
- [87] J. Kansy, LT for Windows, Version 9.0, Inst. of Phys. Chem. of Metals, Silesian University, Bankowa 12, PL-40-007 Katowice, Poland, March 2002 (private Communication).
- [88] K. Saarinen, P. Hautojärvi, A. Vehanen, R. Krause and G. Dlubek, Phys. Rev. B **39**, 5287 (1989).
- [89] M. Elsayed, V. Bondarenko, K. Petters and R. Krause-Rehberg, J. Phys.: Conference Series (JPCS) **265**, 012005 (2011).
- [90] M. Manninen and R.M. Nieminen, Appl. Phys. A **26**, 93(1981).
- [91] A. Polity, F. Rudolf, C. Nagel, S. Eichler and R. Krause-Rehberg, Phys. Rev. B **55**, 10467 (1997).
- [92] M. Elsayed, R. Krause-Rehberg, W. Anwand, M. Butterling and B. Korff, to be published.
- [93] M. Elsayed, V. Bondarenko, K. Petters, J. Gebauer and R. Krause-Rehberg, J. Appl. Phys. **104**, 103526 (2008).
- [94] M. J. Puska, C. Corbel and R.M. Nieminen, Phys. Rev. B **41**, 9980 (1990).
- [95] C. Le Berre, C. Corbel, K. Saarinen, S. Kuisma, P. Hautojärvi and R. Fornari, Phys. Rev. B **52**, 8112 (1995).
- [96] J. Gebauer, R. Krause-Rehberg, C. Domke, P. Ebert and K. Urban, Phys. Rev. Lett. **78**, 3334 (1997).

- [97] N.F. Mott and H.S. N. Massey, Eds. Theory of atomic collisions. Oxford, University Press (1965).
- [98] M. Alatalo, H. Kauppinen, K. Saarinen, M.J. Puska, J. Mäkinen, P. Hautojärvi and R.M. Nieminen, Phys. Rev. B **51**, 4176 (1995).
- [99] P. Asoka-Kumar, M. Alatalo, V.J. Ghosh, A.C. Kruseman, B. Nielsen and K.G. Lynn, Phys. Rev. Lett. **77**, 2097 (1996).
- [100] H. Kauppinen, L. Baroux, K. Saarinen, C. Corbel and P. Hautojärvi, J. Phys.: Condens. Matter **9**, 5495 (1997).
- [101] J. Gebauer, M. Lausmann, T.E.M. Staab, R. Krause-Rehberg, M. Hakala and M.J. Puska, Phys. Rev. B **60**, 1464 (1999).
- [102] S. Mantl and W. Triftshäuser, Phys. Rev. B **17**, 1645 (1978).
- [103] L. Liskay, C. Corbel, L. Baroux, P. Hautojärvi, M. Bayhan, A.W. Brinkmann and S. Tatarenko, Appl. Phys. Lett. **64**, 1380 (1994).
- [104] K. Saarinen, T. Laine, K. Skog, J. Mäkinen, P. Hautojärvi, K. Rakennus, P. Uusimaa, A. Salokatve and M. Pessa, Phys. Rev. Lett. **77**, 3407 (1996).
- [105] M. Alatalo, B. Barbiellini, M. Hakala, H. Kaupinen, T. Korhonen, M. J. Puska, K. Saarinen, P. Hautojärvi and R.M. Nieminen, Phys. Rev. B **54**, 2397 (1996).
- [106] M. Alatalo, P. Asoka-Kumar, V.J. Ghosh, B. Nielsen, K.G. Lynn, A.C. Kruseman, A. Van Veen, T. Korhonen and M.J. Puska, J. Phys. Chem. Solids **59**, 55 (1998).
- [107] U. Myler, R.D. Goldberg, A.P. Knights, D.W. Lawther and P.J. Simpson, Appl. Phys. Lett. **69**, 3333 (1996).
- [108] S. Szpala, P. Asoka-Kumar, B. Nielsen, J.P. Peng, S. Hayakawa, K.G. Lynn and H.-J. Gossmann, Phys. Rev. B **54**, 4722 (1996).
- [109] R. Krause-Rehberg, K. Petters and J. Gebauer, Physica B **273-274**, 714 (1999).
- [110] F. Börner, S. Eichler, A. Polity, R. Krause-Rehberg, R. Hammer and M. Jurisch, Appl. Surf. Sci. **149**, 151 (1999).
- [111] B. Somieski, T.E.M. Staab and R. Krause-Rehberg, Nucl. Instr. Meth. Phys. Res. A **381**, 128 (1996).
- [112] A. Vehanen, K.G. Lynn, P.J. Schutz and M. Eldrup, Appl. Phys. A **32**, 163, (1983).
- [113] R. Khatri, M. Charlotten, P. Sferlazzo, K.G. Lynn, A.P.J. Mills and L.O. Roelling, Appl. Phys. Lett. **57**, 2374 (1990).
- [114] G. Brauer, W. Anwand, E.-M. Nicht, P.G. Colemann, N. Wagner, H. Wirth, W. Skorupa, Appl. Surf. Sci. **116**, 19 (1997).
- [115] B. Werlich (2010), Untersuchung von Elektromigration an Kupfer mittels monoenergetischer Positronen. Halle (Saale), Martin Luther Universität.
- [116] P. Sperr and G. Kögel, Mater. Sci. Forum **255-257**, 109 (1997).
- [117] P. Willutzki, J. Störmer, G. Kögel, P. Sperr, D.T. Britton, R. Steindl and W. Triftshäuser, Meas. Sci. Technol. **5**, 548 (1994).
- [118] R. Suzuki, T. Ohdaira and T. Mikado, Radiat. Phys. Chem. **58**, 603 (2000).
- [119] J.P. Peng, K.G. Lynn, P. Asoka-Kumar D.P. Becker and D.R. Harshman, Phys. Rev. Lett. **76**, 2157 (1996).
- [120] R. Krause-Rehberg, V. Bondarenko, E. Thiele, R. Klemm and N. Schell, Nucl. Instr. and Meth. in Phys. Res. B **240** 719 (2005).
- [121] S. Valkealahti and R.M. Nieminen, Appl. Phys. A **32** 95 (1983).
- [122] A. Vehanen, K. Saarinen, P. Hautojärvi and H. Huomo, Phys. Rev. B **35** 4606 (1987).
- [123] J. Gebauer, S. Eichler, R. Krause-Rehberg and H.P. Zeindl, Appl. Surf. Sci. **116**, 247 (1997).
- [124] S. Valkealahti and R.M. Nieminen, Appl. Phys. A: Solids Surf. **35**, 51 (1984).
- [125] V.J. Ghosh, Appl. Surf. Sci. **85**, 187 (1995).

- [126] A. Van Veen, H. Schut, M. Clement, J.M.M. de Nijs, A. Kruseman, M.R. IJpma, *Appl. Surf. Sci.* **85**, 216 (1995).
- [127] R.M. Cohen, *Mater. Sci. Eng. R.* **20**, 167 (1997).
- [128] R. Leon, P. Werner, K.M. Yu, M. Kaminska and E.R. Weber, *Appl. Phys. A* **61**, 7 (1995).
- [129] N.A. Gokcen, *Bulletin of Alloy Phase Diagrams* **10**, 11 (1989).
- [130] R. Krause-Rehberg and H.S. Leipner, *Appl. Phys. A* **64**, 457 (1997).
- [131] V. Bondarenko, K. Petters, R. Krause-Rehberg, J. Gebauer and H.S. Leipner, *Physica B* **308-310**, 792 (2001).
- [132] J. Gebauer, F. Börner, R. Krause-Rehberg, T.E.M. Staab, W. Bauer-Kugelmann, G. Kögel, W. Triftshäuser, P. Specht, R.C. Lutz, E.R. Weber and M. Luysberg, *J. Appl. Phys.* **87**, 8368 (2000).
- [133] T.E.M. Staab, M. Haugk, A. Sieck, Th. Frauenheim and H.S. Leipner, *Physica B* **273-274**, 501 (1999).
- [134] V. Bondarenko, J. Gebauer, F. Redmann and R. Krause-Rehberg, *Appl. Phys. Lett.* **87**, 161906 (2005).
- [135] J. Gebauer, M. Lausmann, F. Redmann and R. Krause-Rehberg, *Physica B* **273-274**, 705 (1999).
- [136] C.C. Tin, C.K. Teh and F.L. Weichman, *J. Appl. Phys.* **62**, 2329 (1987).
- [137] K. Kuriyama, K. Tomizava, S. Uematsu and Hirokazu Takahashi, *Appl. Phys. Lett.* **65**, 746 (1994).
- [138] K. Petters, J. Gebauer, F. Redmann, H.S. Leipner and R. Krause-Rehberg, *Mater. Sci. Forum* **363-365**, 111 (2001).
- [139] B.Pagh, H.E. Hansen, B. Nielsen, G. Trumphy and K. Petersen, *Appl Phys. A* **33**, 255 (1984).
- [140] R.C. Newman, *Semicond. Sci. Technol.* **9**, 1749 (1994).
- [141] D.T.J. Hurle, *J. Phys. Chem. Solids* **40**, 613 (1979).
- [142] S.B. Zhang and J.E. Northrup, *Phys. Rev. Lett.* **67**, 2339 (1991).
- [143] G.A. Baraff and M. Schlüter, *Phys. Rev. B* **33**, 7346 (1986).
- [144] D.J. Chadi, *Mater. Sci. Forum* **258-263**, 1321 (1997).
- [145] E.W. Williams, *Phys. Rev.* **168**, 922 (1968).
- [146] C. Domke, Ph. Ebert, M. Heinrich and K. Urban, *Phys. Rev. B* **54**, 10288 (1996).
- [147] P. Hautojärvi, *Positrons in Solids, Vol. 12 of Topics in Current Physics*, edited by P. Hautojärvi (Springer, Heidelberg, 1979).
- [148] *Positron Solid State Physics*, edited by W. Brandt and A. Dupasquier (North-Holland, Amsterdam, 1983).
- [149] P. Hautojärvi and C. Corbel, *Positron Spectroscopy of Solids*, Proceedings of the Int. School of Physics, Enrico Fermi (ISO Press 1995) p. 491.
- [150] C. Corbel and P. Hautojärvi, *Positron Spectroscopy of Solids*, Proceedings of the Int. School of Physics, Enrico Fermi (ISO Press 1995) p. 533.
- [151] R. Krause-Rehberg, H.S. Leipner, T. Abgarjan and A. Polity, *Appl. Phys. A* **66**, 599 (1998).
- [152] K. Saarinen, P. Hautojärvi, P. Lanki and C. Corbel, *Phys. Rev. B* **44**, 10585 (1991).
- [153] R. Krause-Rehberg, H.S. Leipner, A. Kupsch, A. Polity and Th. Drost, *Phys. Rev. B* **49**, 2385 (1994).
- [154] S. Fujii and S. Tanigawa, *Hyperfine Interact.* **79**, 719 (1993).
- [155] P.J. Schultz, K. G. Lynn, I. K. Mackenzie, Y. C. Jean and C. L. Snead, *Phys. Rev. Lett.* **44**, 1623 (1980).
- [156] S. Linderoth and C. Hidalgo, *Phys. Rev. B* **36**, 4054 (1987).
- [157] L.C. Smedskjaer, M. Manninen and M. J. Fluss, *J. Phys. F* **10**, 2237 (1980).

- [158] I.K. Mackenzie, Phys. Rev. B **16**, 4705 (1977).
- [159] M.J. Puska, O. Jepsen, O. Gunnarsson and R.M. Nieminen, Phys. Rev. B **34**, 2965 (1986).
- [160] G. Dlubek, O. Brümmer, F. Plazaola and P. Hautojärvi, J. Phys. C **19**, 331 (1986).
- [161] S. Dannefear and D. Kerr, J. Appl. Phys. **60**, 591 (1986).
- [162] P. Hautojärvi, P. Moser, M. Stucky, C. Corbel and F. Plazaola, Appl. Phys. Lett. **48**, 809 (1986).
- [163] T. Laine, K. Saarinen, J. Mäkinen, P. Hautojärvi, C. Corbel, L.N. Pfeiffer and P.H. Citrin, Phys. Rev. B **54**, R11 050 (1996).
- [164] T. Hiramoto and T. Ikoma, *the source of copper contamination in commercial semi-insulating GaAs wafers, Semi-insulating III-V materials*, Malmö 1988, G. Grossmann and L. Ledebö, Eds. (Adam Hilger, 1988) pp. 337-342.
- [165] H.S. Leipner, R.F. Scholz, F. Syrowatka, J. Schreiber and P. Werner, Philos. Mag. A **79**, 2785 (1999).
- [166] R.A. Roush, D.C. Stoudt and M.S. Mazzola, Appl. Phys. Lett. **52** 2670 (1993).
- [167] A. Sen Gupta, S.V. Naidu and P. Sen, Appl. Phys. A **40**, 95 (1986).
- [168] B. Barbiellini, M.J. Puska, T. Korhonen, A. Harju, T. Torsti and R.M. Nieminen, Phys. Rev. B **53**, 16201 (1996).
- [169] N.W. Ashcroft and N.D. Mermin, Solid State Physics (Holt-Saunders, New Yourk, 1976), p. 579.
- [170] O.V. Boev, M.J. Puska and R.M. Nieminen, Phys. Rev. B **36**, 7786 (1987).
- [171] B. Imer, M. Schmidt, B. Haskell, S. Rajan, B. Zhong, K. Kim, F. Wu, T. Mates, S. Keller, U.K. Mishra, S. Nakamura, J.S. Speck and S.P. DenBaars, Phys. Stat. Sol. (a) **205**, 1705 (2008).
- [172] S. Lutgen and M. Schmitt, Optik & Photonik **2**, 37 (2009).
- [173] K. Fujito, S. Kubo, H. Nagaoka, T. Mochizuki, H. Namita and S. Nagao, J. Cryst. Growth **311**, 3011 (2009).
- [174] T.L. Tansley and R.J. Egan, Phys. Rev. B **45**, 10942 (1992).
- [175] P. Perlin, T. Suski, H. Teisseyre, M. Leszczynski, I. Grzegory, J. Jun, S. Porowski, P. Boguslawski, J. Bernholc, J.C. Chervin, A. Polian and T.D. Moustakas, Phys. Rev. Lett. **75**, 296 (1995).
- [176] J. Zou, D. Kotchetkov, A.A. Balandin, D.I. Florescu and Fred H. Pollak, J. Appl. Phys. **92**, 2534 (2002).
- [177] P.R. Tavernier, T. Margalith, J. Williams, D.S. Green, S. Keller, S.P. DenBaars, U. K. Mishra, S. Nakamura and D.R. Clarke, J. Cryst. Growth **264**, 150 (2004).
- [178] C.G. Van de Walle and J. Neugebauer, J. Appl. Phys. **95**, 3851 (2004).
- [179] M.A. Reshchikova and H. Morkoç, J. Appl. Phys. **97**, 061301 (2005).
- [180] S.-N. Lee, K.K. Kim, O.H. Nam, J.H. Kim and H. Kim, Phys. Stat. Sol. (c) **7**, 2043 (2010).
- [181] J. Neugebauer and C. Van de Walle, Appl. Phys. Lett. **69**, 503 (1996).
- [182] T. Mattila and R.M. Nieminen, Phys. Rev. B **55**, 9571 (1997).
- [183] S. Limpijumngong and C.G. Van de Walle, Phys. Rev. B **69**, 035207 (2004).
- [184] K. Saarinen, T. Laine, S. Kuisma, J. Nissilä, P. Hautojärvi, L. Dobrzynski, J.M. Baranowski, K. Pakula, R. Stepniewski, M. Wojdak, A. Wyszomolek, T. Suski, M. Leszczynski, I. Grzegory and S. Porowski, Phys. Rev. Lett. **79**, 3030 (1997).
- [185] O. Moutanabbir and U. Gösele, Annu. Rev. Mater. Res. **40**, 469 (2010).
- [186] R.Q. Wu, G.W. Peng, L. Liu, Y.P. Feng, Z.G. Huang and Q.Y. Wu, Appl. Phys. Lett. **89**, 062505 (2006).
- [187] A.L. Rosa and R. Ahuja, Appl. Phys. Lett. **91**, 232109 (2007).

- [188] J.-H. Lee, S. Shin, S. Lee, J. Lee, C. Whang, S.-C. Lee, K.-R. Lee, J.-H. Baek, K. H. Chae and J. Song, *Appl. Phys. Lett.* **90**, 032504 (2007).
- [189] X.L. Yang, Z.T. Chen, C.D. Wang, Y. Zhang, X.D. Pei, Z.J. Yang, G.Y. Zhang, Z.B. Ding, K. Wang and S. D. Yao, *J. Appl. Phys.* **105**, 053910 (2009).
- [190] J. Hong, *J. Appl. Phys.* **103**, 063907 (2008).
- [191] H.-K. Seong, J.-Y. Kim, J.-J. Kim, S.-C. Lee, S.-R. Kim, U. Kim, T.-E. Park and H.-J. Choi, *Nano Lett.* **7**, 3366 (2007).
- [192] P.R. ganz, C. Sürgers, G. Fischer and D. M. Schaadt, *J. Phys.: Conf. Series* **200**, 062006 (2010).
- [193] J.-P. Ao, D. Kikuta, N. Kubota, Y. Naoi and Y. Ohno, *IEICE Trans Electron* **E86-C**, 2051 (2003).
- [194] J.-P. Ao, N. Kubota, D. Kikuta, Y. Naoi and Y.o Ohno, *Phys. Stat. Sol. (c)* **0**, 2376 (2003).
- [195] K. Saarinen, T. Suski, I. Grzegory and D. C. Look, *Phys. Rev. B* **64**, 233201 (2001).
- [196] A. Uedono, S.F. Chichibu, Z.Q. Chen, M. Sumiya, R. Suzuki, T. Ohdaira T. Mikado, T. Mukai and S. Nakamura, *J. Appl. Phys.* **90**, 181 (2001).
- [197] J. Oila, A. Kemppinen, A. Laakso, K. Saarinen, W. Egger, L. Liskay, P. Sperr, H. Lu and W.J. Schaff, *Appl. Phys. Lett.* **84**, 1486 (2004).
- [198] A. Uedono, S.F. Chichibu, M. Higashiwaki, T. Matsui, T. Ohdaira and R. Suzuki, *J. Appl. Phys.* **97**, 043514 (2005).
- [199] A. Pelli, K. Saarinen, F. Tuomisto, S. Ruffenach and O. Briot, *Appl. Phys. Lett.* **89**, 011911 (2006).
- [200] S. Zeng, G.N. Aliev, D. Wolverson, J.J. Davies, S.J. Bingham, D.A. Abdulmalik, P.G. Coleman, T. Wang and P.J. Parbrook, *Appl. Phys. Lett.* **89**, 022107 (2006).
- [201] S. Hautakangas, I. Makkonen, V. Ranki, M.J. Puska, K. Saarinen, X. Xu and D.C. Look, *Phys. Rev. B* **73**, 193301 (2006).
- [202] F. Tuomisto, A. Pelli, K.M. Yu, W. Walukiewicz and W.J. Schaff, *Phys. Rev. B* **75**, 193201 (2007).
- [203] A. Uedono, S. Ishibashi, T. Ohdaira and R. Suzuki, *J. Cryst. Growth* **311**, 3075 (2009).
- [204] O. Moutanabbir, R. Scholz, U. Gösele, A. Guittoum, M. Jungmann, M. Butterling, R. Krause-Rehberg, W. Anwand, W. Egger and P. Sperr, *Phys. Rev. B* **81**, 115205 (2010).
- [205] S.S. Park, Il-W. Park and S. H. Park, *Jpn. J. Appl. Phys.* **39**, L1141 (2000).
- [206] S. Hautakangas, J. Oila, M. Alatalo, K. Saarinen, L. Liskay, D. Seghier and H.P. Gislason, *Phys. Rev. Lett.* **90**, 137402 (2003).
- [207] S. Hautakangas, K. Saarinen, L. Liskay, J.A. Freitas, Jr. and R. L. Henry, *Phys. Rev. B* **72**, 165303 (2005).
- [208] H. Yi-Fan, C.D. Beling and S. Fung, *Chin. Phys. Lett.* **22**, 1214 (2005).
- [209] P.J. Schultz and K.G. Lynn, *Rev. Mod. Phys.* **60**, 701 (1988).
- [210] J. Oila, V. Ranki, J. Kivioja, K. Saarinen, P. Hautojärvi, J. Likonen, J.M. Baranowski, K. Pakula, T. Suski, M. Leszczynski and I. Grzegory, *Phys. Rev. B* **63**, 045205 (2001).
- [211] H.C. Casey, in D. Shaw (ed.), *Atomic Diffusion in Semiconductors*, Plenum, 1973, p. 351.
- [212] H. Bracht, M.S. Norseng, E.E. Haller and K. Eberl, *Physica B* **308–310** 831 (2001).
- [213] G. Bösker, N.A. Stolwijk, H.-G. Hettwer, A. Rucki, W. Jäger and U.S. odervall, *Phys. Rev. B* **52** 11927 (1995).
- [214] R.L. Longini, *Solid-State Electron.* **5**, 127 (1962).
- [215] M. Luysberg, W. Jäger, K. Urban, M. Schänzer, N.A. Stolwijk and H. Mehrer, *Mater. Sci. and Engin. B* **13**, 137 (1992).
- [216] H.R. Winteler, *Helv. Phys. Acta*, **44**, 451 (1970).

-
- [217] F. Börner, S. Eichler, A. Polity, R. Krause-Rehberg, R. Hammer and M. Jurisch, *J. Appl. Phys.*, **84**, 2255 (1998).
- [218] W. Brandt and R. Paulin, *Phys. Rev. B* **15**, 2511 (1977).
- [219] J. Gebauer, R. Krause-Rehberg, C. Domke, Ph. Ebert, K. Urban and T.E.M. Staab, *Phys. Rev. B*, **63** 045203 (2001).
- [220] R. Krause-Rehberg, V. Bondarenko, J. Pöpping, N.A. Stolwijk, T.E.M. Staab and U. Södervall, *Mater. Sci. Forum*, **445-446**, 26 (2004).

Erklärung

Hiermit erkläre ich an Eides Statt, dass ich die vorliegende Arbeit selbständig und ohne fremde Hilfe verfasst und nur die angegebenen Quellen und Hilfsmittel verwendet habe. Ergebnisse anderer wissenschaftlicher Arbeiten wurden als solche gekennzeichnet. Diese Arbeit wurde bisher weder im In- noch im Ausland in gleicher oder ähnlicher Form in einem Prüfungsverfahren vorgelegt. Ich erkläre hiermit, dass ich mich bis zu dem jetzigen Zeitpunkt noch nie um einen Doktorgrad beworben habe.

Halle (Saale), December 2010

Mohamed Elsayed

Curriculum vitae

Family name: Elsayed

Given name: Mohamed

Date of birth: 23/11/1976

Place of birth: Minia, Egypt

Marital status: Married. One child.

1982-1988: Primary school.

1988-1991: Preparatory school.

1991-1995: Secondary school.

1995-1999: Student at the Faculty of Education, Cairo University (Beni Suef branch), Beni Suef, Egypt.

May 1999: B.Sc. Physics, Faculty of Education, Cairo University (Beni Suef branch), Beni Suef, Egypt.

2000-2002: Student at the Faculty of Science, Minia University, Minia, Egypt.

May 2002: B.Sc. Physics, Faculty of Science, Minia University, Minia, Egypt.

2002-2006: M.Sc. Student Faculty of Science, Minia University, Minia, Egypt.

May 2006: M.Sc. Physics, Faculty of Science, Minia University, Minia, Egypt.

2007-2010: Ph.D. student, Institut für Physik, Naturwissenschaftliche Fakultät II, Martin Luther Universität, Halle (Saale), Germany.

Acknowledgements

First, my outmost thanks go to **Allah** for giving me the strength, patience and great support for conducting this work.

I would like to express my deepest gratitude and sincere appreciation for my supervisor Prof. Dr. R. Krause-Rehberg for initiation of this study, his constant support in work organization, constant guidance and many fruitful discussions. With your much needed patience, I managed to learn a lot in material science and experimental techniques.

I am also thankful to Prof. Dr. G. Dlubek and P. D. H.S. Leipner for their beneficial discussions and encouragement.

To all my colleagues in the work group of positron annihilation at the Martin Luther University Halle-Wittenberg, cordial thanks for all the intellectual discussions we had. I am grateful to my predecessors in the positron laboratory Dr. E. Sayed-Ahmed, Dr. S. Thränert, Dipl. Phys. M. Penzler and Dipl. Phys. F. Süßkraut. Special thanks also go to my colleagues, Dipl. Phys. A. Krille, Dipl. Phys. M. Jungmann, Dipl. Phys. M. Butterling, Dipl. Phys. Y. Yu, Dipl. Phys. B. Werlich and B. Sc. J. Häberle for their help and needed friendship.

I would like to thank Prof. Dr. N.A. Stolwijk and his group (Univ. Münster), from whom I have learnt the preliminary steps of diffusion experiments.

Many thanks go to the team of the mechanical workshop for their help with many technical aspects. I owe to thank Herr. T. Schurig (Glassblower) and Dipl. Ing. A. Müller (electronic workshop). The help of Dipl. Ing. H. Mähl is deeply appreciated.

I am thankful to Dipl. Phys. B. Korff for performing the theoretical calculation as well to Dipl. Phys. S. Richter and Dr. C. Hagendorf (Fraunhofer Institute) for the SIMS measurements.

I would like to acknowledge Dipl. Phys. W. Anwand (Rossendorf) and Dr. O. Moutanabbir (MPI Halle) for their wonderful cooperation.

I would like to express my thankfulness for Dr. S. Eichler in Freiburger Compound Materials GmbH for supplying most of GaAs wafers investigated in this work. I would like to thank Dr. M. Farag (Leibniz Institute Halle) for language checking.

I am indebted for the continuous support from my passed mother and father and without whom I could not have accomplished this degree. Special thank goes to my siblings for all their help and motivation.

I am grateful to my wife Shaimaa and my child Alyaa for their patience and great support in many ways during my Ph.D. study.

Financial Support from the Egyptian Higher Education Ministry and Minia University for conducting this study in Germany is gratefully acknowledged.

I would like to take this opportunity to thank my master thesis supervisors Prof. Dr. M. Abdel Rahman and Prof. Dr. E. Badawi (Minia University, Egypt), with the help of whom I managed to take my first step in research.